

DYNAMIC RANGE ENHANCMENT IN DIGITAL FRINGE PROJECTION AND
LASER INTERFEROMETRY

by

Gelareh Babaie

A dissertation submitted to the faculty of
The University of North Carolina at Charlotte
in partial fulfillment of the requirements
for the degree of Doctor of Philosophy in
Optical Science and Engineering

Charlotte

2015

Approved by:

Dr. Faramarz Farahi

Dr. Angela D. Davies

Dr. Christopher J. Evans

Dr. Nathaniel M. Fried

Dr. Mehdi Miri

ABSTRACT

GELAREH BABAIE. Dynamic range enhancement in digital fringe projection and laser interferometry. (Under the direction of DR. FARAMARZ FARAH)I)

Optical metrology is the science and technology concerning measurements with light. Surface texture and 3D profile measurement are very important in many applications such as production automation, robot vision, virtual reality, medical image diagnosis, and other fields. Fringe projection profilometry and laser interferometry systems are two powerful optical methods for surface shape and texture measurements. These techniques offer the advantages of non-contact operation, full-field acquisition, high resolution, and fast data processing. As a result, these techniques are widely used in different fields where fast and accurate measurement is required. However, despite the widespread use of these systems, there are several limitations in acquiring and analyzing interferometric data. One serious limitation, which significantly decreases the SNR in both fringe projection and laser interferometry systems, is the limited dynamic range of imaging systems. For example, a typical 8-bit camera can represent the intensity level between 0 to 255 grayscale, while the optical reflectivity of objects under the measurement towards the camera can be much wider. As a result, some areas in the image taken by the camera are saturated while other areas are underexposed. Consequently the true intensity values and phase information of the corresponding saturated and underexposed areas cannot be correctly retrieved for metrology purposes. Therefore, achieving a system with high dynamic range is very desirable in the field of optical metrology. This research effort, in part, is focused on addressing the dynamic range problem in both digital fringe projection and laser interferometry techniques. Spatially Varying Pixel Intensity (SVPI) technique is

introduced as a tool to enhance dynamic range in optical metrology tools specifically in digital fringe projection and laser interferometer systems. The results obtained demonstrate that this technique can increase the signal to noise ratio in the fringe projection and laser interferometer system, hence improving the measurement precision.

In the second part of the research, profilometry based on optical wavelength conversion is introduced as a new technique for 3D profilometry of objects composed of unique raw materials, such as dark, non-reflective objects.

A solid can absorb light as the result of intraband transitions. When the energy of the incident light exceeds the energy bandgap of the solid, the electrons absorb the energy of the light and electron jumps from the ground energy level to the higher excited level. The reverse process can happen when the electrons in the excited states drop to the lower level by either emitting a photon (radiative process) or by releasing heat (non-radiative process).

The amount of light absorption, percentage of absorbed light that is converted to another wavelength, depends on the optical properties of the material that the object is made from. New fringe projection systems based on wavelength conversion are presented in this thesis that offer increased signal to noise ratio as well as increasing the effective numerical aperture of the measurement systems.

ACKNOWLEDGMENTS

First and foremost I would like to thank my advisor, Prof. Faramarz Farahi for giving me the opportunity to accomplish my Ph.D. under his esteemed guidance. I truly appreciate all his contributions of time, ideas, and support to make my Ph.D. experience productive and stimulating. I would like to thank him for allowing me to grow as a research scientist. His advices on my research, career, and personal growth have been invaluable.

I would also like to thank my committee members, Prof. Angela Davies, Prof. Christopher J. Evans, Prof. Nathaniel Fried, and Prof. Mehdi Miri for their time, interest, helpful comments and support, and for making my defense an enjoyable and memorable moment.

A special thanks to my former lab partner, Dr. Mehrdad Abolbashari, for his generous support and help during my research. He is the most humble, and hardworking person I have ever met.

I would also like to acknowledge the Industrial Affiliates of the Center for Precision Metrology for funding this project.

Lastly, I would like to thank my family for all their love and encouragement. To my parents, who raised me with love and supported me in all my pursuits, to my sister for being my best friend throughout all my life, to my uncle, Majid, for always giving me the correct advice during rough moments of my Ph.D., and finally, to my loving, supportive, and patient husband, Babak. This PhD would not have been possible without him and his love.

TABLE OF CONTENTS

LIST OF FIGURE	ix
CHAPTER 1: INTRODUCTION	1
1.1. Introduction	1
1.2 Limitations in Optical Metrology Associated with System Components	4
1.3 Limitations in Optical Metrology Associated with the Intrinsic Nature of the Measurement Method	6
1.4. Limitations Associated with Combined Object Properties and System Characteristics	9
1.4.1 High Dynamic Range Photography	10
1.4.2 Dynamic Range Enhancement In Interferometric Based Technique	16
CHAPTER 2: 3D PROFILOMETRY OF OBJECTS USING FRINGE PROJECTION AND LASER INTERFEROMETERS	19
2.1 Fringe Projection Profilometry Technique	19
2.1.1 Temporal Fringe Analysis Technique	25
2.1.2 Spatial Fringe Analysis Technique	27
2.2. Interferometry	29
2.2.1. Basics of Interferometry	29
2.2.2. Interferometry Techniques For Surface Topography Measurement	31
2.2.3. Michelson Interferometers	32
2.2.4. Mirau Interferometer	33
2.2.5. Linnik Interferometes	34
CHAPTER 3: DYNAMIC RANGE ENHANCEMENT IN 3D PROFILOMETRY OF FREE FORM OBJECTS USING DIGITAL FRINGE PROJECTION	37

3.1. Introduction	37
3.2. SVPI Measurement Method in Digital Fringe Projection Profilometry	39
3.3 Simulation	50
3.4. Three Dimensional Profile Measurement of a Calibration Sphere	53
3.5. Three Dimensional Profile Measurements of Solder Bumps	60
3.6. Three Dimensional Profile Measurements of Large Industrial Objects with Steep Slopes using Digital Fringe Projection	69
CHAPTER 4: DYNAMIC RANGE ENHANCEMENT IN LASER INTERFEROMETERS	80
4.1. Introduction	80
4.2. Experimental Setup	83
4.2.1. Instrumentation	83
4.2.2. Geometrical Alignment	85
4.3. SVPI Algorithm Measurement Procedure	86
4.4. Experimental Results and Discussion	90
CHAPTER 5: THREE- DIMENSIONAL PROFIOMETRY OF OBJECTS BASED ON ABSORPTION AND OPTICAL FREQUENCY CONVERSION	96
5.1. Introduction	96
5.2. Absorption and Emission in Solid State Materials	97
5.3. Profilometry of a Hemispherical Polymer Surface using Optical Wavelength Conversion	100
5.3. Optical Profilometry of Dark Objects Based on Optically Induced Heat	107
5.3.1 Experimental Setup and Results	110
5.4 Discussion	117

	viii
CHAPTER 6: CONCLUSIONS AND FUTURE WORK	118
6.1 Conclusions	118
6.2 Future Work	122
REFERENCES	126

LIST OF FIGURES

FIGURE 1.1: A 2D array of micro-optical systems overlaying a 2 array of detector, which enables the system to form a complete, large-format, high-resolution image [17].	5
FIGURE 1.2: Schematic of the dual-moiré-laser interferometer	6
FIGURE 1.3: A schematic of a digital camera, which illustrates how is a scene radiance transformed to pixel values.	12
FIGURE 1.4: Formation of a high dynamic range image using a sequence of images with different exposure [43].	15
FIGURE 1.5 An interference pattern obtained from a Michelson laser interferometer with two different exposure times.	16
FIGURE 2.1: A schematic of a typical fringe projection profilometry system.	20
FIGURE 2.2: A fringe projection triangulation setup with a flat reference surface.	21
FIGURE 2.3: Schematic of a fringe projection triangulation setup for 3D profilometry of an object.	22
FIGURE 2.4: A schematic of a Michelson laser interferometer for surface measurement.	33
FIGURE 2.5: A schematic of a Mirau interferometer.	34
FIGURE 2.6: A schematic of a Linnik interferometer.	35
FIGURE 2.7: An interferogram obtained by a laser interferometer from a surface [49].	36
FIGURE 3.1: (a) Reflected fringe pattern captured by the camera from the metallic ball with exposure time = 5ms, and (b) reflected pattern of the same sample with exposure time = 1s.	38
FIGURE 3.2 Linear geometrical alignment between the projector coordinate and camera.	41
FIGURE 3.3: Geometrical alignment between camera pixels and projector pixels, a) projected pattern, and b) captured image by the camera.	44
FIGURE 3.4: SVPI technique flowchart to enhance dynamic range in a fringe projection.	49

- FIGURE 3.5: (a) Initial simulated structured pattern, (b) the simulated object, and (c) the initial reflected pattern. 50
- FIGURE 3.6: Simulation results for the DR enhancement using SVPI technique, a) intensity mask, a(1), structured pattern, a(2) and the reflected pattern, a(3), before applying the SVPI, $KDR = 0.07$, b) intensity mask, b(1), structured pattern, b(2), and the reflected pattern, b(3) after applying the SVPI once, $KDR = 0.35$, c) intensity mask, c(1), structured pattern, c(2) and the reflected pattern, c(3) after applying the SVPI twice, $KDR = 0.95$ 51
- FIGURE 3.7: (a) HDR constructed image using the SVPI technique, and (b) the phase map of the object using the DCFT technique 52
- FIGURE 3.8: Schematic of a system implemented to demonstrate dynamic range enhancement in digital fringe projection for 3D profile measurement of a calibration ball. 54
- FIGURE 3.9: (a) First structured pattern projected onto the sample without applying the SVPI, (b) first reflected image captured by the camera, (c) modified structured pattern based on SVPI technique, and (d) reflected pattern recorded by the camera after applying the SVPI once. 55
- FIGURE 3.10: a (1) Initial structured pattern illuminating the sample, a (2) first reflected image captured by the camera, $KDR = 0.79 \pm 0.03$, b (1) modified structured pattern after applying the SVPI once, b (2) reflected image using the modified pattern b (1), $KDR = 0.89 \pm 0.03$, c (1) modified structured pattern after applying the SVPI twice, and c (2) reflected image using the modified pattern c (1), $KDR = 0.99 \pm 0.03$. 56
- FIGURE 3.11: (a) Phase of the metallic ball calculated by 4-step phase shifting, and (b) unwrapped phase map of the sample 57
- FIGURE 3.12: Equivalent wavelength map for the fringe projection setup used for 3D profilometry of the calibration ball. 58
- FIGURE 3.13: Actual height map of the calibration ball using the SVPI technique in a digital fringe projection system. 60
- FIGURE 3.14: Solder bump field on the middle of a substrate package at different magnification. 61

- FIGURE 3.15: Schematic of the experimental setup of dynamic range enhancement in fringe projection using SVPI technique. 62
- FIGURE 3.16: The reflected pattern captured by the SVPI system with an exposure time = 16.56 ms. 62
- FIGURE 3.17: (a) Initial structured pattern illuminated to the solder bumps, (b) first reflected pattern captured by the camera, $KDR = 0.57 \pm 0.03$, (c) first modified structured pattern after applying the SVPI technique once, (d) second captured pattern, $KDR = 0.89 \pm 0.03$, (e) second modified structured pattern after applying the SVPI technique twice, and (f) third reflected pattern, $KDR = 0.98 \pm 0.03$. 63
- FIGURE 3.18: a) Combined carrier phase and object phase map obtained from the four-step phase shift fringe analysis technique, (b) Fourier spectrum of the combined phase map, (c) filtered and shifted to center phase spectrum, and (d) wrapped phase of the object without the carrier phase information. 64
- FIGURE 3.19: Three dimensional unwrapped phase of the solder bumps using SVPI technique in a digital fringe projection setup. 65
- FIGURE 3.20: (a) 3D profile of one solder bump calculated from the SVPI technique, (b) hemisphere fit, (c) data selected from the raw profile of the solder bump, (d) selected data from the hemisphere fit, and (e) final profile of the solder bump with sharp edges. 66
- FIGURE 3.21: Three-dimensional profile of 9 solders bumps with sharp edges using the fitting process. 67
- FIGURE 3.22: Three-dimensional profile of 9 solders bumps with sharp edges using the fitting process above the solder resist layer. 68
- FIGURE 3.23: (a) The outer surface of a hemispherical shaped industrial object, and (b) the inner surface of a hemispherical shaped industrial object. 69
- FIGURE 3.24: Digital fringe projection profilometry setup used for industrial spherical object profile measurement. 70
- FIGURE 3.25: Images taken by the camera with different exposure times from the industrial spherical object. 71
- FIGURE 3.26: Piecewise linear geometrical alignment process between the projector plane and the camera image plane, 71

(a) projector pattern with several segment with known three points, and (b) image obtained from the object illuminated by a known projected pattern.

- FIGURE 3.27: Applying the SVPI technique on an industrial spherical object in order to enhance dynamic range in a digital fringe projection setup. 73
- FIGURE 3.28: (a) Obtained image by the fringe projection setup at 20 ms camera exposure time before applying the SVPI. Dynamic range coefficient of this image is $KDR = 48.36 \pm 0.02$. (b) Obtained image by the fringe projection setup at 250 ms camera exposure time before applying the SVPI. Dynamic range coefficient of this image is $KDR51.33 \pm 0.02$. (c) Obtained image by the fringe projection setup at 250 ms camera exposure time after applying the SVPI. Dynamic range coefficient of this image is $KDR = 91.06 \pm 0.02$. 74
- FIGURE 3.29: (a) Phase of the sample calculated from a 4-step phase shifting algorithm, (b) wrapped phase map of the object, and (c) calculated unwrapped phase map of the object using quality-guided algorithm. 75
- FIGURE 3.30: Three-dimensional profile of the outer surface of the industrial object using the SVPI technique in a fringe projection setup. 76
- FIGURE 3.31: Radial profile of the industrial object using the SVPI technique in a fringe projection setup. 77
- FIGURE 3.32: Three-dimensional profile of the inner surface of the industrial object using the SVPI technique in a fringe projection setup. 77
- FIGURE 3.33: Three-dimensional profile of the inner surface of the industrial object using the SVPI technique in a fringe projection setup. 78
- FIGURE 4.1: (a) An interference pattern obtained from a Michelson laser interferometer at camera exposure time set to 300 ms, and (b) an interference pattern obtained from a Michelson laser interferometer at camera exposure time set to 50 ms. 81
- FIGURE 4.2: A schematic of a liquid crystal spatial light modulator by a TFT switch [102]. 82
- FIGURE 4.3: A schematic of a Michelson interferometer and the experimental setup used to demonstrate dynamic range enhancement technique. 84

FIGURE 4.4: Experimental setup used for dynamic range enhancement in a Michelson laser interferometer using the SVPI technique.	85
FIGURE 4.6. SVPI algorithm used to enhance the dynamic range of a laser interferometer.	89
FIGURE 4.7. Image obtained by the camera at exposure time 500 ms.	90
FIGURE 4.8: (a) Initial transmission of the SLM, (b) image obtained by the camera at exposure time 500 ms, (c) modified transmission of the SLM after the first iteration, (d) image obtained by the camera at exposure time 500 ms for modified SLM, e) modified transmission of the SLM after the second iteration, and (f) image obtained by the camera at exposure time 500 ms.	92
FIGURE 4.9: Three-dimensional profile of the flat mirror obtained from a Michelson laser interferometry after applying the SVPI technique once.	93
FIGURE 4.10: Three-dimensional profile of the flat mirror obtained from a Michelson laser interferometry after applying the SVPI technique twice.	94
FIGURE 5.1 Schematic diagram of the vibrational-electronic transitions in a semiconductor.	99
FIGURE 5.2: Hemispherical shape objects composed of a unique polymers combination.	101
FIGURE 5.3 (a) A schematic of the fringe projection setup used for profilometry of a hemispherical shaped object composed of a specific polymer, and (b) the reflected image obtained by the CMOS camera.	101
FIGURE 5.4 (a) The experimental setup used for profilometry of a hemispherical shaped object using the wavelength conversion technique, and (b) the emitted florescence pattern from the object obtained by the CMOS camera.	102
FIGURE 5.5: (a) A schematic of the fringe projection profilometry based on reflected light, and (b) a schematic of the fringe projection profilometry based on wavelength conversion.	104
FIGURE 5.6: (a) Calculated phase of the blue reflected light using a four-step phase shifting algorithm. (b) Calculated phase of the red fluorescence emitted light using a four-step phase shifting algorithm.	104

FIGURE 5.7: (a) Fourier spectrum of the phase component of the reflected blue signal, and (b) Fourier spectrum of the fluorescence red signal	105
FIGURE 5.8: (a) Unwrapped phase map constructed from the blue reflected pattern, and (b) unwrapped phase map constructed from the emitted red pattern.	106
FIGURE 5.9: A schematic of a heat induction technique using a fringe projection configuration.	110
FIGURE 5.9: Experimental Setup for profilometry of a black egg-holder shape object based on optical wavelength conversion from visible to deep infrared spectrum.	112
FIGURE 5.10: (a) Obtained image from a dark egg-holder shape object by the infrared camera, and (b) image from the dark egg-holder shape object by a conventional camera at visible spectrum.	112
FIGURE 5.11: (a) One dimensional profile of the heat pattern along the blue dotted line and the best fit polynomial to the profile, the green curve, and (b) the form-free profile of the pattern along the blue dotted line. The red plot is the best sinusoidal fit to the obtained heat pattern, (SNR = 0.309).	113
FIGURE 5.12: One-dimensional profile of the heat pattern along the blue dotted line and the best fit polynomial to the profile, the green curve, and (b) the form-free profile of the pattern along the blue dotted line. The red plot is the best sinusoidal fit to the obtained heat pattern, (SNR = 0.038).	113
FIGURE 5.13: Obtained heat patterns of a flat object at different time and the profile of each pattern compared with its best sinusoidal fit.	115
FIGURE 5.14: The sinusoidal heat pattern from one bump of the dark egg-holder shape object using the infrared Moire technique, and the reconstructed height map of the object.	116
FIGURE 5.15: The sinusoidal heat pattern from two bumps of the dark egg-holder shape object using the infrared Moire technique, and the constructed height map of the object.	117
FIGURE 6.1: Simple schematic for 3D thermal imaging of an object to detect non-uniformity.	124

CHAPTER1: INTRODUCTION

1.1. Introduction

Dimensional characterization of surface plays an important role in functionality of a part. Measuring the surface texture and form has significant importance in many industrial and biological applications. Recent development in manufacturing of more complex objects with high variety on raw materials, functions, and geometries demands for development of more precise measurement techniques. Also, the growing need for in-process testing to improve the quality of manufacturing process requires a fast, precise and potentially non-contact measurement technique. Optical-based surface topography measurement techniques have the advantage of being non-contact, non-destructive, fast, and highly accurate. These techniques avoid deformation and mechanical errors in measuring even highly delicate surfaces. The basic principle of optical-based surface measurement technique is to project light from an optical source onto an object and analyze the reflected or transmitted signal. Several optical instruments have been developed over the years for surface topography measurements, including laser and white light interferometry [1] [2], confocal microscopy [3] [4], confocal chromatic microscopy [5], Moire [6] [7] [8] [9] [10], structured light projection [11] [12], etc. Although the optical-based instruments are non-contact, fast and high resolution, there are still serious limitations in the metrology of objects using these types of instruments. We can divide these limitations into three main categories.

First, limitations that come from the inherent properties of the physical components used in the instruments. For example, the trade-off between the resolution and field of view of the imaging sensor can limit the measurement range.

Second, the limitations that comes from the intrinsic properties of the measurement method. For example, in interferometric-based techniques such as laser interferometers, Moire, and fringe projection techniques, there is always a phase ambiguity issue due to the periodic nature of the signals. The principle of these methods will be discussed in the detail in Chapter 2.

Third category is the limitations, which are related to the geometry or/and optical properties of the surface under measurement in combination with the system's characteristics. One such limitation, for example, could be easily experienced in metrology of complex objects (objects with free form geometry) using an optical instrument that utilizes a conventional 8-bit camera as its image acquisition unit. An 8-bit camera can distinguish the intensity range between 0 to 255 gray scales while the light reflecting back from a complex object can offer a much wider range than 8-bit. Therefore, some information of the reflected signal cannot be correctly recorded by the system, which results in an inaccurate and an unreliable measurement. Another example of such limitations occurs in metrology of objects that are composed of materials with specific optical properties. For example, transparent materials or highly absorbent materials have very low reflectivity; therefore an optical-based metrology instrument that uses a conventional imaging system cannot obtain enough information for reliable metrology of an object made from such materials.

Tremendous efforts have been directed over the years to tackle the first and second types of limitations in optical surface metrology tools. The main purpose of this research effort is to provide metrology solutions to solve the third type of limitations in the field of optical metrology. The main focus of this work is to provide solutions for more accurate and more reliable 3D profilometry of complex objects using fringe projection and laser interferometry techniques. This chapter will provide an overview of the techniques developed to overcome the challenges that fall within the first and the second type of limitations discussed above. Also, the problem associated with the limited dynamic range of imaging systems in metrology of complex objects, as an example of the third type of optical metrology tools, will be discussed. In chapter two, the principle of 3D profilometry of objects using fringe projection technique, and laser interferometry will be discussed. In Chapter 3, a novel technique called Spatially Varying Pixel Intensity (SVPI) is reported to enhance dynamic range of a fringe projection system with simulation and experimental results. In chapter 4, the effect of limited dynamic range in laser interferometers for metrology of objects will be discussed, and a modified Spatially Varying Pixel Intensity technique is introduced to enhance dynamic range in a Michelson laser interferometer. The experimental setup and results will be discussed in detail in this chapter. In Chapter 5, the effect of optical properties of the material in metrology of complex surfaces will be discussed. A novel technique called “3D Profilometry Based on Wavelength Conversion” is presented and supported by experimental results. In final chapter, Chapter 6, a summary of all the major achievements in the course of this study will be discussed, and some suggestions for future work will be given.

1.2. Limitations in Optical Metrology Associated with System Components

There are two distinct types of optical surface metrology instruments: i) those that measure over a large area from several millimeters to several meters, with spatial resolution of tens of micrometers to hundreds of micrometers. Moiré interferometry [6]-[10], fringe projection [12] and photogrammetry [13] [14] are in this category, and ii) instruments that measure over a small area up to a few millimeters with spatial resolution of 1 micrometer to sub nanometers. Coherence scanning interferometry [15] and confocal microscopy [3] [4] are two examples of this category of instruments.

Therefore metrology of objects with a large area, which carries low profile and high frequency features on top of them, is a challenge in the field of optical metrology. The problem is usually associated with the trade-off between the range of measurement, which is usually limited by the imaging system field of view, and the corresponding resolution of the measurement system, which is limited by the spatial sampling in the system.

One approach to maintain high spatial resolution over a large field of view (FOV) is to scan the object and obtain several images with smaller FOV and high spatial resolution, and then stitch the images together using an appropriate stitching algorithm. The stitching process might introduce several sources of errors in the measurement results, which need to be considered [16]. Also taking multiple images from the sample and stitching them together is a very time-consuming process.

Array microscopy is an alternative approach for solving the FOV and spatial resolution trade-off problem [17]. In this technique a 2D array of micro-optical systems is overlaying a 2D detector array, which enables the system to simultaneously obtain

several images from a different area of the object with high spatial resolution, figure 1-1. The obtained high-resolution images are stitched together to construct an image with large FOV and high spatial resolution.

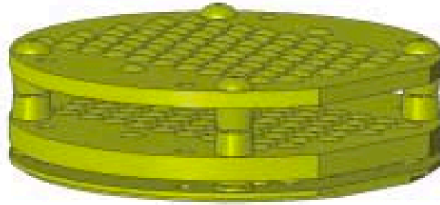


Figure 1.1: A 2D array of micro-optical systems overlaying a 2D array of detector, which enables the system to form a complete, large-format, high-resolution image [17].

Another approach for solving the FOV, spatial resolution trade off problem is to combine the two types of instruments (high spatial resolution instruments with small FOV and low spatial resolution instrument with large FOV). Dual Moiré and Laser Interferometry is a technique reported by M. Abolbashari. et al. [18]. In this technique coarse measurements with large field of view obtained from a Moire interferometer at different zoom levels have been combined with high-resolution and fine measurements obtained by a Michelson laser interferometer over a small field of view and shorter vertical range to construct large format high resolution objects. A schematic of the reported setup is shown in figure 1.2.

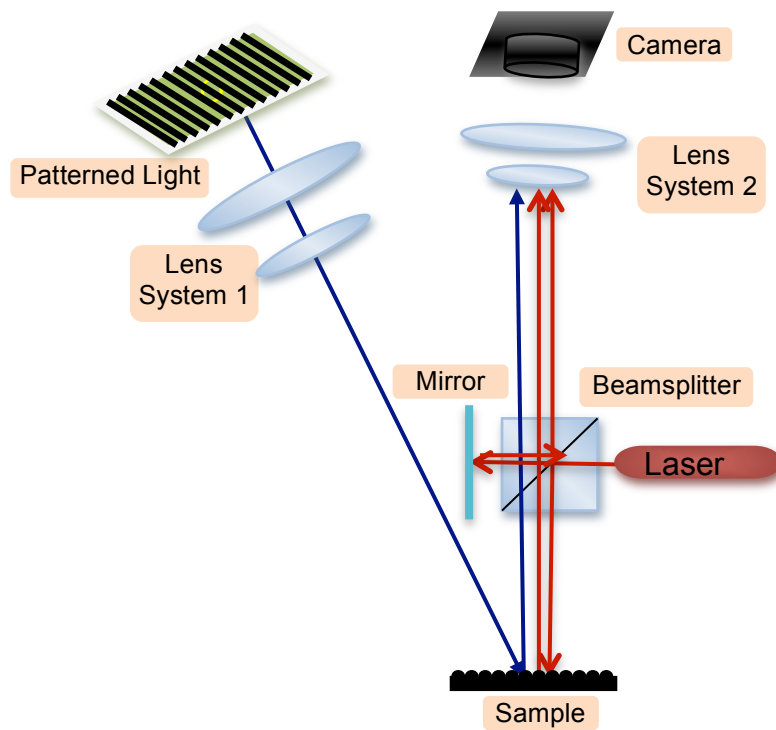


Figure 1.2: Schematic of the dual-moiré-laser interferometer [18].

1.3. Limitations in Optical Metrology Associated with the Intrinsic Nature of the Measurement Method

Interferometric based surface metrology techniques, such as laser interferometry, Moire, and digital fringe projection techniques are among the most powerful and important optical surface metrology tools. In these techniques the phase of the reflected or transmitted fringe pattern from the object is modulated by the surface topography. Therefore, by obtaining the phase distribution of the light one can extract the desired information from the object under the measurement. However, because of the periodic nature of such optical signals, the phase at a certain point is uniquely defined only in the principal value range of $(-\pi, \pi)$. In general, the true phase map can vary over the 2π

range, which causes discontinuous phase jump in the wrapped phase map if the phase modulation is greater than 2π . Several algorithms have been developed over the years to find the continuous phase map from the wrapped phase of the object. These algorithms are usually referred to as phase unwrapping techniques.

A simple approach to unwrapping the phase is to compare the phase at neighboring pixels, and by adding or subtracting integers of 2π to bring the relative phase of the neighboring pixels into the $[-\pi, \pi]$ intervals [19].

$$\phi(m, n) = \varphi(m, n) \pm 2\pi k \quad (1.1)$$

where, “k” is the integer multiples and called the wrapped counts.

In the mentioned unwrapping algorithm, a presumption of continuous phase map is made. However, in the real measurement condition, the presence of different types of noise such as low fringe contrast, shadow, fringe discontinuity, and variable reflectivity from the object surface may cause fringes to merge or break in some locations. The locations where the fringes merge or become isolated are called residues or discontinuity sources. In this situation, phase unwrapping becomes more difficult and highly path dependent. Several advanced unwrapping techniques have been developed over the years; they can be divided into three categories: i) global algorithms, ii) region algorithms, and iii) path-following algorithms.

In the global algorithm a global function, which is usually an error function, is defined. Then the algorithm tries to minimize the error using a least square regression model. FFT [20], multigrid technique [21] and L^p -norm method [22] are in this category. These types of algorithms are robust, but they are computationally extensive.

The region algorithms divide the image into sub regions. The phase of each sub region will be wrapped individually. Then the phase of all the sub-regions will be wrapped relative to each other until the entire phase is wrapped. The region algorithms can be sub classified into two groups: the tile-based [23], [24], [25] algorithms and the region-based [26], [27], [28] algorithms. These types of algorithms are faster than global algorithms, but they are less accurate and less robust.

In the path-following algorithms, a path is defined, and the unwrapping process is done through that path. This group can be sub-classified into two groups [23]: i) residue-compensation methods, and ii) quality guided path methods. The residue compensation algorithms search for residues and abrupt phase steps in the image. Then it generates branch cuts around them. The unwrapping path is then defined in such a way to avoid crossing the branch cuts. Goldstein unwrapping algorithm is in this category [29]. These algorithms are computationally efficient, but they are not robust.

The quality guided algorithm works based on unwrapping the highest quality pixels first, and unwrapping the lowest quality pixels last. The technique first defines a quality map, which is a matrix of values that defines the quality of each pixel on the image. The success level of the technique depends on how well the quality map is defined. These types of algorithms are very robust and usually computationally efficient [30]-[35].

1.4. Limitations Associated with Combined Object Properties and System Characteristics

Usually, optical surface metrology tools utilize imaging sensor arrays such as CCD or CMOS cameras for detection of optical signals. These cameras have given dynamic range of 8 or 16 bits. However, in some cases the dynamic range of light coming from the test object toward the imaging sensor is much wider than the dynamic range of the imaging sensor itself. For example, a conventional 8-bit camera can correctly record the intensity range values between 0 to 255 gray scale levels, and if the intensity level of signal reaching the camera is wider than this range (0-255) some intensity information of the light cannot be accurately recorded, which limits system's application for such objects.

The large variation in the intensity of the light reflecting from the surface can be the result of the intrinsic properties of the signal itself. For example, in laser interferometry, when two Gaussian beams are superimposed, the resultant interferogram has a wide range with a bright central part, which fades into darker region when moving away from the center. There are methods to generate a flat beam profile to avoid this problem, but such a beam profile is not always the optimum option. Therefore, an optical metrology tool that utilizes Gaussian laser beam as its light and a conventional camera as its image acquisition unit could potentially have a dynamic range problem.

Also, large variation in the intensity of light reflecting from the object might be the result of shape and/or composition of the object under measurement. For example, in integrated optical circuits the presence of metallic and non-metallic regions generates significantly different levels of optical reflections, which makes the light collection from these regions very difficult in a single image. Also, specular objects with spherical or free-form shapes reflect light in very wide range of angles from normal to near vertical,

which make collection of the reflected light from this object very difficult using a single imaging sensor. In both cases, the intensity level of the light coming from the test object varies above the dynamic range of most conventional cameras. Hence, the true intensity value of the incoming light cannot be entirely recorded in a single shot. As a result, the correct phase information of the detected signal cannot be obtained and consequently the correct height variation of the object under measurement cannot be reconstructed. Hence, developing an imaging technique, which enhances the dynamic range in interferometric based systems, would be very useful for a reliable demodulation of the interference pattern and has many applications.

In the rest of this section, we first review the principle of dynamic range enhancement in digital photography. Then the previously developed techniques to enhance dynamic range in fringe projection and laser interferometers will be discussed.

1.4.1. High Dynamic Range Photography

High Dynamic Range Imaging (HDRI or HDR) is a set of methods used in imaging to capture a greater range of intensity levels between the brightest and darkest areas on an image than available with standard methods. It has been shown that a high dynamic range image can be constructed by fusing multiple differently exposed images of the same scene [36], [37], [38]. The idea of fusing multi-exposure images is first introduced by Charles Wyckoff in the early nineteen sixties well before the age of digital image processing [39]. He developed a high dynamic range film, called XR film (extended range film) by composing three layers of same spectral sensitivity but different intensity sensitivity (for example the bottom layer had very low sensitivity to light intensity and top layer had much more sensitivity to light intensity). As a result, he was able to record a

very wide range of intensity information of the scene on his film. Then he printed his gray scale picture onto color paper to separate the differently exposed parts of the scene by mean of colors.

The same principle is then applied in digital imaging sensor. Multiple images with different exposures are obtained from the same scene. At low exposures, information from the bright zones can be properly recorded and at high exposures, information from the dark zones can be preserved. The information obtained from differently exposed images can be combined to construct a high dynamic range image from the target scene. The quality of the composed HDR image depends on the number of images and the chosen exposure for each image. In order to have a better understanding of how many images and at what exposures are required to construct a high-quality HDR image by fusing multiple exposed images, we need to understand what the camera measures.

In general, the scene radiance transfers to the pixel value by a nonlinear mapping called response function. The nonlinearity comes from several factors, such as vignetting, lens fall-off, the sensitivity of the detector, and the electronics of the camera.

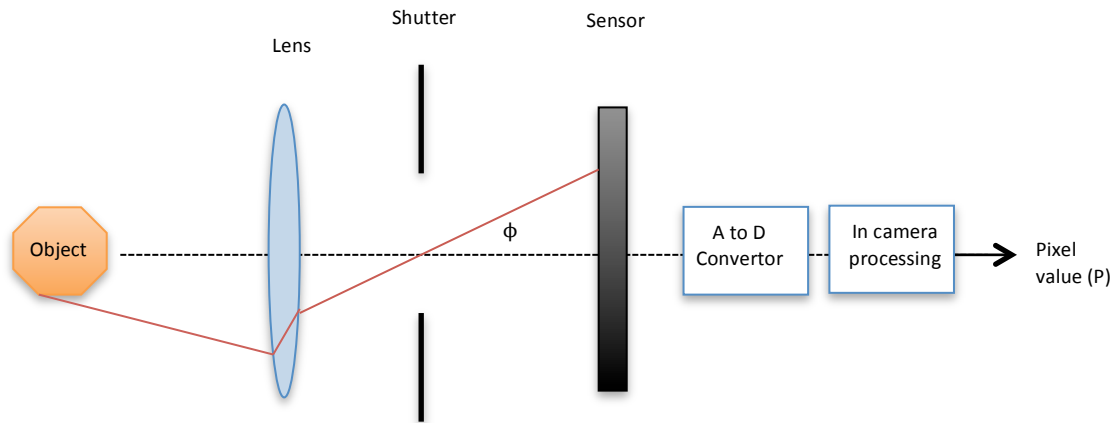


Figure 1.3: A schematic of a digital camera, which illustrates how is a scene radiance transformed to pixel values.

The scene radiance, r , is attenuated by passing through the lens system of the camera. Figure 1.3, The irradiance received on the imaging sensor can be calculated by the following equation:

$$E = r \frac{\pi}{4} \left(\frac{D}{f}\right)^2 V(\varphi) \quad (1.2)$$

where, E is the irradiance received by the sensor, " D " is the lens diameter, " f " is the lens focal length, and $V(\varphi)$ is the vignetting coefficient, which can be approximated by:

$$V(\varphi) = \cos^4(\varphi) \quad (1.3)$$

where φ is the angle between the chief ray and the optical axis.

The shutter can control the total amount of time, which the sensor is exposed to the scene. Therefore the total amount of light received on the imaging sensor during an integration time of Δt , or in the other words the exposure of the camera is:

$$I = E\Delta t \quad (1.4)$$

Typical sensors such as CCD and CMOS are designed to produce an electrical signal, which is proportional to the sensor exposure up to a saturation level. Above the saturation level, the sensor cannot distinguish between different exposure values. The produced electrical signal is converted to integer values using an analog to digital convertor (ADC).

This step introduces quantization noise to the recorded data. Then the digital values are scaled and transformed by a gamma function to properly display on a monitor.

Also if the sensor exposure is less than a certain level, the correct signal information will be lost in the sensor noise. Generally, there are three main sources of noise associated with a typical CCD and CMOS cameras, the photon shot noise, dark current noise, and read noise. The photon shot noise, first introduced in 1918 by Walter Schottky [13], exists because the photon arrives at random intervals at any detector. Therefore there is always an uncertainty of the number of photons collected over a given period of time by the camera. Dark current noise is caused by the statistical variation of the number of thermally generated electrons due to the heating of the camera sensors. Cooling the sensors may reduce it. Other types of noise that may occur during the amplification and quantization of signals are collectively referred to as read noise, which may be minimized by careful design of camera circuitry.

Regardless of the individual factors involved in nonlinearity in the imaging process, we can define the camera response function, which converts the sensor exposure to the image brightness as follow:

$$M = f(I) \quad (1.5)$$

where M is the intensity value of each pixel on the monitor, and f is the camera response function. The non-linear mapping defined by the camera response function is an intentional process, which enables the camera to compress a wide range of irradiance values into a fixed range of measurable image brightness. The response function of each camera is the individual characteristic of that camera that is set by the manufacturer.

By having the response function of the camera, we can find the irradiance received by each pixel of the imaging sensor using equation below:

$$E_{ij} = \frac{1}{\Delta t_j} f^{-1}(M_{ij}) \quad (1.6)$$

where, f^{-1} is the inverse of the camera response function and Δt_j is the exposure time, and M_{ij} is the intensity value of the obtained image.

Therefore, by taking multiple images at different exposure time, multiple values can be obtained for each individual pixel using equation 1-6. A high dynamic range image can be obtained by selecting the best value of the irradiance for each pixel using all the obtained irradiance by differently exposed images. In general a high dynamic range map can be constructed by combining the reconstructed irradiance values of each pixel using,

$$E_i = \frac{\sum_j E_{ij} \omega(M_{ij})}{\sum_j \Delta t_j} \quad (1.7)$$

where $\omega(M_{ij})$ is some weighting criterion. Several algorithms have been developed to show how to combine differently exposed images to generate HDR images. These algorithms all have the same basics as discussed above, however they differ in the choice

of weighting criterion. [40] [41] [42] [43]. Figure 1-4 shows a simple schematic of high dynamic range imaging using differently exposed images.

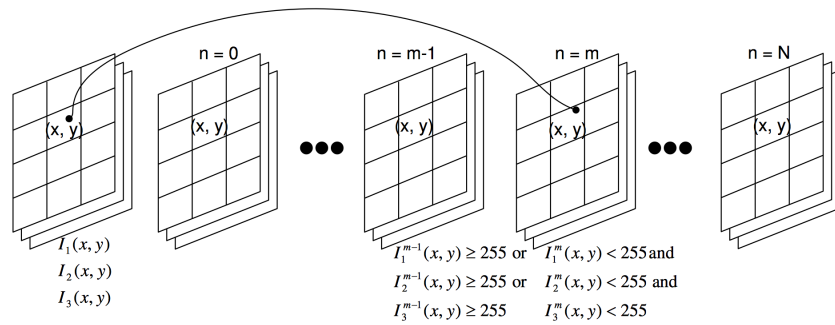


Figure 1.4: Formation of a high dynamic range image using a sequence of images with different exposure [43].

Two aspects need to be considered here: i) the number of images needed to recover the camera's response function, and ii) the number of images required to construct a high quality HDR image. Debevec and Malik [36] showed that two images are enough to recover the camera response function providing that they cover a wide range of radiance values. However to construct a high quality HDR image, we need as many images to insure each pixel falls at least in one image in the working range, of the imaging system [40]. In general, if the dynamic range of the scene is "D" and dynamic range of the imaging system is "d", the minimum number of images required for constructing a HDR image is $N = \frac{D}{d}$.

1.4.2. Dynamic Range Enhancement In Interferometric Based Technique

The intensity variation of an interferogram may be much wider than the gray-scale level, which can be recorded by a conventional camera. As stated before, in laser interferometry when two Gaussian beams are superimposed, the resultant interferogram has a wide intensity range, and when combined with the wide range of reflections from a curvilinear object the overall range of the optical signal reaching the sensor array could be much larger than the sensor's range. If we select the camera exposure time to correctly capture the dark zones then the details in the bright regions are lost by overexposure. Likewise, if the integration time is set to capture the bright zones correctly, then the underexposed dark regions are lost in sensor noise.

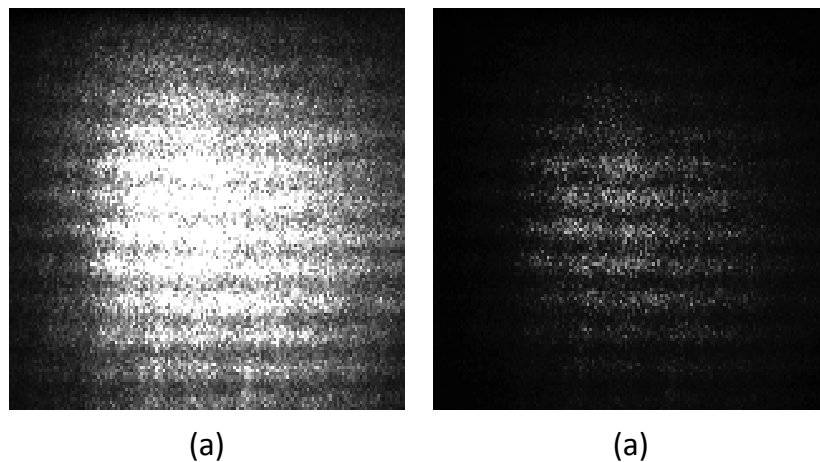


Figure 1.5 An interference pattern obtained from a Michelson laser interferometer with two different exposure times.

The correct phase information of the pattern cannot be extracted under such conditions. Therefore, developing a method to enhance the dynamic range in interferometric based systems would be very useful for a reliable demodulation of the interference pattern.

Several methods have been developed over the years to overcome the limited dynamic range problem of cameras in interferometric based systems. One technique proposed by Yoshinori et al is called ‘High dynamic range scanning’ [44]. This technique utilizes the conventional differently exposed image fusing concepts as discussed in section 1.4.1, where a sequence of fringe images are obtained from the surface at different exposure times. This technique produces the HDR interferogram based on obtaining the response function of the imaging system through a calibration process. Once the response function is calculated, the proportional true value of each pixel can be computed and based on that, a high dynamic range image can be constructed [45] [46] [47] [48].

Another technique proposed by Vergas et al. [49] enhances the dynamic range of an interferometry imaging system by acquiring multiple images from the stationary sample at different exposure times and computing the modulation depth for each fringe pattern $\gamma(x,y)$ through a normalization algorithm. For each single exposed pattern, in the regions where the modulation depth has large values, the fringe pattern is not overexposed nor underexposed. In the opposite case, if the modulation map has low values the corresponding fringe pattern is not reliable at these points and the technique will not use these values in constructing the HDR interferogram. Although this technique does not require computing the response function of the camera, it requires computing the modulation map for differently exposed images, which is a time consuming process.

Another high dynamic range imaging technique in fringe projection was proposed by Zhang et al [50]. In this technique a high dynamic range image was acquired by adjusting the intensity of some regions of the pattern using a DLP based on the feedback from the reflected pattern of the sample captured by the camera. In this work the dynamic range of the fringe projection system is improved with a single shot, however, since their enhancement technique is done in one step it cannot compensate for object with very wide variation of reflectivity. In addition, compensating in one-step could mistakenly decrease the intensity of pixels that have high intensity due to pixel bleeding effect and decrease the fringe contrast. In this research effort, a new technique called Spatially Varying Pixel Intensity technique has been developed to enhance dynamic range imaging in both laser interferometry and digital fringe projection profilometry. The principle of this technique for applications in digital fringe projection and laser interferometry will be discussed in detail in chapters 3 and 4.

CHAPTER 2: 3D PROFILOMETRY OF OBJECTS USING FRINGE PROJECTION AND LASER INTERFEROMETERS

2.1. Fringe Projection Profilometry Technique

Fringe projection is one the most important three dimensional measurement techniques, which offers the advantages of being non-contact, full-field acquisition, high resolution, and fast data processing. The technique has a wide range of applications in both the industrial and biomedical fields such as characterization of MEMS components [51] [52], vibration analysis [53] [54], reverse engineering [55] [56] [57], quality control of circuit board manufacturing [58] [59] [60], biometric identification applications such as 3D facial reconstruction [61] [62], 3D intra-oral dental measurement [63], non-invasive 3D imaging and monitoring of vascular wall [64], human body shape measurement for shape guided radiotherapy treatment [65] [66], inspection of wounds [67] [68], and skin topography measurement for use in cosmetology [69] [70] [71].

A typical fringe projection profilometry system consists of a projection unit, an image acquisition unit, and a processing unit. A schematic of a fringe projection profilometry system is shown in figure 2.1.

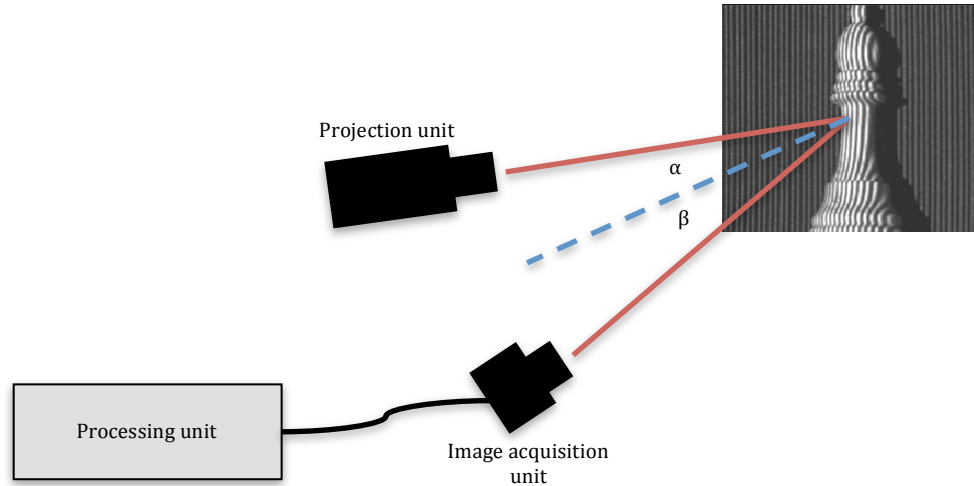


Figure 2.1: A schematic of a typical fringe projection profilometry system.

The projection unit projects a structured pattern (usually a sinusoidal) to the test object at a given angle. Several methods have been developed for generating and projecting patterns [72]-[84]. In general the projector units can use either a coherent light source such as a laser source combined by an interferometer to generate high frequency fringes [72] [73] or use an incoherent light source such as LED combined with a grating [74] [75] or simply use a digital optical projector to project a computer based generated fringes [81] [82] [83] [84].

The reflected pattern from the test object is a deformed pattern, which the height information of the object is embedded in the phase distribution of the reflected light as the result of triangulation. Triangulation causes variation in the periodicity of the fringe pattern viewed by the imaging system as the result of relative height variation on the test object surface.

In order to explain the basic operation of a fringe projection system first consider the projection unit, which generates equally spaced fringes of spatial period of d_p , illuminating a reference flat test object at angle α relative to the surface normal, figure 2.2.

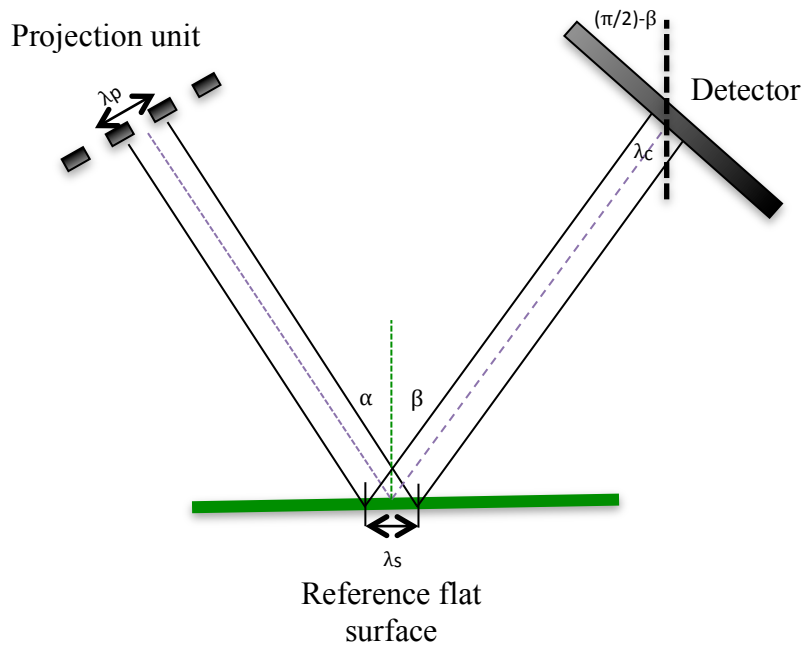


Figure 2.2: A fringe projection triangulation setup with a flat reference surface.

The spatial period of the fringes on the surface of the reference flat plate is:

$$\lambda_s = \frac{\lambda_p}{\cos \alpha} \quad (2.1)$$

If the image acquisition unit views the reflected pattern at angle β relative to the surface normal, the obtained spatial period will be:

$$\lambda_c = \frac{\lambda_p \cdot \cos \beta}{\cos \alpha} \quad (2.2)$$

The spatial period of the reflected pattern viewed by the imaging system alters with the system geometry. Now consider if an object replaces the reference flat surface with a given surface profile of h as shown in figure 2.3.

The light wave reflected from each point of the object incident the detector with a shift relative to the reflected light from the reference flat surface due to the object surface profile.

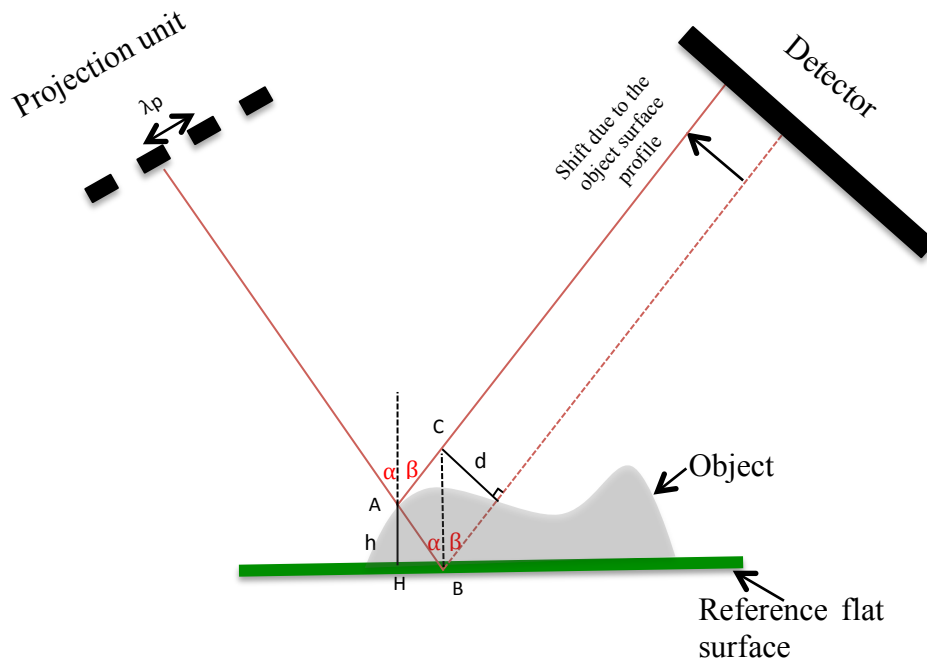


Figure 2.3: Schematic of a fringe projection triangulation setup for 3D profilometry of an object

As a result, a shift in the phase of the fringe pattern on the image plane occurs, which can be expressed in terms of the displacement “d” with the following relationship:

$$\varphi = \frac{2\pi}{\lambda_c} \cdot d \quad (2.3)$$

Therefore, by finding the relation between "d" and "h" at each point the relation between phase of the reflected light and the height information of the object can be obtained. The following calculations show the steps to find the relation between "d" and "h".

In AHB triangle we have,

$$AB = \frac{h}{\cos \alpha} \quad (2.4)$$

similarly for the triangle ABC,

$$\frac{AB}{\sin \beta} = \frac{BC}{\sin (\alpha + \beta)} \quad (2.5)$$

and

$$d = OB \cdot \sin \beta = \frac{h}{\cos \alpha} \cdot \sin (\alpha + \beta) \quad (2.6)$$

As the result we obtain:

$$\varphi = \frac{2\pi}{\lambda_c} \cdot \frac{h}{\cos \alpha} \cdot \sin (\alpha + \beta) \quad (2.7)$$

or

$$\varphi = \frac{2\pi}{\lambda_{eff}} \cdot h \quad (2.8)$$

where, $\lambda_{eff} = \lambda_p \cdot \frac{\cos \beta}{\sin(\alpha + \beta)}$ is the equivalent wavelength of the fringe projection system that depends on the spatial period of the projection pattern and the geometry of the system. Therefore the phase of the reflected fringe pattern obtained by the imaging system at each point directly depends on the height distribution of the object at a specific point. For a two dimensional image:

$$\varphi(x, y) = \frac{2\pi}{\lambda_{eff}} \cdot h(x_o, y_o) \quad (2.9)$$

where, x, y are the image coordinates, and x_o, y_o are the objects coordinate.

In general the intensity distribution of the acquired fringe pattern obtained by the imaging system can be described as:

$$I(x, y) = I_0(x, y) \{ [1 + \gamma(x, y) \cos(\varphi(x, y))] \} \quad (2.10)$$

where $I_0(x, y)$ is the background intensity distribution and $\gamma(x, y)$ is the modulation depth of the fringes in the field of view, which can be simply described as the fringe contrast. For simplicity we can write the intensity distribution of the acquired fringe pattern as follow:

$$I(x, y) = a(x, y) + b(x, y) \cos(\varphi(x, y)) \quad (2.11)$$

where $a(x, y) = I_0(x, y)$, and $b(x, y) = I_0(x, y)\gamma(x, y)$.

The processor unit of the fringe projection profilometry system then analyzes the obtained intensity distribution of the fringe pattern to extract the modulated phase of the pattern, $\varphi(x,y)$, and consequently calculates the height distribution of the object using equation 2.8.

Fringe analysis is the key step in the fringe projection profilometry technique, which has significant influence on the overall performance of the system. In general, fringe analysis techniques can be divided into two main categories: i) temporal fringe analysis techniques, and ii) spatial fringe analysis techniques. In temporal fringe analysis techniques a sequence of images from a series of phase-shifted fringe patterns are required. The phase-shifting method and the fringe-scanning method belong to this category [85] [86] [87]. In spatial fringe analysis technique a high-frequency spatial carrier is required for a measurement. The main advantages of this type of technique is that they can extract the phase from a single shot interferogram; therefore they are usually fast and are good candidates for dynamic processes. Fourier transforms based methods (FTM) [88] [89] [90] [91] and the spatial carrier phase shifting methods [92] [93] are two most popular types of spatial phase analysis techniques. In the following section of this chapter the principles of each category of fringe analysis technique will be discussed.

2.1.1. Temporal Fringe Analysis Technique

The phase-shifting method is one of the most popular temporal fringe analysis techniques. In this method a series of fringe patterns, N , in which their initial phases are shifted by a known step of $\delta\psi$ are sequentially projected to the test sample, and their reflected patterns are acquired by the imaging system.

For the sampling number $k=1,2,3\dots N$, the phase shift value is usually defined by:

$$\delta\psi = \frac{2\pi}{N} \quad (2.12)$$

Therefore the intensity distribution of the K^{th} fringe pattern obtained by the imaging system can be defined as:

$$I_k(x, y) = a(x, y) + b(x, y) \cos(\varphi(x, y) + (k - 1) \cdot \delta\psi) \quad (2.13)$$

The phase distribution of the fringe pattern can be calculated by using the intensity distribution of the acquired images using the following equation:

$$\tan(\varphi(x, y)) = \frac{\sum_{k=1}^N I_k(x, y) \sin[(k - 1) \cdot \delta\psi]}{\sum_{k=1}^N I_k(x, y) \cos[(k - 1) \cdot \delta\psi]} \quad (2.14)$$

For example, in a four-step phase shifting, $N = 4$, and $\delta\psi = \frac{\pi}{2}$, the phase distribution can be calculated by:

$$\varphi(x, y) = \tan^{-1}\left(\frac{I_4(x, y) - I_2(x, y)}{I_3(x, y) - I_1(x, y)}\right) \quad (2.15)$$

The spatial resolution of the system is limited by the number of the pixels on the imaging system. Also, the accuracy of the system can be improved by increasing the sampling number. In general, as the sampling number increases, the random noise in the system decreases by factor of $\frac{1}{\sqrt{N}}$, which results in a more accurate and more reliable measurement. On the contrary, since the technique requires taking multiple images at different times, it is very sensitive to any vibration in the environment; therefore the

phase-shifting technique is not a suitable fringe analysis technique for the measurement of a moving object.

2.1.2. Spatial Fringe Analysis Technique

In dynamic applications, where the height distribution of the test object is constantly changing, it is highly desirable to have a fringe analysis technique, which can calculate the phase distribution from only one captured image. In the spatial fringe analysis technique, a high frequency, equally spaced fringe pattern, called carrier fringe, $f_0(v_{0x}, v_{0y})$, is superimposed with the modulated phase. The intensity distribution of the acquired pattern can be written as:

$$I(x, y) = a(x, y) + b(x, y) \cos (2\pi(v_{0x}x + v_{0y}y) + \varphi(x, y)) \quad (2.16)$$

where, $\varphi(x, y)$ deforms the equally-spaced carrier frequency. The most common technique for the spatial analysis of carrier fringe pattern is the Fourier transform method. The following calculations show the necessary steps required for phase extraction from equation 2-16 using the Fourier transform technique.

The cosine term in equation 2-16 can be written as a summation of two exponents as shown in the following equation,

$$I(x, y) = a(x, y) + c(x, y)e^{2\pi i(v_x x + v_y y)} + c^*(x, y)e^{-2\pi i(v_x x + v_y y)} \quad (2.17)$$

where,

$$c(x, y) = \frac{b(x, y)e^{i\varphi(x, y)}}{2} \quad (2.18)$$

and

$$c^*(x, y) = \frac{b(x, y)e^{-i\varphi(x, y)}}{2} \quad (2.19)$$

Taking a two-dimensional Fourier transform from equation 2-19, we will have:

$$FI(v_x, v_y) = A(v_x, v_y) + C(v_x - v_{0x}, v_y - v_{0y}) + C^*(v_x + v_{0x}, v_y + v_{0y}) \quad (2.20)$$

where $A(v_x, v_y)$ is the spectrum of the background illumination, which is usually considered as the background noise, or DC noise. $C(v_x - v_{0x}, v_y - v_{0y})$ and $C^*(v_x + v_{0x}, v_y + v_{0y})$ are the spectra of the deformed carrier fringes. By filtering around either "C" or "C*" term and shifting it toward the origin, we can eliminate the spectrum of the carrier fringe, and isolate the term "C" or "C*", which contains only the spectrum of the modulated phase. By applying a two dimensional inverse Fourier transform on the filtered spectrum we can reconstruct the $c(x, y)$ or $c^*(x, y)$, and consequently calculate the modulated phase, $\varphi(x, y)$. For example, consider $c(x, y)$ is the term which is reconstructed; the real and imaginary parts of this term can be written as follow:

$$Re\{c(x, y)\} = b(x, y) \cos(\varphi(x, y)) \quad (2.21)$$

$$Im\{c(x, y)\} = b(x, y) \sin(\varphi(x, y)) \quad (2.22)$$

Therefore,

$$\varphi(x, y) = \tan^{-1}\left(\frac{Im\{c(x, y)\}}{Re\{c(x, y)\}}\right) \quad (2.23)$$

As the result of the trigonometric arctangent function, the phase is mathematically limited to the interval $[-\pi, \pi]$. The generated phase map at this step is usually referred to as the wrapped phase map. In general, the true phase map can vary over the 2π range, which causes discontinuous phase jump in the wrapped phase map. Therefore an additional procedure is required to find continuous phase distribution, which is referred to as phase unwrapping. An overview of phase unwrapping techniques was provided in chapter 1. As discussed before in chapter 1 the quality-guided algorithms are among the most robust and time efficient unwrapping algorithms. Therefore in our experimentation for 3D profilometry of objects using fringe projection and laser interferometry techniques we have used the quality-guided algorithm which uses short time Fourier transform (STFT) quality map proposed by Qian Kemao [94], for unwrapping the phase of the signal.

2.2. Interferometry

2.2.1. Basics of Interferometry

Optical interferometers have been widely used in a variety of precision measurement techniques. Optical interferometers work based on the interference phenomena produced by superposition of two or more light waves. When two light waves propagate in the same medium, they interact with one another, both constructively and destructively. Providing that the light waves have a degree of coherence and same state of polarization, the resultant wave creates an intensity distribution with bright and dark regions, which is called fringe pattern.

A light wave can be considered as a transverse electromagnetic wave propagating along the z direction, and mathematically can be described as:

$$E(x, y, z, t) = a \cos(\omega t - kz) \quad (2.24)$$

where a is the amplitude of the light wave, $\omega = 2\pi\nu$ is the angular frequency, ν is the light frequency, $k = \frac{2\pi}{\lambda}$ is the propagation constant, and λ is light wavelength. The term " $\omega t - kz$ " is the phase of the light wave, which varies as a function of time and distance. A wavefront is represented by a surface of constant phase at any specific time. Equation 2-24 can be also written in the complex format as follow:

$$E(x, y, z, t) = \text{re}[A \exp(i\omega t)] \quad (2.25)$$

where $A = a e^{-i\frac{2\pi z}{\lambda}} = a e^{-i\varphi}$ is known as the complex amplitude.

Consider two light waves, which have the same frequency and state of polarization, are propagating in the same direction. The resultant intensity at each point is the square of the sum of the complex amplitude of the two waves:

$$I = |A_1 + A_2|^2 \quad (2.26)$$

$$= (A_1 + A_2)(A_1 + A_2)^* \quad (2.27)$$

$$= |A_1|^2 + |A_2|^2 + A_1 A_2^* + A_1^* A_2 \quad (2.28)$$

$$= I_1 + I_2 + 2\sqrt{I_1 I_2} \cos \Delta\varphi \quad (2.29)$$

where I_1 and I_2 are the intensities of each light wave, and $\Delta\varphi = \varphi_1 - \varphi_2$ is the phase difference between them. If the waves have the same initial phase, the phase difference corresponds to an optical path length difference:

$$\Delta P = \left(\frac{\lambda}{2\pi}\right) \Delta\varphi \quad (2.30)$$

If the phase difference varies linearly across the field of view, the intensity of the mixed light waves varies sinusoidally based on equation 2-29, which results in alternating black and white bands, known as a fringe pattern.

The intensity of the fringe pattern varies between two limits, I_{max} , for bright fringes, and I_{min} , for dark fringes. The visibility, V , is defined as a contrast of fringe pattern, and mathematically is written as:

$$V = \frac{I_{max} - I_{min}}{I_{max} + I_{min}} \quad (2.31)$$

If $I_{max} = 1$, and $I_{min} = 0$, then the contrast of fringe pattern is maximum.

2.2.2. Interferometry Techniques For Surface Topography Measurement

When a test object is inserted across the field of view of one of the interfering light waves, it will introduce a change in the phase of the light's wavefront. Therefore the height distribution of the test object modulates the wavefront of the light waves. When the light with distorted wavefront mixes with the other, non-distorted light wave, a fringe pattern will be produced, in which the height information of the test object is embedded in the phase distribution of the interference pattern. Therefore the surface profile of the

object can be obtained by proper analysis of the fringes as described in section 2.1 followed by the unwrapping technique to avoid discontinuity.

The most common types of laser-based interferometers used for surface topography measurements are Michelson interferometers, Mirau interferometers, and Linnik interferometers. A brief description of each interferometer is given in the following subsections.

2.2.3. Michelson Interferometers

A typical Michelson interferometer used for surface topography measurement consists of a laser source, a beam collimator, a beam splitter, a reference mirror, imaging system, and the test object, figure 2.4. The height information of the test object deforms the wavefront of the reflecting light coming back from path 1, while the reflecting light coming back from the reference mirror has not changed. The two reflecting wavefront will interfere with each other once they pass through the beam splitter, and create a fringe pattern, which is phase modulated based on the height variation of the test object.

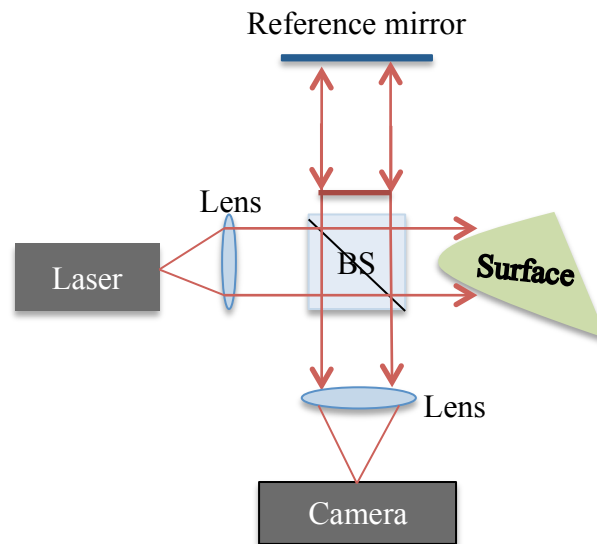


Figure 2.4: A schematic of a Michelson laser interferometer for surface measurement.

2.2.4. Mirau Interferometer

A Mirau interferometer is a compact form of a Michelson interferometer. The light source and the camera are in the same location, and the measurement beam and the reference beam have almost the same optical path length difference. As the result a Mirau interferometer is good for both laser interferometry and white light interferometry. A schematic of a Mirau interferometer is shown in figure 2.5.

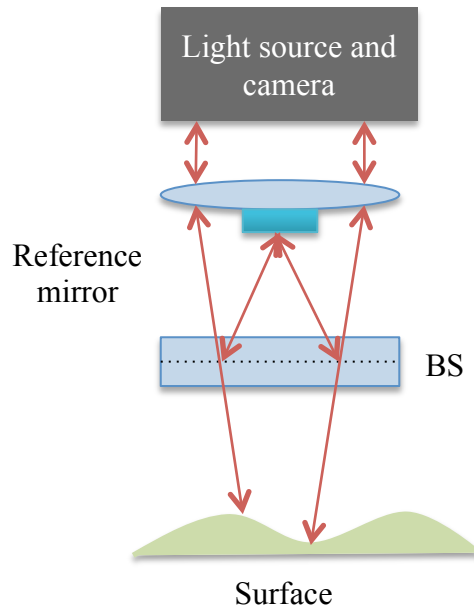


Figure 2.5: A schematic of a Mirau interferometer.

2.2.5. Linnik Interferometes

Linnik interferometers also follow the same principle as Michelson interferometers. The only difference is they use a high magnification objective lens in front of both reference mirror and the object to focus the light for a high-resolution measurement. These types of interferometers are good for the observation of small details on the surface. A schematic of this interferometer is shown in figure 2.6.

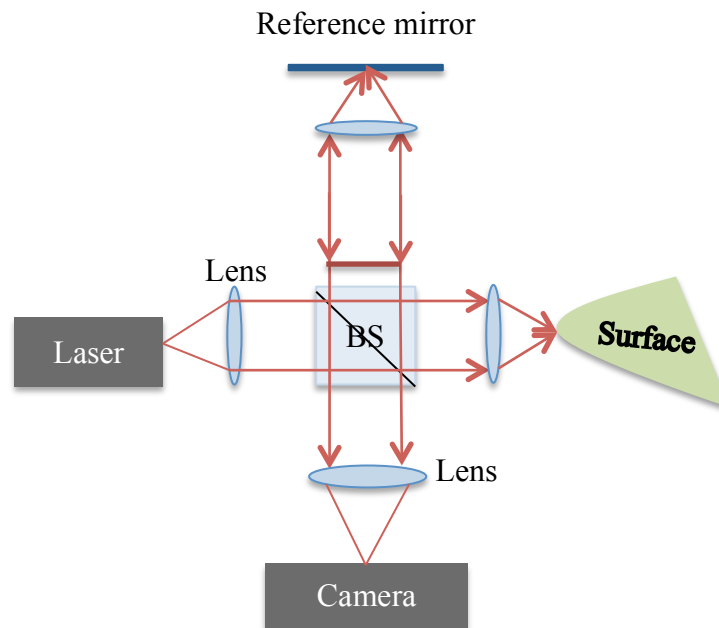


Figure 2.6: A schematic of a Linnik interferometer.

In all of the above interferometers, the obtained interferogram will be transferred to the computer for further processing to derive its phase information. As discussed in chapter 1, usually the resultant interferogram will have a higher level of intensity variation in comparison with what can be captured by a camera as the result of the Gaussian distribution of the laser source or/and the shape of the object under measurement. Therefore it is possible to lose some useful information of the interferogram and consequently the object due to the underexposed or saturated pixels on the interferogram. Figure 2.7 shows an interferogram obtained by a Michelson interferometer from a curved surface. The area of the interferogram, which is associated

with high reflection from the object, is saturated. This leads to serious limitations in the metrology of such surfaces using a laser interferometer.

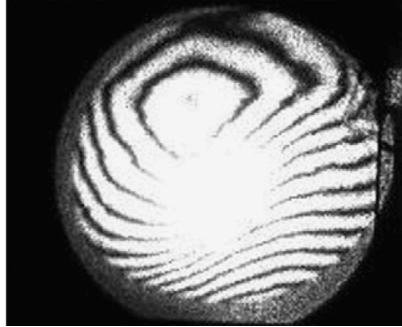


Figure 2.7: An interferogram obtained by a laser interferometer from a surface [49].

In chapter 3 and 4 Spatially Varying Pixel Intensity technique will be introduced as a tool to enhance dynamic range in digital fringe projection 3D profilometry and laser interferometry systems.

CHAPTER 3: DYNAMIC RANGE ENHANCEMENT IN 3D PROFILOMETRY OF FREE FORM OBJECTS USING DIGITAL FRINGE PROJECTION

3.1. Introduction

As discussed in chapter 1 limited dynamic range of conventional cameras causes difficulties in optical metrology of objects with wide variation in their optical reflectivity due to either their compositions or forms. For instance, metallic objects with steep slopes have a much higher level of intensity variations in their reflections compared to what can be captured by the 0-255 gray intensity range level of conventional cameras. As a result, reflected patterns taken by conventional cameras lose some information from such surfaces.

One powerful technique to obtain a 3D profile of an object is the digital fringe projection technique [51]-[71]. The details of the digital fringe projection technique were discussed in chapter 2. In general a simple setup to apply fringe projection is to project a fringe pattern onto the object and observe the reflected pattern by a camera from another direction. The reflected pattern is a deformed fringe pattern, which has the height information of the object embedded in its phase distribution. However, as mentioned before, dynamic range can be a problem in many situations. For example, figure 3.1(a) shows the image of a metallic ball from a fringe projection setup at low exposure time. Only areas with strong reflection toward the camera (tip of the metal ball) can provide measurable optical signal, while light reaching the camera from other regions of the object is extremely weak. Thus, sufficient information from the illuminated object is not

available to obtain surface topography of the object. As we increase the exposure time, figure 3.1(b), patterns reflected from sides of the ball with low reflection toward the camera become visible while pixels corresponding to areas with higher reflection toward the camera become saturated. Therefore the corresponding phase and intensity information of those areas (saturated pixels) are not measurable.

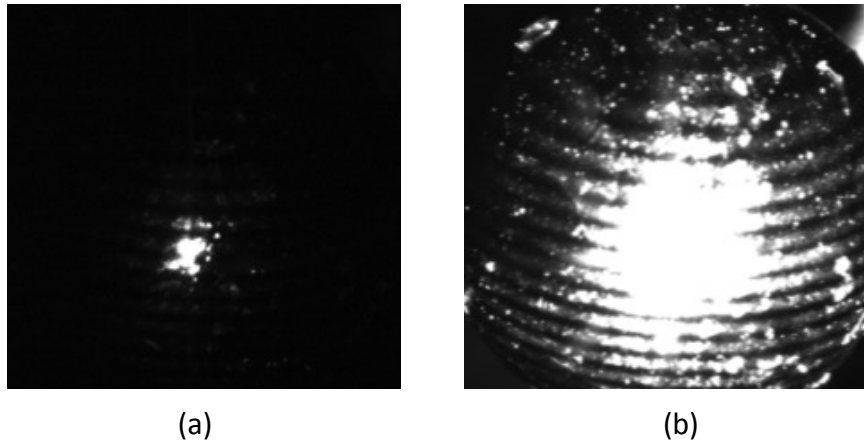


Figure 3.1: (a) Reflected fringe pattern captured by the camera from the metallic ball with exposure time = 5 ms, and (b) reflected pattern of the same sample with exposure time = 1 s

In this chapter we introduce a new technique called ‘Spatially Varying Pixel Intensity’ (SVPI), which can enhance the dynamic range in a fringe projection system by recursively adjusting the intensity of the projected pattern at the pixel level. This technique improves the dynamic range of the imaging system with no physical modification in the fringe projection systems.

In section 3.2 the measurement method will be discussed in detail. The proposed technique is simulated using a Matlab code and the results of the simulation discussed, in section 3.3. To implement the concept experimentally, we have used different setups for objects with different dimensions, ranging from tens of micrometers to tens of centimeters. In section 3.4 we describe use of a calibration ball with couple of millimeters diameter as the object under measurement. Afterwards, in section 3.5, we present the SVPI technique when applied on a series of solder bumps (diameter range of tens of micrometers) to measure the 3D profile of solder bumps designed for flip chip bonding, and finally in section 3.6, we present results when this technique has been applied to measure the 3D profile of a spherical object with dimension of tens of centimeters.

3.2. SVPI Measurement Method in Digital Fringe Projection Profilometry

The goal of SVPI technique is to control the irradiance of each pixel on the camera by repeatedly adjusting the intensity of the projection pattern at pixel level. Therefore the algorithm needs to adjust the intensity of each pixel on the projector based on the intensity received to the pixel/s of the camera. As the result, the first step in the SVPI technique is to find the geometrical alignment between the projector and camera's pixels.

In the case of the planer imaging, in which the object under the measurement is a uniform planer object, a geometric transformation function can transform features from the camera coordinate to the projector coordinate by a linear approximation. This kind of approximation assumes that the ratios of length and angle information are preserved between the camera, and the projector coordinates. Each point on the camera's image plane can be traced back to the projector's image plane by a rotational and scaling matrix

plus a translational vector using equation 3.1. A simple schematic of the system is shown in figure 3.2.

$$P_{ij} = T_{ij}^{cp} \times C_{ij} + S_{ij} \quad (3.1)$$

where, $P_{ij} = \begin{bmatrix} x_{pi} \\ y_{pi} \end{bmatrix}$ is the projector pixel's coordinate, $C_{ij} = \begin{bmatrix} x_{ci} \\ y_{ci} \end{bmatrix}$ is the camera pixel's coordinate, $T_{ij}^{cp} = \begin{bmatrix} a & b \\ c & d \end{bmatrix}$ is a matrix, which is responsible for the rotation and scale factor between the projector image plane, and the camera's image plane, and $S_{ij} = \begin{bmatrix} e \\ f \end{bmatrix}$ is the transitional vector between the two coordinates.

Therefore by having the rotational and scaling matrix of T_{ij}^{cp} , as well as the transitional vector of S_{ij} , each pixel on the camera's image plane can be traced back to the corresponding pixel of the projector image plane, figure 3.2.

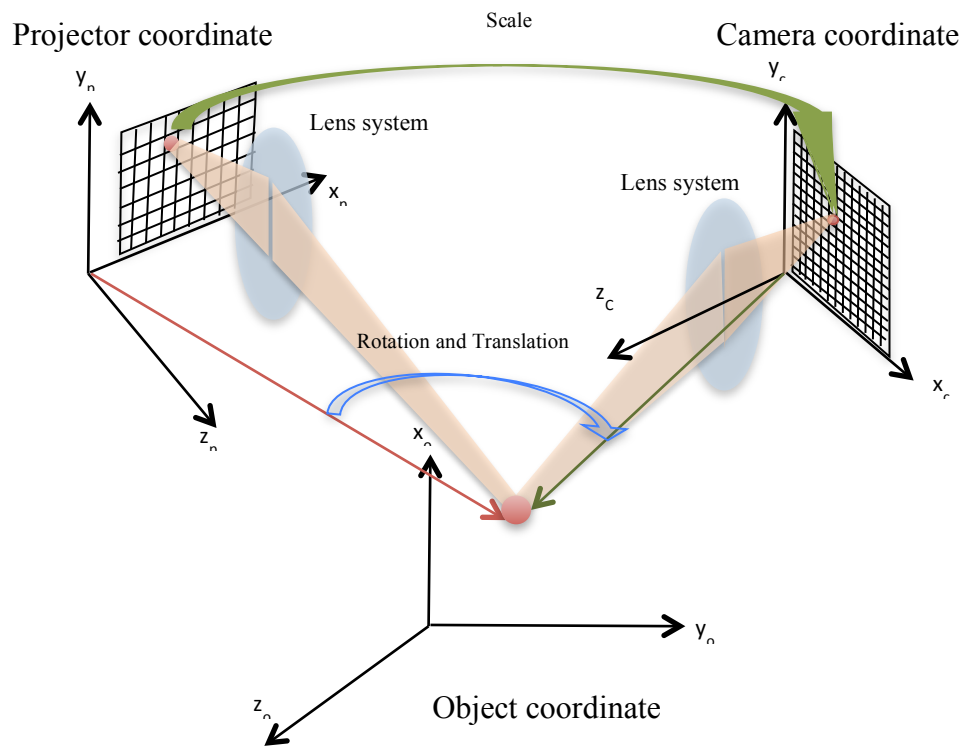


Figure 3.2 Linear geometrical alignment between the projector coordinate and camera.

In order to find $T_{ij}^{cp} = \begin{bmatrix} a & b \\ c & d \end{bmatrix}$, and $S_{ij} = \begin{bmatrix} e \\ f \end{bmatrix}$, we project three pre-defined points onto the object, and obtain their images on the camera. Therefore three relations can be written between the camera's three pixels and projector's three pixels based on equation 3.1 as follows:

$$\begin{bmatrix} x_{p1} \\ y_{p1} \end{bmatrix} = \begin{bmatrix} a & b \\ c & d \end{bmatrix} \begin{bmatrix} x_{c1} \\ y_{c1} \end{bmatrix} + \begin{bmatrix} e \\ f \end{bmatrix} \quad (3.2)$$

$$\begin{bmatrix} x_{p2} \\ y_{p2} \end{bmatrix} = \begin{bmatrix} a & b \\ c & d \end{bmatrix} \begin{bmatrix} x_{c2} \\ y_{c2} \end{bmatrix} + \begin{bmatrix} e \\ f \end{bmatrix}$$

$$\begin{bmatrix} x_{p3} \\ y_{p3} \end{bmatrix} = \begin{bmatrix} a & b \\ c & d \end{bmatrix} \begin{bmatrix} x_{c3} \\ y_{c3} \end{bmatrix} + \begin{bmatrix} e \\ f \end{bmatrix}$$

By simple calculations using the above equations, we can show that the unknown coefficient of a, b, c, d, e, and f can be found by solving the equations below:

$$\begin{bmatrix} a \\ b \\ c \end{bmatrix} = \begin{bmatrix} x_{c1} & y_{c1} & 1 \\ x_{c2} & y_{c2} & 1 \\ x_{c3} & y_{c3} & 1 \end{bmatrix}^{-1} \begin{bmatrix} x_{p1} \\ x_{p2} \\ x_{p3} \end{bmatrix} \quad (3.3)$$

And, (3.4)

$$\begin{bmatrix} d \\ e \\ f \end{bmatrix} = \begin{bmatrix} x_{c1} & y_{c1} & 1 \\ x_{c2} & y_{c2} & 1 \\ x_{c3} & y_{c3} & 1 \end{bmatrix}^{-1} \begin{bmatrix} y_{p1} \\ y_{p2} \\ y_{p3} \end{bmatrix}$$

As mentioned before, the above linear transformation function is only good sufficient when the object under the measurement is a uniform planer object, however, in our experiments, almost all the objects under the measurement are not planer, and they have complex geometries. Therefore, the assumption of the linear approximation, which states that the ratios of length and angle information are preserved between the projector and camera, is no longer valid over the entire image. One technique to find the geometrical alignment in a non-linear transformation is to divide the image into sub-regions where the

linear approximation is valid for each. Therefore for each sub-region we can use the three-point technique as explained above to find the rotational and scaling matrix of T_{ij}^{cp} , and the transitional vector of S_{ij} , and stitch the sub-regions together to find the general non-linear transformation matrix.

In our experiments, we usually projected a checkerboard pattern to the sample under measurement and the camera observed the reflection pattern. Corners on the checkerboard pattern were determined in the camera's image plane and the point correspondences between the camera and the projector were calculated considering the linear transformation at each square, figure 3.3. From this information the transformation matrix, T_{ij}^{cp} between the camera's and projector's pixels and the translation vector, S_{ij} , were computed.

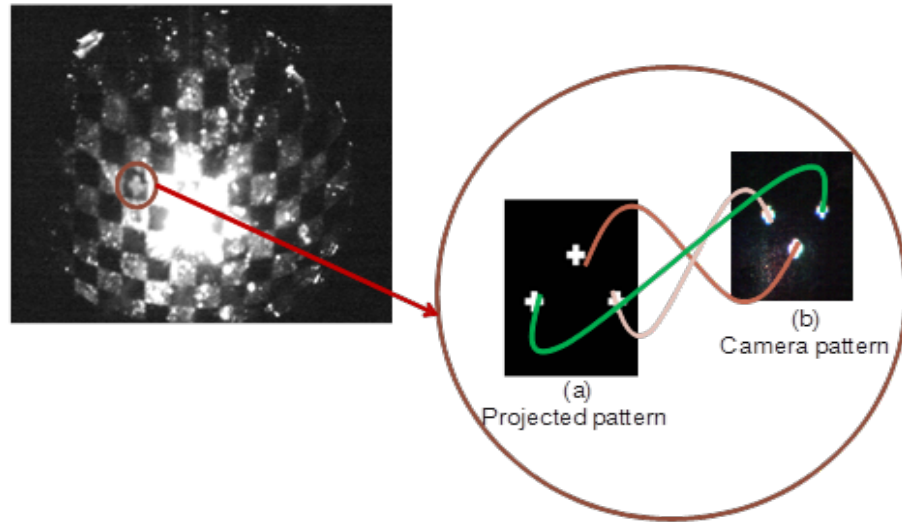


Figure 3.3: Geometrical alignment between camera pixels and projector pixels, a) projected pattern, and b) captured image by the camera.

Knowing the transformation function between the camera and projector, the SVPI technique then targets all the pixels on the projector, which correspond to the saturated or under-exposed pixels on the camera's plane, and modifies their intensities accordingly.

In order to quantify how effectively the reflected pattern preserves the correct intensity and phase information of the object, a dynamic range coefficient is introduced as below:

$$K_{DR} = \frac{N_p}{N_t - N_s} \quad (3.4)$$

where, N_p is the number of pixels with intensities within the dynamic range of the camera (for example for a 8 bit camera this value is between 0 to 255 gray scale level), N_t is the

total number of pixels in the camera image, and N_s is the number of pixels in which their intensity values cannot be altered due to some physical limitations in the system such as the lighting conditions, properties of the object under test, and the camera noise.

In order to find N_s , first a uniform white pattern (intensity level of 255) was projected to the sample, and the total number of pixels with intensities below the camera noise level was identified as N_s^D . These are all the pixels, which their intensity will always be below the camera noise no matter how many times the algorithm applies to the system. Then, a solid dark pattern (intensity level of 0) was projected to the sample, and the total number of pixels with intensities above the saturation level is identified as N_s^S . These are all the pixels, which their intensities will be always saturated no matter how many times the algorithm applies to the system. N_s is the sum of N_s^D and N_s^S .

A flowchart of the SVPI technique for 3D profilometry of object using a digital fringe projection system is shown in figure 3.4. The first step in the algorithm is to define some initial parameters as below:

" i " is the number of iteration in the algorithm.

" K_{DR}^0 " is a constant value of 0. This constant will be used in the first iteration of the algorithm only for comparison between the two successive dynamic range coefficients.

" M^0 " is the camera initial mask, which is a matrix with the same resolution as the image obtained by the camera, for example if the image of the camera has 1024×1024 pixels, M^0 is a 1024×1024 matrix, in which all of its elements are one.

" σ " is a pre-determined value, which depends on the lighting condition and camera noise level. This value will be used to compare the dynamic range coefficient of two successive images taken by the camera. In order to find σ , a uniform pattern was

projected on a flat glass wafer and its reflection recorded by the camera at different times. The six-sigma standard deviation in the intensity of the twenty images is shown as σ in the flowchart. The standard deviation, σ , was calculated using the following equation:

$$\sigma = \sqrt{\frac{1}{N} \sum_{i=1}^N (x_i - \mu)^2} \quad (3.5)$$

where, N is the number of images, and μ is the mean intensity value of all the obtained images.

Given these initial values, the algorithm creates a structured pattern, which will be projected onto the object using the projection unit and the imaging unit captures the reflected pattern from the object. P^i and R^i are the structured patterns projected to the object and its reflected pattern obtained by the imaging unit at i^{th} iteration of the algorithm; respectively.

Then for each obtained image from the camera, the algorithm calculates the dynamic range coefficient, K_{DR}^i , and compares it with the dynamic range coefficient of the previously captured image by subtracting them from each other. If the difference between the two successive dynamic range coefficients is greater than the pre-determined σ value, the algorithm can improve the dynamic range of the system by taking the following steps:

1. The algorithm finds all the saturated and all the under exposed pixels in the image obtained by the camera.

2. Then a camera mask with the same size as the image obtained by the camera will be created, in which all of its pixels corresponding to the saturated pixels on the camera have the value of $\frac{1}{K}$ and all of its pixels corresponding to the underexposed pixels on the camera have the value of k , and the rest are all equal to one.
3. Based on the created camera mask and considering the geometrical alignment, a projector mask will be created with the same resolution as the projector.
4. The projector mask will be multiplied by the previously projected pattern to create a new modified structured pattern.
5. The new pattern will be projected to the object and the camera will obtain the reflected pattern.
6. Finally, the dynamic range of the previously obtained image will be compared by the dynamic range coefficient of the latest obtained image.

The algorithm stops when the difference between two successive dynamic range coefficients is less than the pre-determined value " σ ". At this point we have reached the limit of the system and the dynamic range of the system cannot be improved any further due to the presence of noise and physical limitations in the system.

We can retrieve the true intensity value of the light reflecting off of the object toward the camera by scalar multiplication of the intensity values of the final image obtained by the camera, with the reverse values of all the applied camera masks, equation 3.5.

$$\text{HDR_Image} = R^f \times \frac{1}{\prod_{i=1}^n \text{mask}(\#i)} \quad (3.5)$$

Where " R^f " is the final image recorded by the camera and " n " is the number of camera masks, which have been applied. By having the HDR image, the phase map of the pattern using one of the fringe analysis techniques, such as Fourier transform [90] or four-step phase shifting can be computed [95].

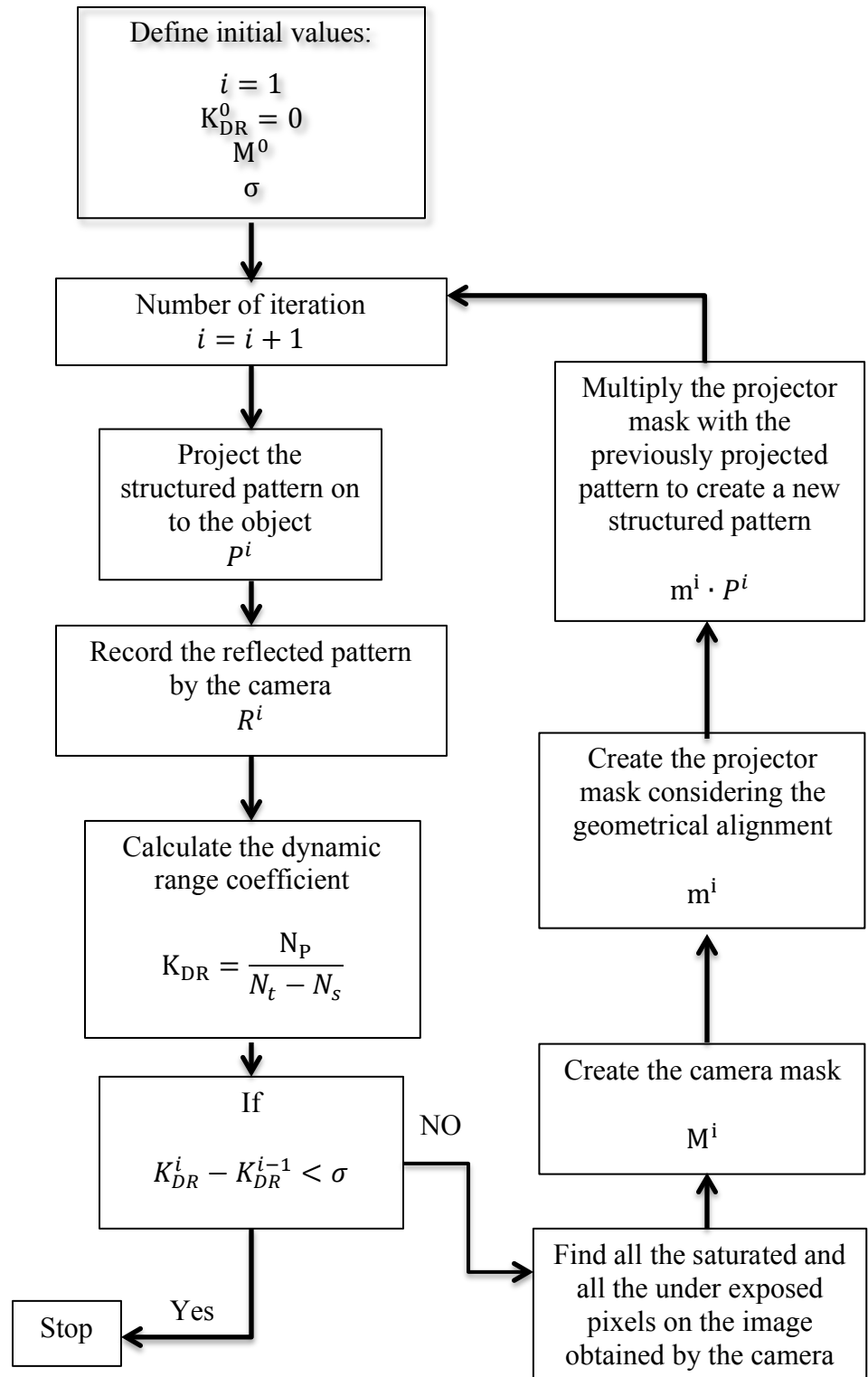


Figure 3.4: SVPI technique flowchart to enhance dynamic range in a fringe projection.

3.3. Simulation

The SPVI technique is simulated in Matlab. A sinusoidal pattern illuminates a hemispherical object with known height and reflectivity, and the reflected pattern is recorded by a 10 bit simulated camera at a different angle as shown in Figure 3.5.

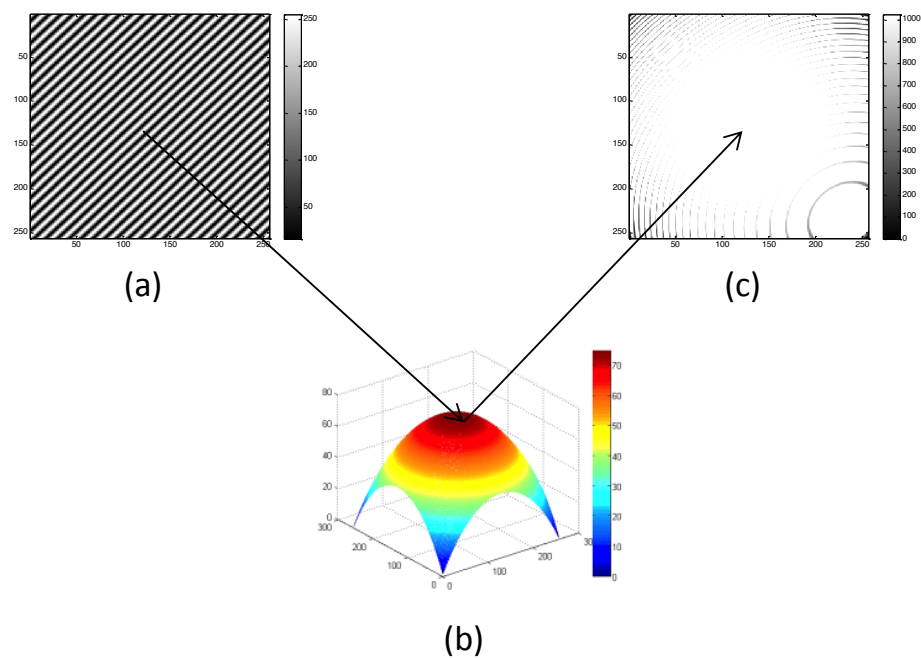


Figure 3.5: (a) Initial simulated structured pattern, (b) the simulated object, and (c) the initial reflected pattern.

The dynamic range coefficient for the reflected pattern shown in figure 3.5 (c) is 0.07. Almost all of the pixels' values are saturated. We applied SVPI technique to this reflected pattern. The dynamic range coefficient of the reflected pattern after applying the SVPI one time is 0.35, which shows five-fold improvement from 0.07. We repeated the SVPI

technique once more and the dynamic range coefficient was improved to 0.95. The constructed intensity masks, the modified structured pattern, and the images obtained by the camera after each step of applying the SVPI are shown in figure 3.6.

Figure 3.7 shows the HDR constructed image using equation 3.5, and its unwrapped phase map obtained by the Fourier transform technique [90].

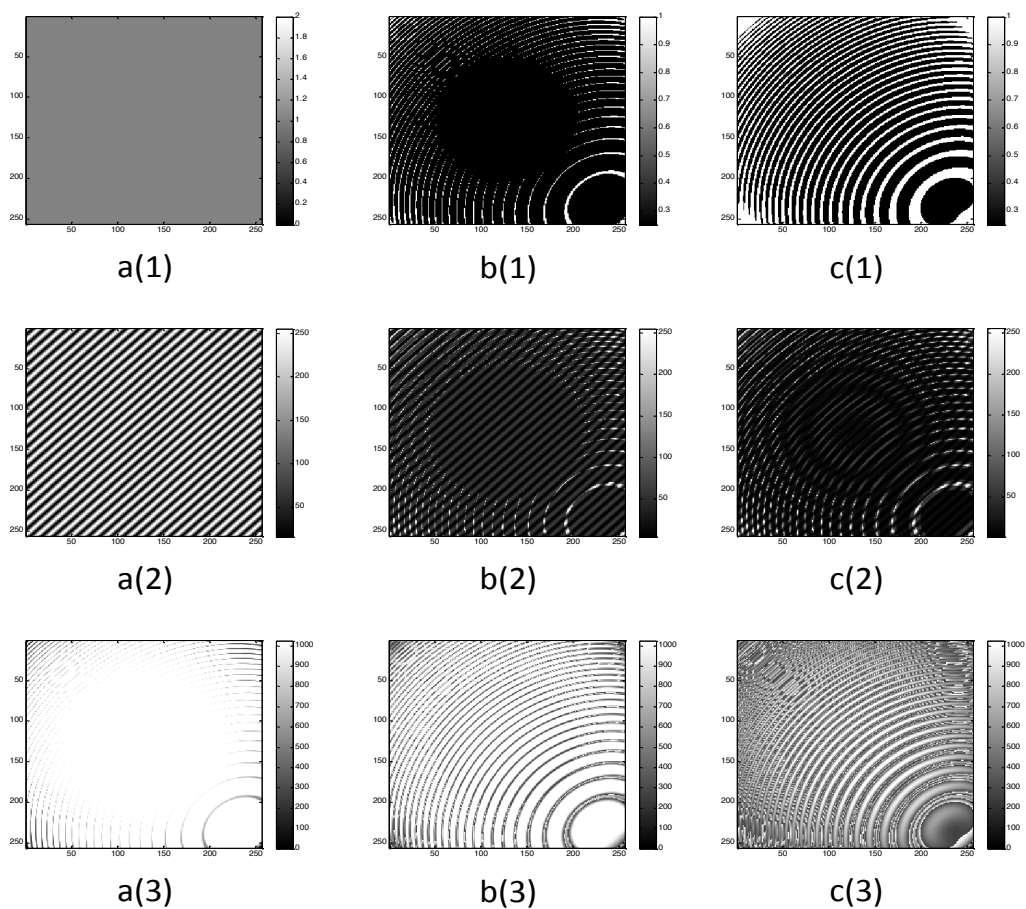


Figure 3.6: Simulation results for the DR enhancement using SVPI technique, a) intensity mask, a(1), structured pattern, a(2) and the reflected pattern, a(3), before applying the SVPI, $K_{DR} = 0.07$, b) intensity mask, b(1), structured pattern, b(2), and the reflected pattern, b(3) after applying the SVPI once, $K_{DR} = 0.35$, c) intensity mask, c(1), structured pattern, c(2) and the reflected pattern, c(3) after applying the SVPI twice, $K_{DR} = 0.95$.

The actual reflectivity level from the object to the camera is between 0 - $1.9072e+004$ gray scale levels. Simulation results show that with SVPI technique we can improve the dynamic range of the fringe projection system by more than four bits.

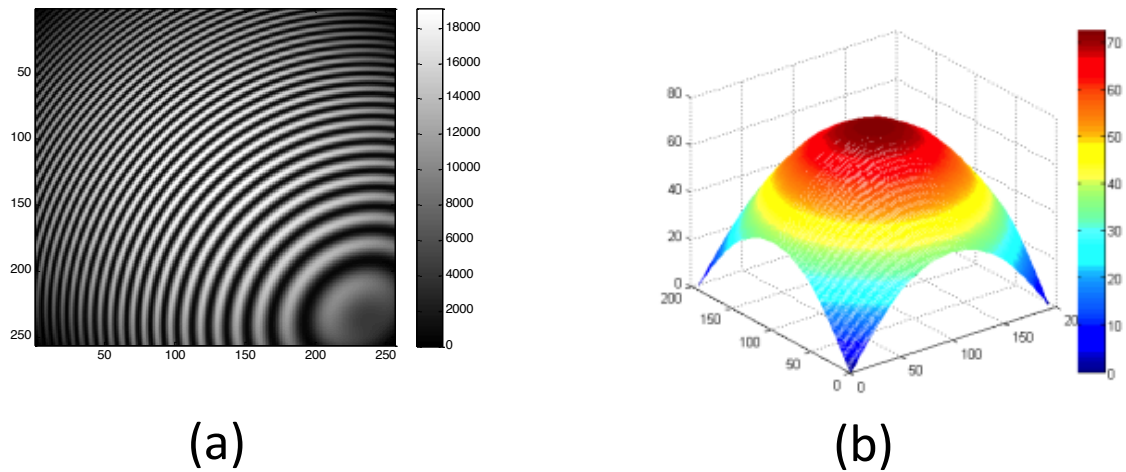


Figure 3.7: (a) HDR constructed image using the SVPI technique, and (b) the phase map of the object using the DCFT technique

In the rest of this chapter we will describe several digital fringe projection systems to measure the 3D profile of freeform surfaces with different dimensions. All the objects under study exhibit high level of reflectivity towards the camera due to their shapes and material composition. We applied the SVPI technique to enhance dynamic range in these systems and the results will be presented.

3.4. Three Dimensional Profile Measurement of a Calibration Sphere

A Calibration sphere, or a datum sphere is a specular metallic ball, which is widely used in calibration of coordinate measuring machines (CMM). In order to evaluate and determine compensation needed for errors in CMM, it is essential to correctly measure the 3D profile of these objects. However, due to their spherical shape, they reflect light at wide range of angles from normal to near horizontal. Therefore, collecting the true intensity value from such objects using a conventional, low dynamic range camera is a challenge. In this experiment we have applied the SVPI in a digital fringe projection setup to characterize a calibration sphere. The schematic of the experimental setup used is shown in figure 3.8. A pattern, generated by MATLAB code, was projected on the sample at an angle using an AAXA M2 micro projector, native XVGA with 1024x768 resolutions. The projected pattern illuminates the sample with an angle. The reflected pattern was captured by an AVT P Guppy F-146 camera with 1392 x 1024 pixels along a perpendicular line. Field of view of the system is $5.2\text{ mm} \times 5.2\text{ mm}$, and its lateral resolution is $5\ \mu\text{m}$.

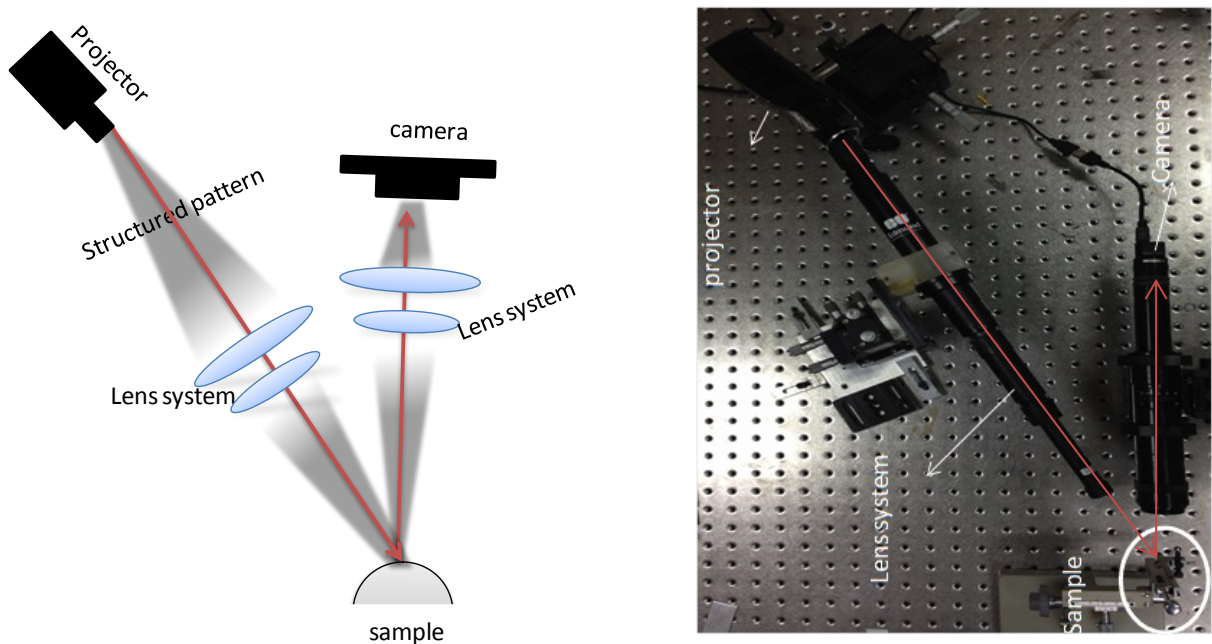


Figure 3.8: Schematic of a system implemented to demonstrate dynamic range enhancement in digital fringe projection for 3D profile measurement of a calibration ball.

A geometrical alignment procedure as described before was used and transformation matrix between camera's image plane and the projector's image plane, T_{ij}^{CP} , and the translation vector of S_{ij} , were calculated. The camera exposure time was set for 500 ms. Figure 3.9 shows the result of SVPI technique after applying the technique once. The dynamic range coefficient of the first image obtained by the camera is 0.79 ± 0.03 , after applying the SVPI technique once the dynamic range coefficient is increased to 0.89 ± 0.03 .

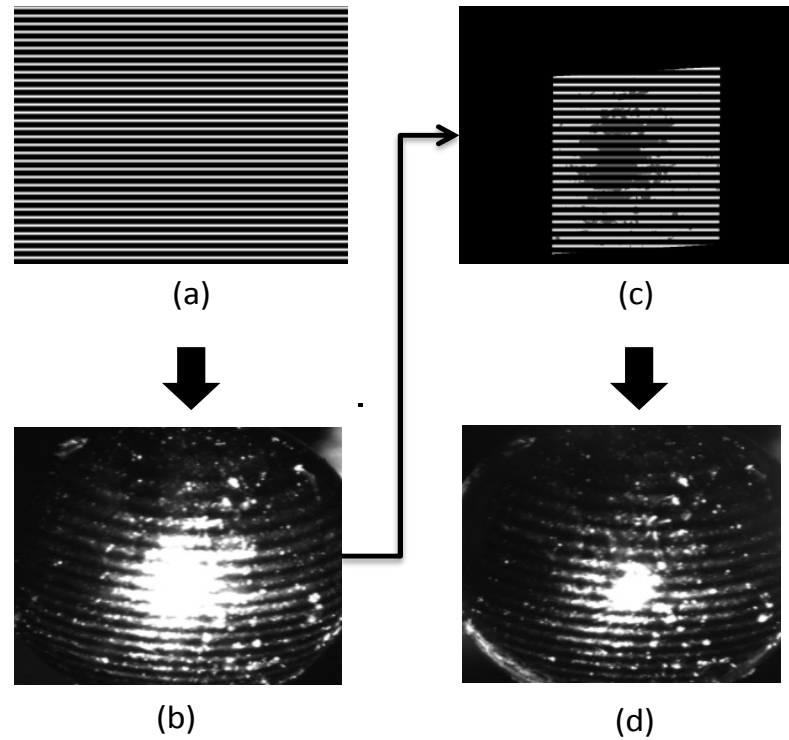


Figure 3.9: (a) First structured pattern projected onto the sample without applying the SVPI, (b) first reflected image captured by the camera, (c) modified structured pattern based on SVPI technique, and (d) reflected pattern recorded by the camera after applying the SVPI once.

The SVPI technique is applied for the second and third time. The dynamics range coefficient difference of the third and fourth reflected patterns is less than the predetermined value of $\sigma = 0.03$, therefore the SVPI algorithm is terminated after applying the technique three times. Figure 3.10 shows the structured projection patterns and their corresponding reflected images for the metallic ball before applying the SVPI technique, 3.10-a (1) and 3.10-a (2), and after applying the SVPI technique for the first, 3.10-b (1), 3.10-b (2), and second time, 3.10-c (1), 3.10-c (2). The dynamics range coefficient of the final captured image is 0.99 ± 0.03 .

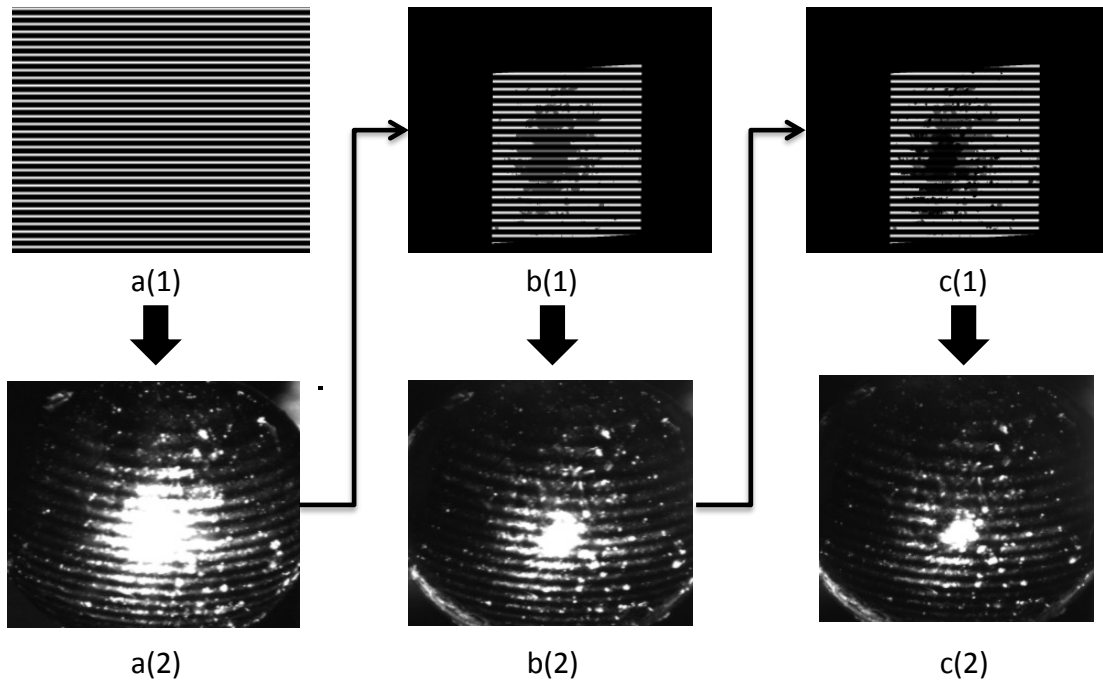


Figure 3.10: a (1) Initial structured pattern illuminating the sample, a (2) first reflected image captured by the camera, $K_{DR} = 0.79 \pm 0.03$, b(1) modified structured pattern after applying the SVPI once, b(2) reflected image using the modified pattern b(1), $K_{DR} = 0.89 \pm 0.03$, c(1) modified structured pattern after applying the SVPI twice times, and c(2) reflected image using the modified pattern c(1), $K_{DR} = 0.99 \pm 0.03$.

In order to calculate the phase map of the final HDR image, a four-step phase shifting algorithm [95] was used and consequently unwrapped using the quality-guided [94] algorithm. Figure 3.11 shows the wrapped phase of the calibration sphere and its unwrapped phase.

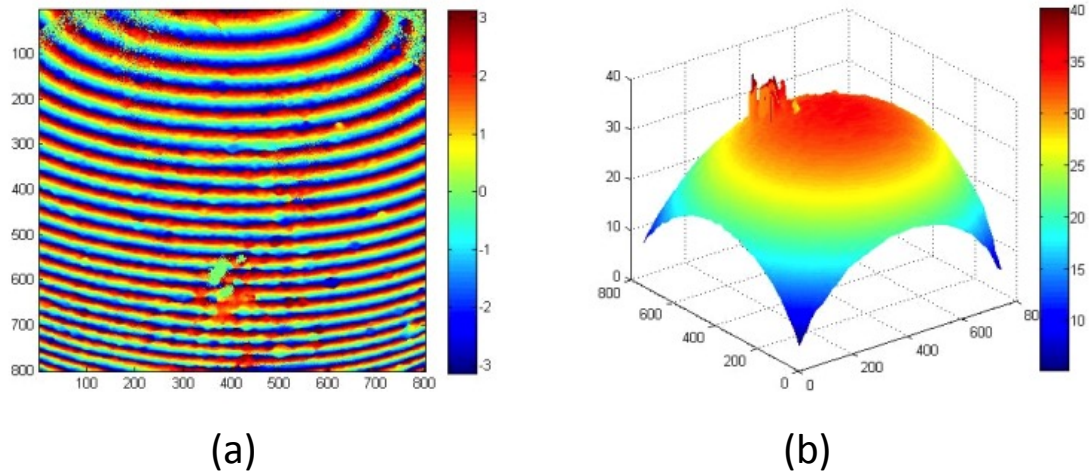
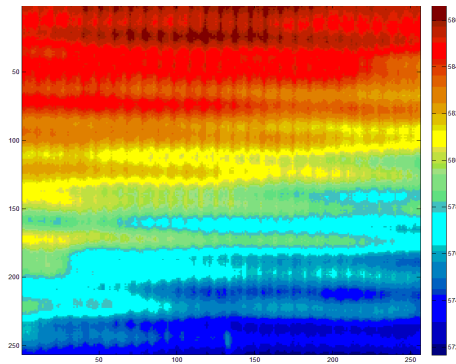


Figure 3.11: (a) Phase of the metallic ball calculated by 4-step phase shifting, and (b) unwrapped phase map of the sample

In order to translate the phase information into the height information we determined the equivalent wavelength of the system. The mathematical description of the equivalent wavelength in fringe projection technique was discussed in chapter 2. In general, the equivalent wavelength depends on the pitch of the fringe pattern and the system configuration. To measure the equivalent wavelength experimentally, we used a flat surface as the object and changed the distance of the object incrementally along the optical axis. For each incremental change we acquired the fringe pattern. As the object moves, the fringe patterns also moves. By looking at one pixel, we observed that the change of the intensity follows a sinusoidal function. The amount of movement that corresponds to the period of this sinusoidal function is the equivalent wavelength for that pixel. The equivalent wavelength can vary from one pixel to another pixel due to parameters such as the angle between the projector and the camera, and the quality of the

optical components such as lens systems used in the setup. Figure 3.12 shows the equivalent wavelength map for the fringe projection setup used for 3D profilometry of the calibration ball.



3.12: Equivalent wavelength map for the fringe projection setup used for 3D profilometry of the calibration ball.

Figure 3.13 shows the actual height map of the calibration ball using the equivalent wavelength map for each pixel.

To characterize the system, an uncertainty analysis was performed on the system based on the following procedure.

We acquired the height map of the object by acquiring phase-shifted interferograms and using the described fringe analysis technique. This procedure repeated ten times by removing the object and putting it back in its place and measuring the object's surface profile each time.

The standard deviation of difference between the measurements were calculated using equation 3.5. Then the standard deviation is multiplied by six to obtain the error at 99.6%.

The average height of the semi-spherical ball calculated from the tens measurement was determined to be 2.237 mm , and the uncertainty of the system was determined to be 0.018 mm . Therefore the final measurement result for the height of calibration ball is $2.237 \text{ mm} \pm 0.018 \text{ mm}$ with 99.6% of confidence level.

The diameter of the calibration ball was calculated based on multiplying the total number of pixels, which lies within one end of the calculated height map to the other end of the height map (from point A to B in figure 3.13) and the dimensions of each pixel of the camera (lateral resolution of the system). The camera has 1024×1024 pixels, with the field of view of $5.2 \text{ mm} \times 5.2 \text{ mm}$, therefore the lateral resolution of the system is $r_2 = 5.2 \text{ mm} / 1024 = 0.005 \text{ mm}$. As the result the diameter of the calibration ball was calculated to be 4.784 ± 0.005 .

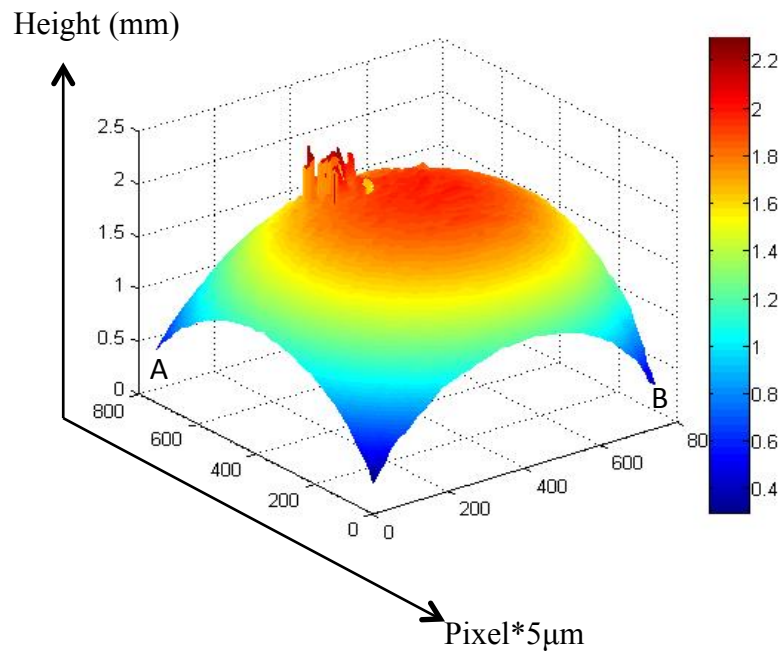


Figure 3.13: Actual height map of the calibration ball using the SVPI technique in a digital fringe projection system.

3.5. Three Dimensional Profile Measurements of Solder Bumps

One challenge in advanced integrated circuit packaging is to measure the profile of solder bumps in the flip chip bonds. Solder bumps are partial-spherical microstructures, which function as high-density interconnectors in flip chip technology. Due to the spherical shape and high reflectivity of solder bumps, acquiring a 3D profile of such structures based on a fringe projection technique requires a HDR imaging system. The spherical shape of the bumps, with large slopes on the sides, makes light collection from the sides very difficult while high reflectivity from the top of the bumps saturates some camera pixels, figure 3.14.

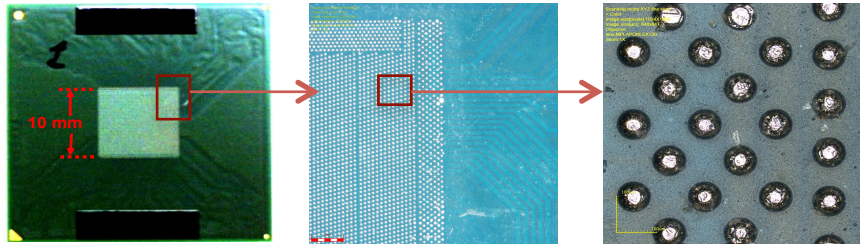


Figure 3.14: Solder bump field on the middle of a substrate package at different magnification.

In order to enhance the dynamic range and measure 3D profile of solder bumps using a digital fringe projection system, an experimental setup was developed as shown in figure 3.15. A structured pattern, generated by Matlab code, was projected on the sample using a micro projector (model: 3M, MPro150) with 1024x768 resolution. The projected pattern goes through a lens system using a binocular stereomicroscope (model: Leica MS5) with a 2x external de-magnifying lens and illuminates the object at an angle. The reflected image was taken by a SUMIX camera with a resolution of 2048×1536 using the other arm of the stereomicroscope. The field of view of the system at its highest magnification was $1.2 \text{ mm} \times 0.9 \text{ mm}$, and its lateral resolution was $1 \mu\text{m}$.

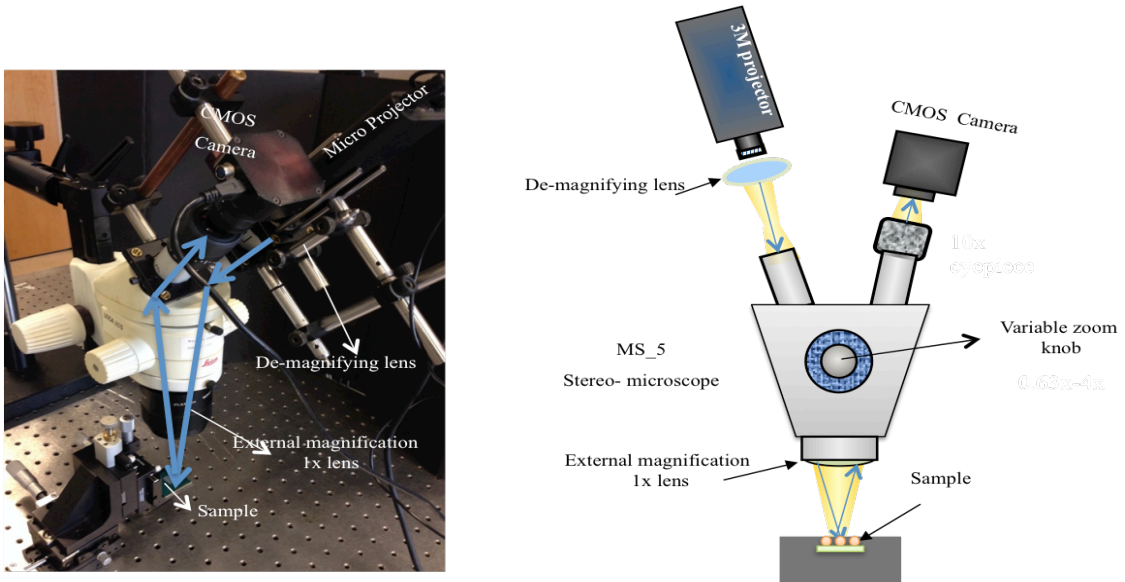


Figure 3.15: Schematic of the experimental setup of dynamic range enhancement in fringe projection using SVPI technique.

Figure 3.16 shows a solder bump field with the projected fringes as seen by the experimental setup at the highest zoom level of the system.

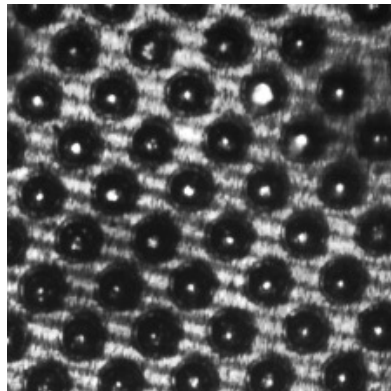


Figure 3.16: The reflected pattern captured by the SVPI system with an exposure time = 16.56 ms.

The dynamic range coefficient of the above image is 0.57 ± 0.03 . We have applied the SVPI process twice to improve the dynamic range of the system. Figure 3.17 shows the modified patterns and corresponding reflected patterns before and after the SVPI technique is applied once and twice. The dynamic range coefficient of the final image, figure 3.17 (f), is 0.98 ± 0.03 .

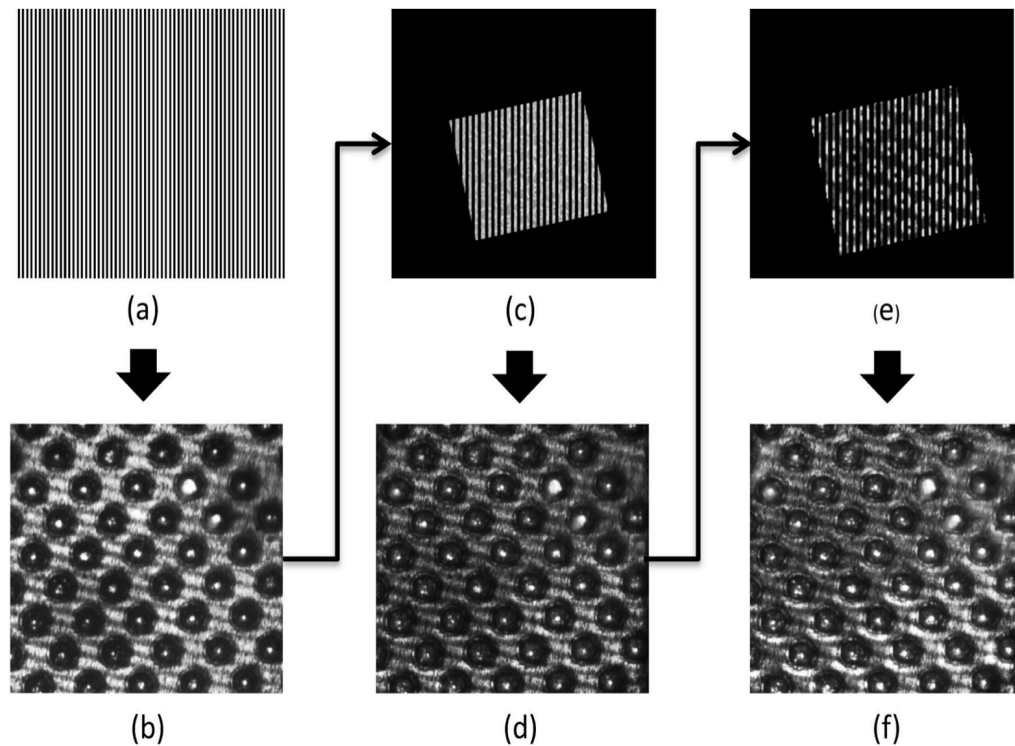


Figure 3.17: (a) Initial structured pattern illuminated to the solder bumps, (b) first reflected pattern captured by the camera, $K_{DR} = 0.57 \pm 0.03$, (c) first modified structured pattern after applying the SVPI technique once, (d) second captured pattern, $K_{DR} = 0.89 \pm 0.03$, (e) second modified structured pattern after applying the SVPI technique twice, and (f) third reflected pattern, $K_{DR} = 0.98 \pm 0.03$.

A 4-step phase shifting algorithm [95] was then used to calculate the phase of the image, figure 3.18 (a). In order to eliminate the carrier frequency, a 2D Fourier transform applied to the obtained phase and a median Gaussian filter run through the detected signal, figure 3.18 (b). Then the filtered signal was shifted to the center in order to eliminate the effect of carrier frequency in the phase map, figure 3.18 (c). Finally, the phase map of the object without the presence of carrier frequency was obtained by applying a 2D inverse Fourier transform on the filtered and centered Fourier spectrum of the phase, figure 3.18 (d).

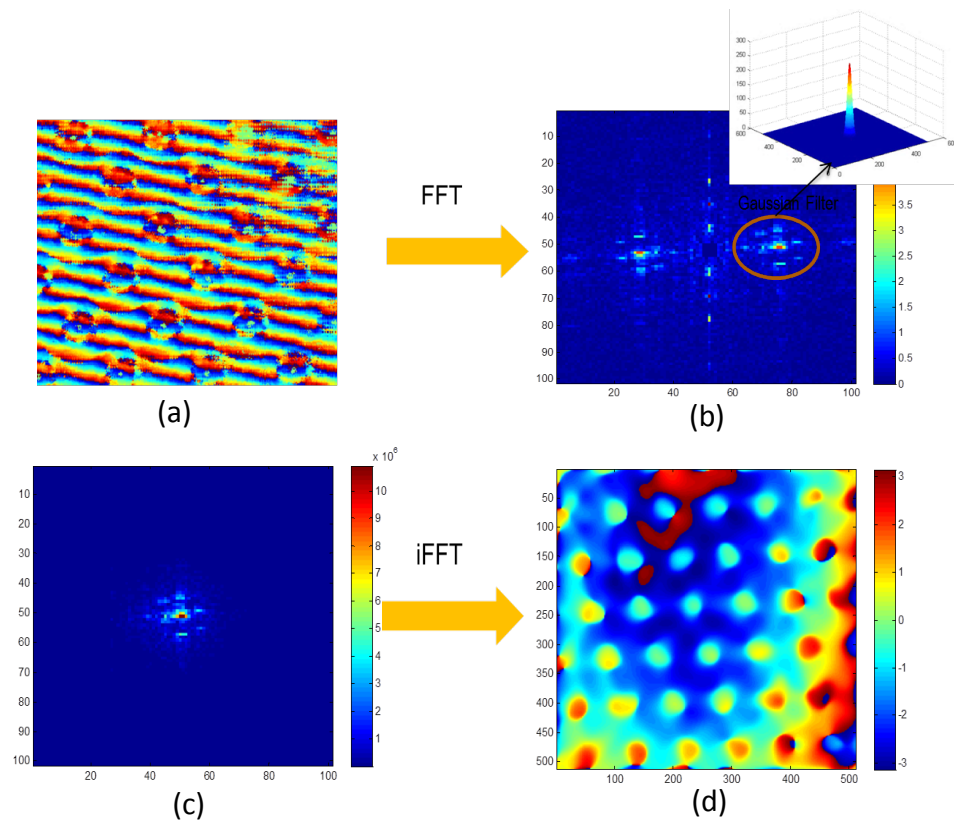


Figure 3.18: a) Combined carrier phase and object phase map obtained from the four-step phase shift fringe analysis technique, (b) Fourier spectrum of the combined phase map, (c) filtered and shifted to center phase spectrum, and (d) wrapped phase of the object without the carrier phase information.

Then a quality-guided algorithm [94] was applied to the underlying phase of the object, in order to find the continuous phase map of the object. Figure 3.19 shows the unwrapped phase map of the solder bumps.

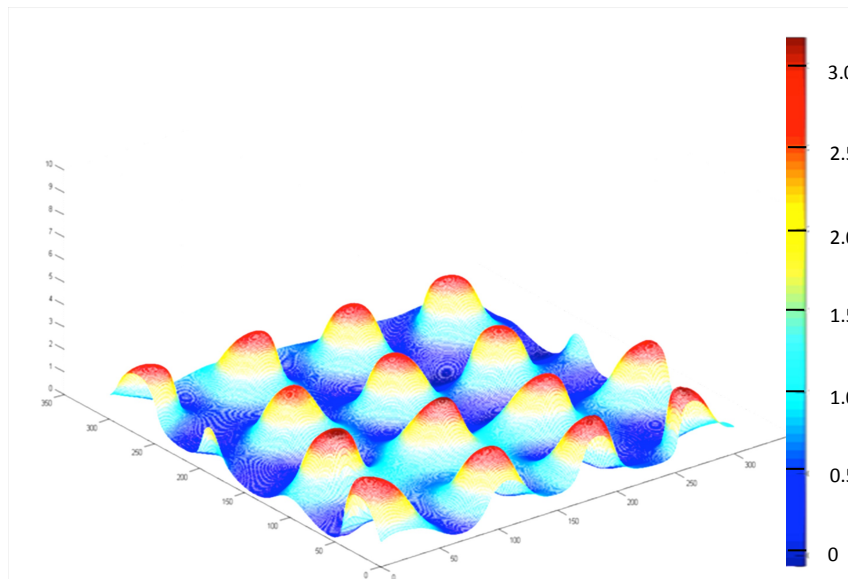


Figure 3.19: Three dimensional unwrapped phase of the solder bumps using SVPI technique in a digital fringe projection setup.

Since, in the process of the phase analysis to obtain the profile of the solder bumps, we have used a Gaussian filter, we have eliminated the noise components as well as some high frequency components associated with sharp edges. In order to estimate the boundaries, each bump has been fitted to a hemisphere and a code was generated to stitch the data from the 3D profile of a bump to its fitted hemisphere. The schematic of the process applied on one solder bump in order to find its final profile with sharp edges is shown in figure 3.20.

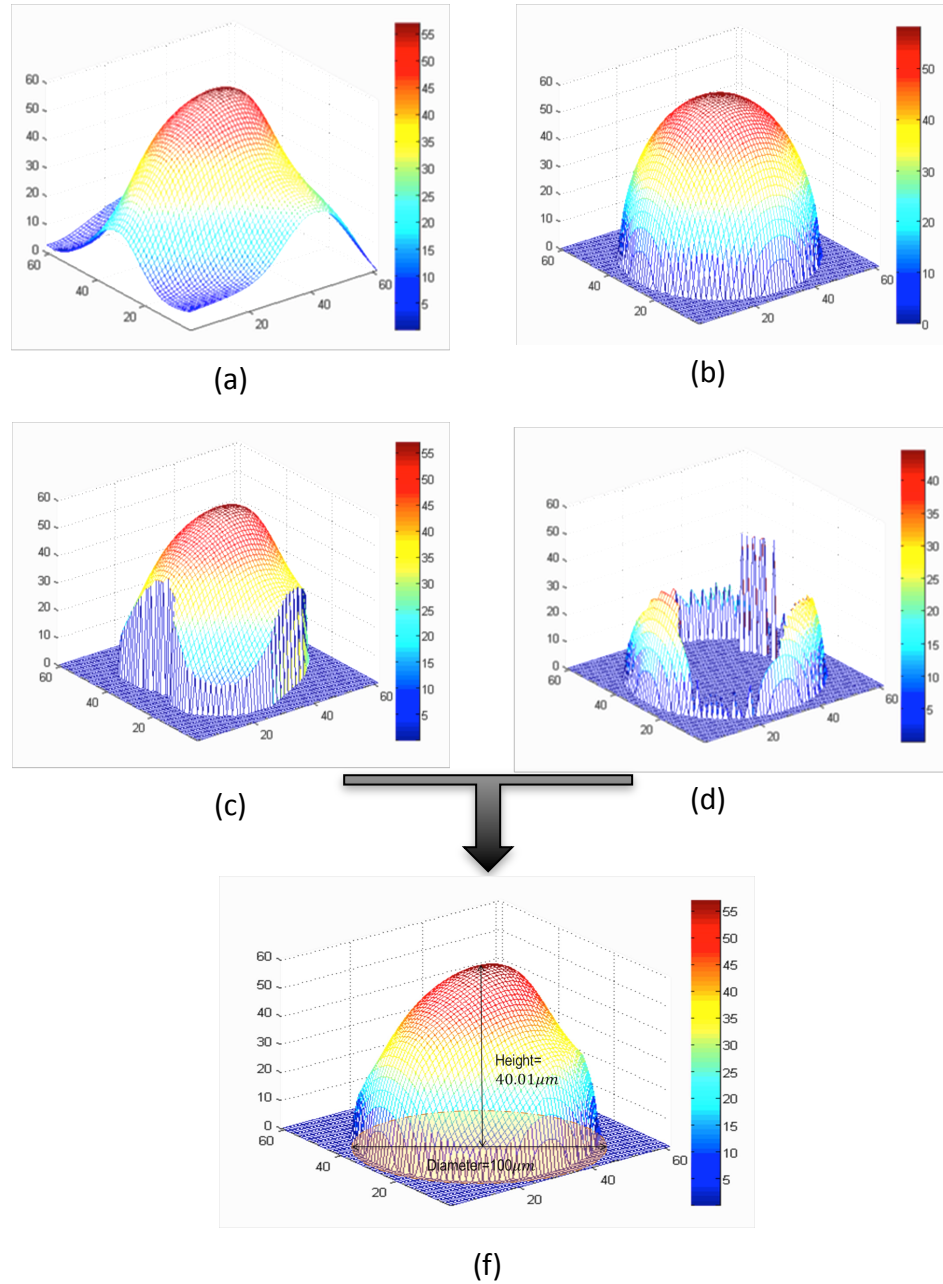


Figure 3.20: (a) 3D profile of one solder bump calculated from the SVPI technique, (b) hemisphere fit, (c) data selected from the raw profile of the solder bump, (d) selected data from the hemisphere fit, and (e) final profile of the solder bump with sharp edges.

The fitting process can be applied to all the solder bumps. Figure 3.21 shows the result of fitting to 9 different bumps. Since the solder bumps are located on a solder resist, the actual height of the bumps above the solder resist is less than what we measure from the fitting process. In order to find the average thickness of the solder resist, the local minimum of each bump before the fitting process was obtained. The average value of the local minima was considered as the average thickness of the solder resist. In our experiment this value was determined to be $10\ \mu\text{m}$. Figure 3.22 shows the profile of the solder bumps above the solder resist.

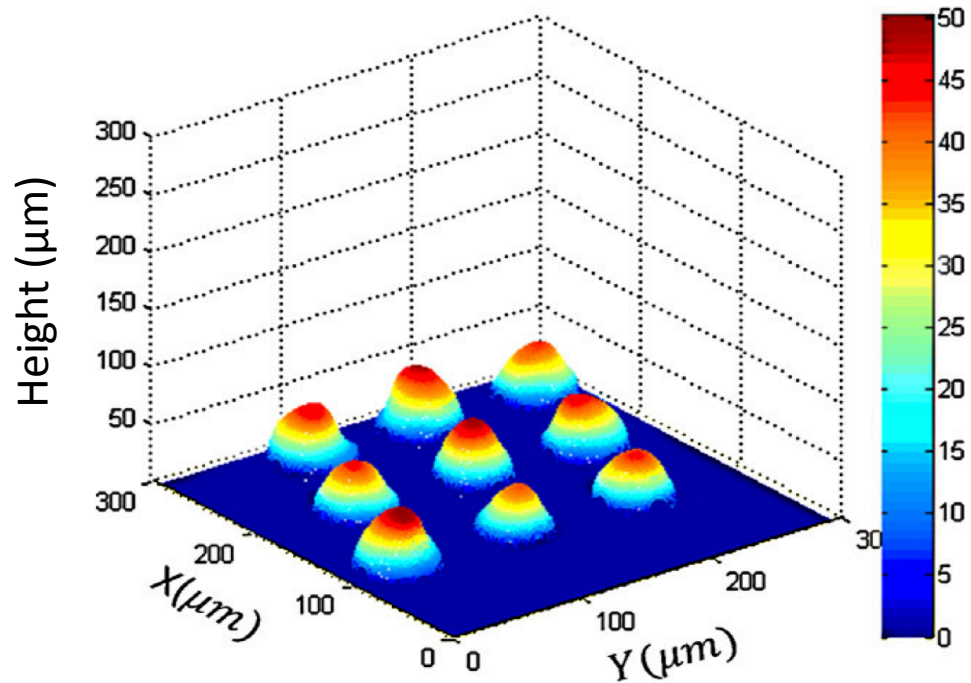


Figure 3.21: Three-dimensional profile of 9 solders bumps with sharp edges using the fitting process.

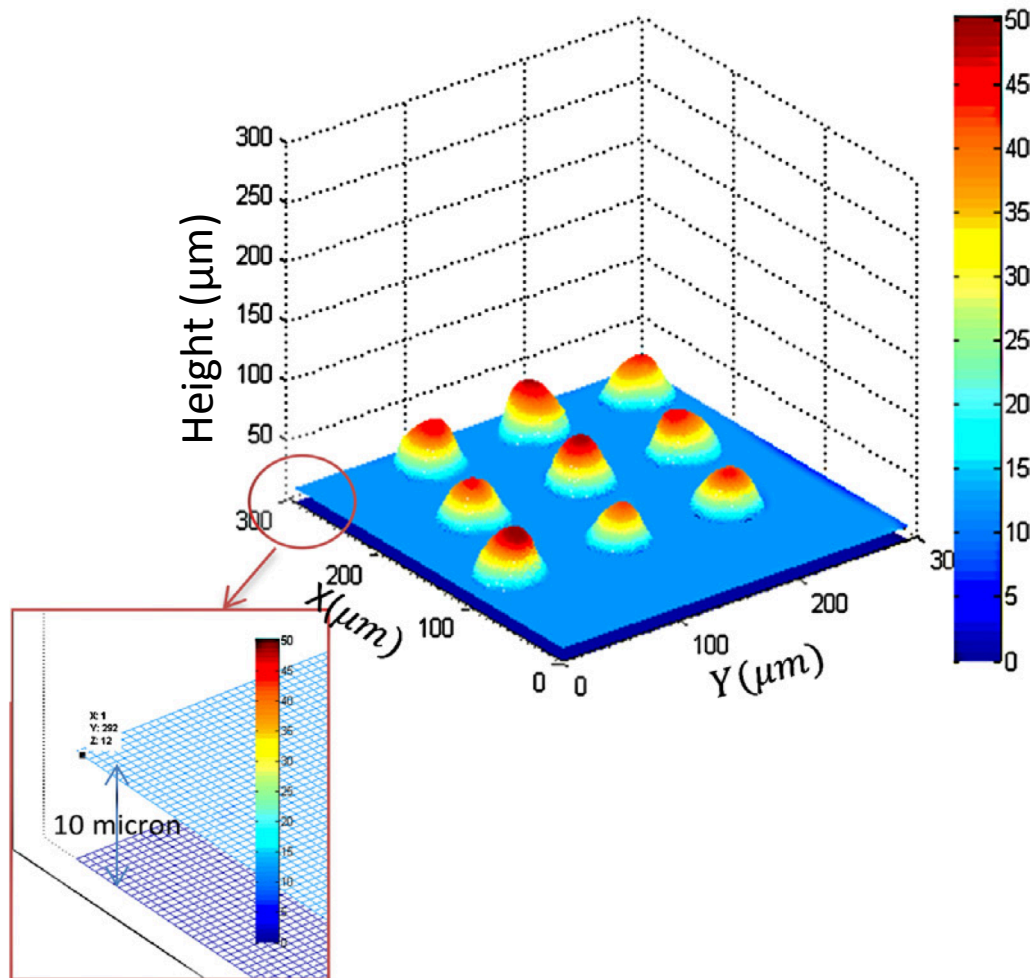


Figure 3.22: Three-dimensional profile of 9 solders bumps with sharp edges using the fitting process above the solder resist layer.

The height bumps were calculated after calculating the effective wavelength for the system, in the same manner as in section 3.4. The heights of the bumps were determined to be within the range of $33.63 \mu\text{m}$ to $40.09 \mu\text{m}$ while their radii varied between $47 \mu\text{m}$ to $51 \mu\text{m}$.

3.6. Three Dimensional Profile Measurements of Large Industrial Objects with Steep Slopes using Digital Fringe Projection

Fast and accurate 3D profile measurement of large objects is another important application of SVPI technique. The manufacturing industry needs a fast inspection process to control the quality of parts and determine if a feature is within tolerance specifications or not. Traditional 3D measurement techniques such as Coordinate Measurement Machines (CMM) and laser scanning provide accurate measurement. However, these techniques are generally slow and expensive. Digital fringe projection is a non-contact, fast, and low-cost alternative technique to measure the 3D profile of industrial parts. However, limitation of their dynamic range introduces challenges in accurate shape measurement of an object with wide variation in its optical reflectivity. One example of such an object is a metallic hemispherical object with a hollow sphere inside. Figure 3.23 shows the sample we used for this experiment.

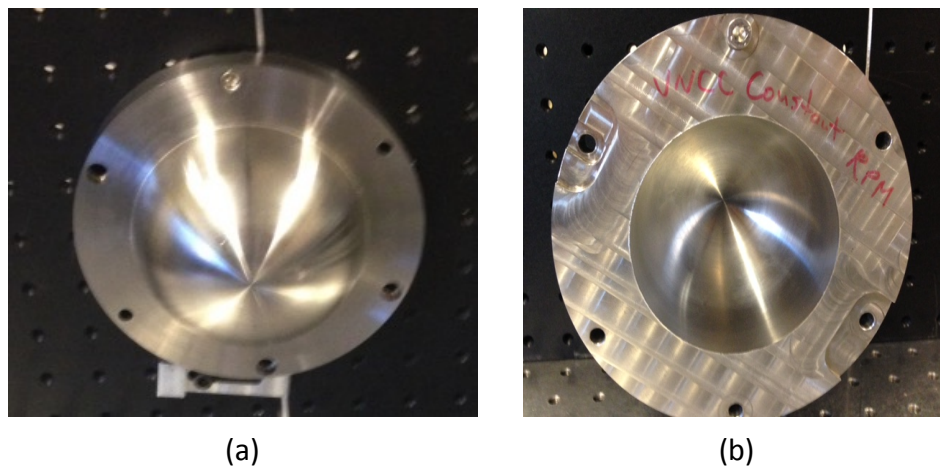


Figure 3.23: (a) The outer surface of a hemispherical shaped industrial object, and (b) the inner surface of a hemispherical shaped industrial object.

The goal is to measure both outside and inside surfaces of this object. However, the level of reflection towards the camera is more than the dynamic range of an 8 bit imaging system due to the spherical shape of the object. Therefore, we applied SVPI technique to enhance dynamic range in a digital fringe projection setup.

A schematic of a digital fringe projection setup used for 3D profilometry of the mentioned object is shown in figure 3.24. A sinusoidal pattern, generated by MATLAB code, was projected on the sample at an angle using a micro projector (model: 3M, MPro150) with 1024x768 resolution. The field of view of the system is $12.78\text{ cm} \times 16.45\text{ cm}$ and the lateral resolution is 0.16 mm .

Figure 3.25 shows images taken by the camera with different exposure times.

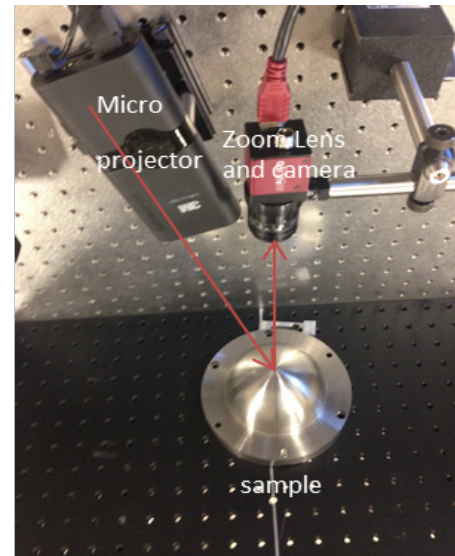
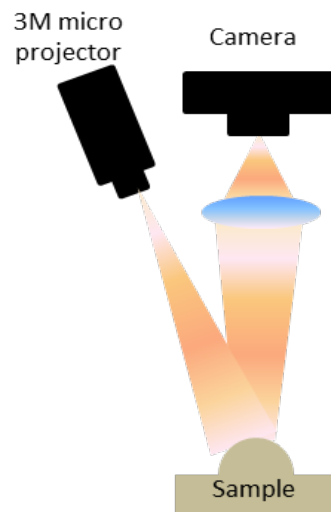


Figure 3.24: Digital fringe projection profilometry setup used for industrial spherical object profile measurement.

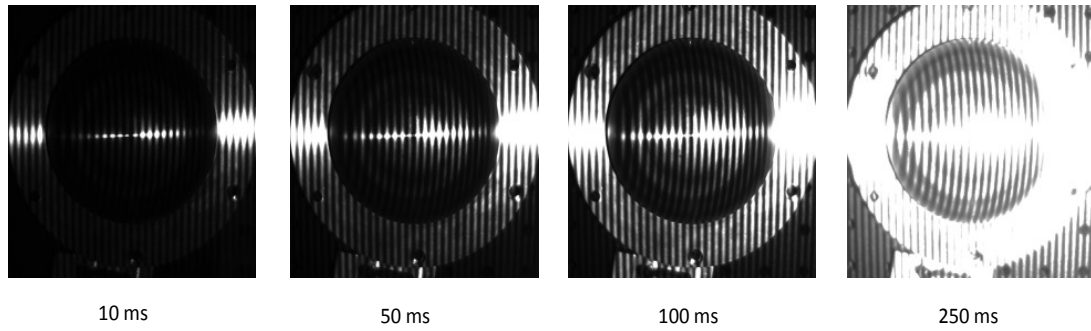


Figure 3.25: Images taken by the camera with different exposure times from the industrial spherical object.

In order to apply the SVPI technique, a piecewise linear geometrical alignment as discussed in section 3.2 was implemented, and the transformation matrix, T_{ij}^{CP} , and the translation vector, S_{ij} , were calculated, figure 3.26.

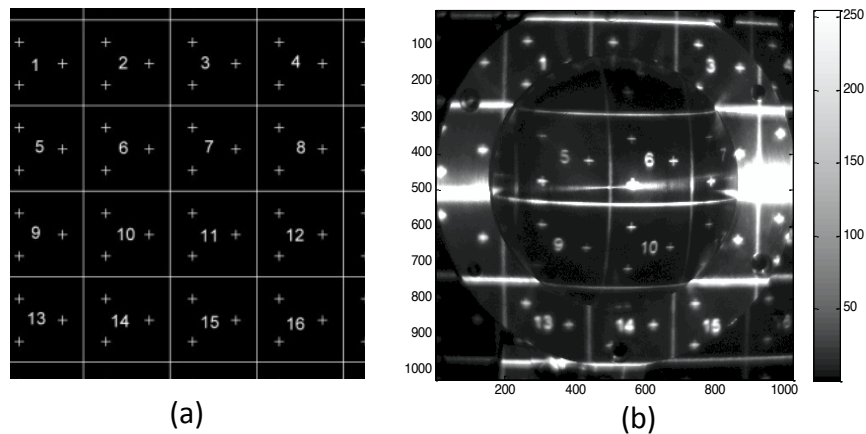


Figure 3.26: Piecewise linear geometrical alignment process between the projector plane and the camera image plane, (a) projector pattern with several segment with known three points, and (b) image obtained from the object illuminated by a known projected pattern.

After the geometrical alignment was implemented, the exposure time of the camera was set at 250 ms, and the SVPI technique was applied to enhance dynamic range of the digital fringe projection technique. Figure 3.27 (a) shows the obtained image by the camera from the outer surface of the object at 250 ms exposure. The dynamic range coefficient of this pattern is $K_{DR} = 51.33 \pm 0.02$, therefore more than half of the information from the object is lost as the result of low dynamic range of the system. Figure 3.27 (b) is the camera mask created by the algorithm in which the pixels corresponding to the saturated pixels on the image 3.27 (a) have lower values, and pixels corresponding to the under-exposed pixels on the image 3.27 (a) have higher values. Image 3.27 (c) is the created projector mask considering the geometrical alignment between the camera and the projector. Figure 3.27 (d) shows the new modified structured pattern by multiplying the projector mask to the initial sinusoidal fringe pattern. Finally, figure 3.27 (e) shows the second image obtained by the camera from the object when it is illuminated by the modified structured pattern. The dynamic range coefficient of this pattern is increased to $K_{DR} = 91.06 \pm 0.02$.

Therefore, by applying the SVPI technique we have been able to bring the intensity of more pixels within the dynamic range of the imaging system, and consequently preserve more phase information from the test object.

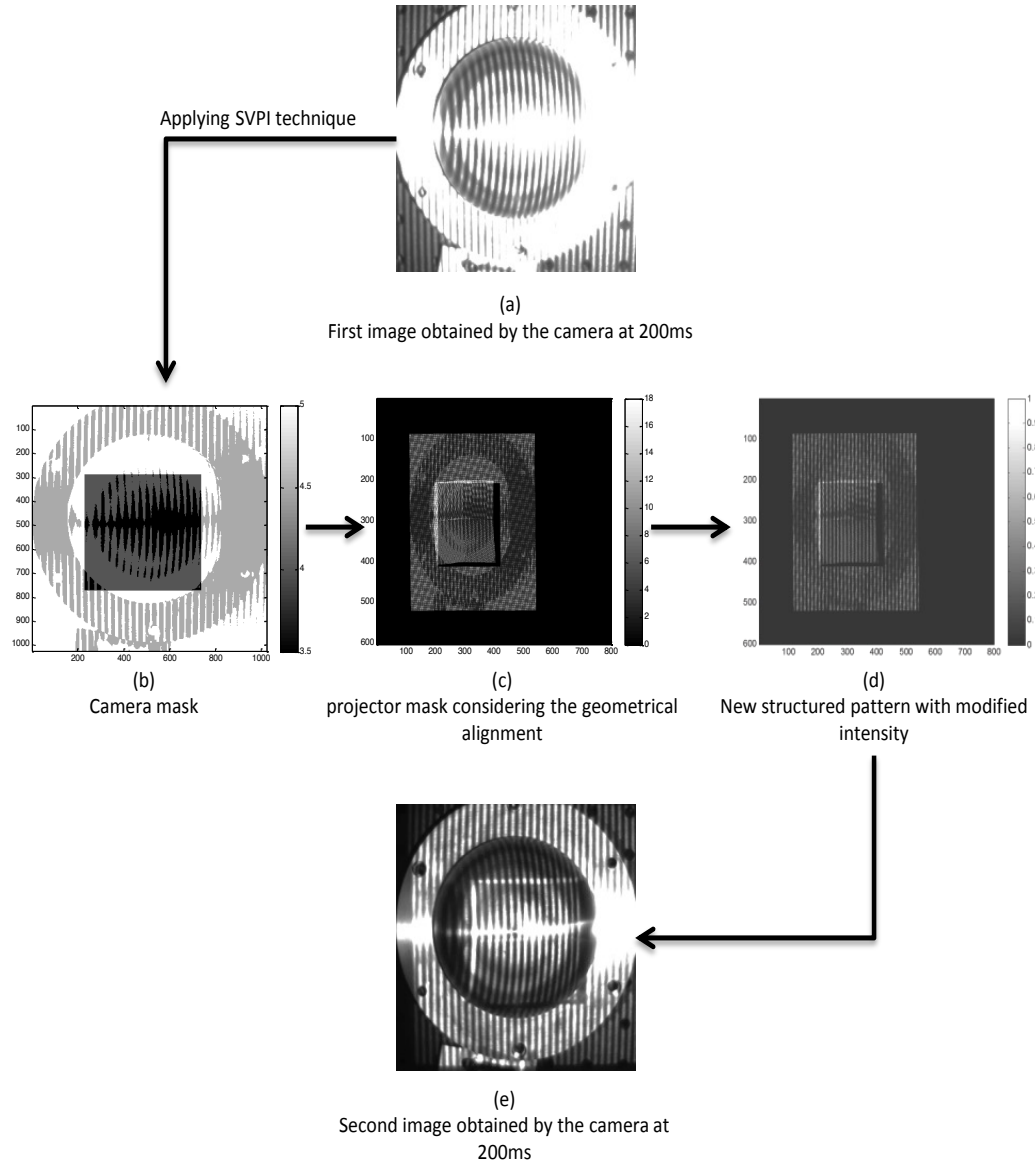


Figure 3.27: Application of the SVPI technique on an industrial spherical object in order to enhance dynamic range in a digital fringe projection setup.

Figure 3.28 illustrates a comparison between a single image obtained by the fringe projection setup without utilizing the SVPI technique at low and high exposure time, and a single image obtained by the fringe projection setup utilizing the SVPI technique. The dynamic range coefficient of the image taken by the SVPI technique is almost twice the dynamic range coefficient of the images obtained without SVPI technique.

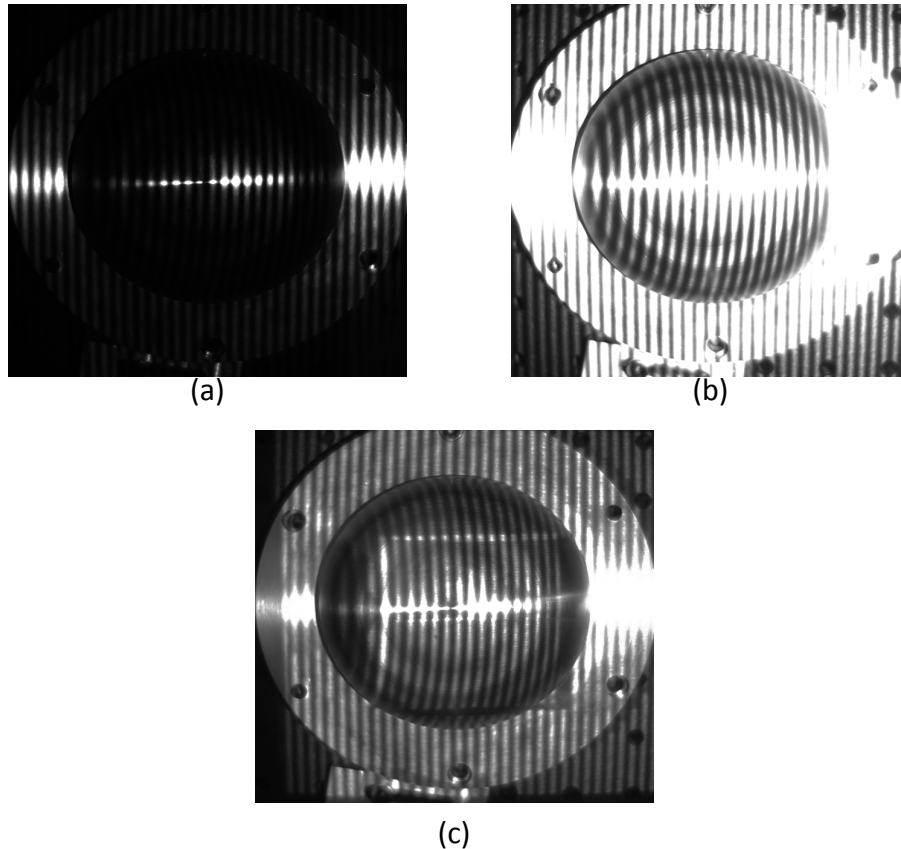


Figure 3.28: (a) Image obtained by the fringe projection setup at 20 ms camera exposure time before applying the SVPI. Dynamic range coefficient of this image is $K_{DR} = 48.36 \pm 0.02$. (b) Image obtained by the fringe projection setup at 250 ms camera exposure time before applying the SVPI. Dynamic range coefficient of this image is $K_{DR} 51.33 \pm 0.02$. (c) Image obtained by the fringe projection setup at 250 ms camera exposure time after applying the SVPI. Dynamic range coefficient of this image is $K_{DR} = 91.06 \pm 0.02$.

Once we had the high dynamic range image obtained by the SVPI technique, we applied a 4-step phase shifting algorithm [95] to calculate the corresponding phase map of the image, Figure 3.29 (a). As before, a median Gaussian filter was applied on the Fourier spectrum of the calculated phase. The filtered spectrum is then shifted to the center of the spectrum (frequency of zero), and the inverse Fourier transform applied as discussed in more detail in section 3.5. The obtained phase from the object is a wrapped phase with some discontinuity. A quality-guided unwrapping algorithm was applied on the wrapped phase to find the continuous phase of the object [94]. Figures 3.29 (b) and 3.29 (c) show the wrapped and unwrapped phase of the outer surface of the industrial object respectively.

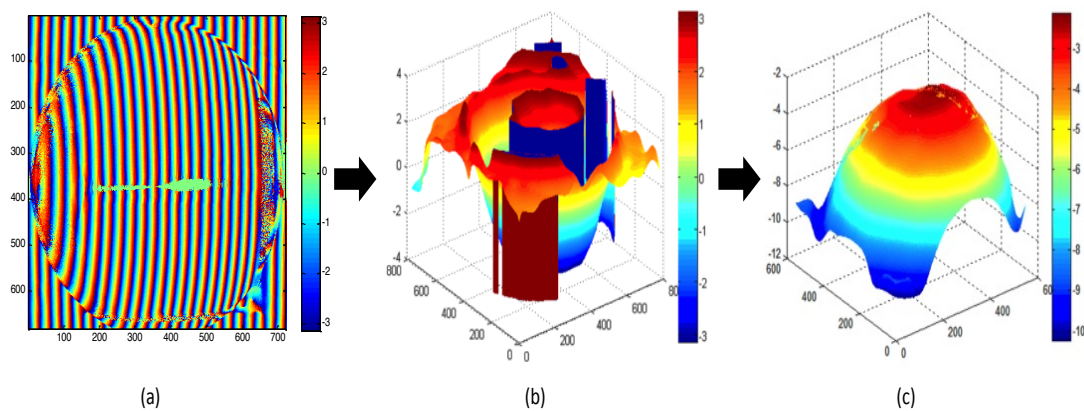


Figure 3.29: (a) Phase of the sample calculated from a 4-step phase shifting algorithm, (b) wrapped phase map of the object, and (c) calculated unwrapped phase map of the object using quality-guided algorithm.

Since in the process of unwrapping the phase map of the object, we used the Gaussian filter in the Fourier spectrum of the phase, the sharp edges of the object are rounded. In order to estimate the sharp edges of the sample under the measurement, the unwrapped profile has been fitted to a hemisphere and a stitching code is generated in Matlab and was used to find the final profile of the object with sharp boundaries. Figure 3.30 shows the final 3D profile of the object. The calculated height of the outside hemisphere of the object is 5.294 ± 0.008 cm and its diameter is 10.579 ± 0.015 cm.

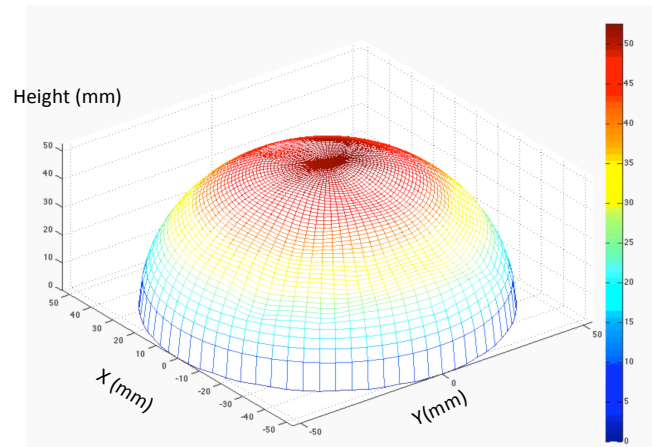


Figure 3.30: Three-dimensional profile of the outer surface of the industrial object using the SVPI technique in a fringe projection setup.

Figure 3.31 shows the radial profile of the calculated height map of the object with 5-degree of steps starting from the 10 mm distance from the center of the profile.

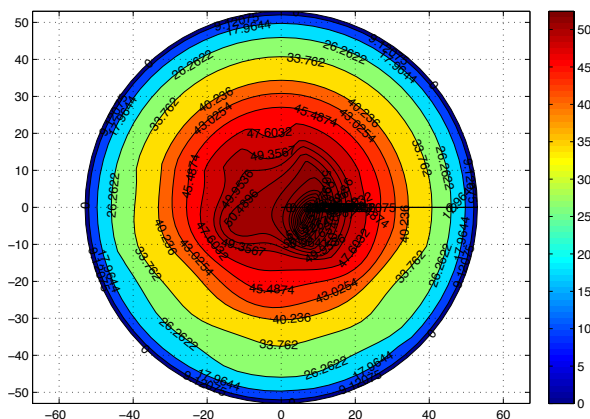


Figure 3.31: Radial profile of the industrial object using the SVPI technique in a fringe projection setup.

In the same manner, the hollow inside of the object is measured using the SVPI technique. Figure 3.32 shows the 3D profile of the inner surface of the object. The calculated height of the inner hemisphere side of the object is 7.016 ± 0.008 cm and its diameter is 9.637 ± 0.015 cm.

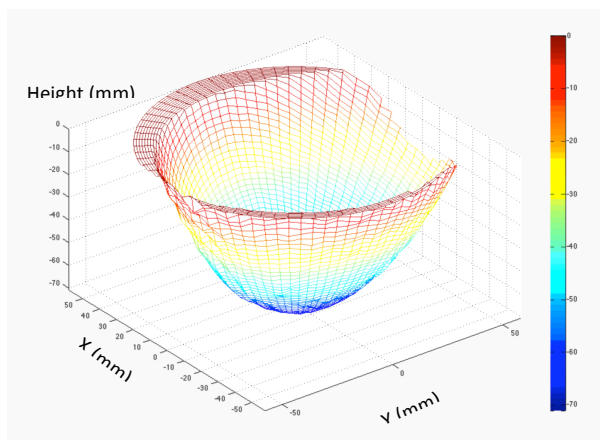


Figure 3.32: Three-dimensional profile of the inner surface of the industrial object using the SVPI technique in a fringe projection setup.

The radial profile of the calculated height with 5-degree of steps starting from the center of the profile is shown in figure 3.33.

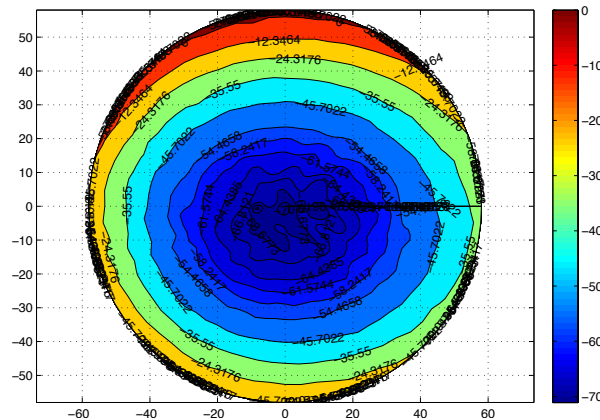


Figure 3.33: Three-dimensional profile of the inner surface of the industrial object using the SVPI technique in a fringe projection setup.

3.7. Discussion

In this chapter, we demonstrated that SVPI technique can enhance dynamic range in a digital fringe projection profilometry system by recursively controlling the intensity of the projected pattern at pixel level based on the feedback from the reflected pattern obtained by the camera.

As the result of HDR imaging we were able to reconstruct a full-field 3D profile of specular objects with steep slopes with different sizes and shapes more precisely in comparison to what can be obtained by a conventional fringe projection system.

Since the technique is recursive, it is applicable for profilometry of objects with a very wide range of optical reflectivity. The only limiting factor for enhancing the

dynamic range using SVPI technique is the physical limitations in the system such as camera noise, and the illumination performance of the projector.

Furthermore since dynamic range enhancement is achieved at multiple steps we can reduce error caused by pixel bleeding by defining the proper parameters in the algorithm such as the " k " value.

Finally, this method to achieve a HDR imaging system can be applied to many existing fringe projection profilometers with digital projection without any hardware change requirements.

CHAPTER 4: DYNAMIC RANGE ENHANCEMENT IN LASER INTERFEROMETERS

4.1. Introduction

The dynamic range of a conventional camera limits the resolution of laser interferometer systems. When two Gaussian beams are superimposed, the resultant interferogram has a bright central part, which fades into a darker region when moving away from the center with no obvious border. As a result, a single image does not fully capture information from all regions. If we set the exposure time to optimize the image for the dark zones, the correct intensity and phase information of the bright zones are lost since the corresponding pixels of the bright regions on the camera sensor become saturated. Likewise, if we set the exposure time to optimize the signal for the bright zones, detailed information of the dark zones is lost, Figure 4.1. Furthermore, if the test object under measurement shows a wide range of reflectivity due to its form or composition, the limited dynamic range of the conventional cameras will become even more problematic. Therefore, developing a system that enhances the dynamic range of laser interferometry systems would be very useful for a reliable demodulation of the interference pattern, and has many applications [96] [97] [98] [99] [100].

A typical method to enhance the dynamic range in laser interferometry systems, as discussed in chapter 1, is to obtain the response function of the imaging sensor and compute the true value of each pixel by acquiring multiple images with different exposure times of a static scene [46] [47].

In this chapter we apply the concept of the Spatially Varying Pixel Intensity (SVPI) to laser interferometers. In order to demonstrate this technique we used a Michelson laser interferometer. However the technique can be applied on any other type of laser or white light interferometers as well.

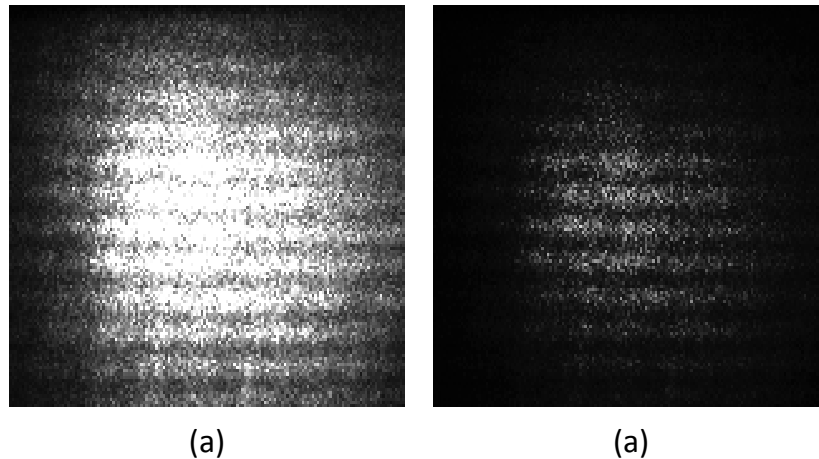


Figure 4.1: (a) An interference pattern obtained from a Michelson laser interferometer at camera exposure time set to 300 ms, and (b) an interference pattern obtained from a Michelson laser interferometer at camera exposure time set to 50 ms.

As discussed in chapter 3, the goal of SVPI technique is to recursively control the irradiance received on the imaging sensor at the pixel level to preserve more reliable information from the reflected light. In a digital fringe projection system, this goal can be fulfilled by controlling the intensity of the projected pattern in the computer, hence no physical modification is required in the system. In a laser interferometry system, we control the intensity of light reaching the imaging sensor by inserting a spatial light modulator (SLM) in front of the imaging system. The SLM is a device which spatially

modulates and controls the intensity of the light. There are different types of SLM, which can broadly be categorized into two groups: i) Electrically Addressed Spatial Light Modulators (EASLM), and ii) Optically Addressed Spatial Light Modulators (OASLM) [101].

In our experiment we used a liquid crystal modulator switched by thin-film transistors (TFT), which is in the OASLM category. Figure 4.2 shows a schematic of a liquid crystal TFT spatial light modulator. The major components of this device are the back panel, a liquid crystal (LC) layer, and the front and back polarizer layers. The back panel consists of 600×800 pixels connected by horizontal and vertical lines. Each pixel includes a TFT to which a charge storage capacitor is attached. The voltage across the capacitor can be changed using the control circuitry. As a result, the local electric field can be controlled at each pixel and hence the polarization of the light as well. This leads to controlling the intensity of light that can be transmitted through each pixel.

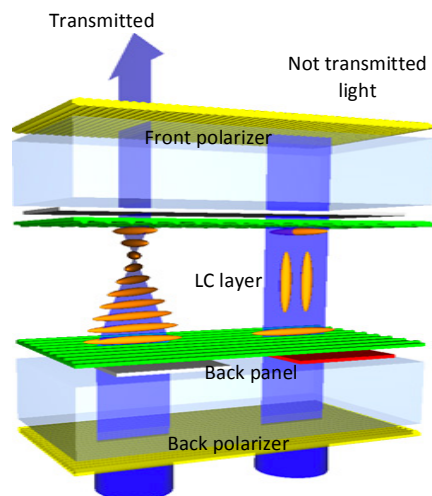


Figure 4.2: A schematic of a liquid crystal spatial light modulator by a TFT switch [102].

First the experimental setup used to implement the SVPI technique in laser interferometry will be discussed. The measurement procedure of SVPI technique to enhance the dynamic range in a laser interferometer will be discussed in section 4.3, and finally the results will be given in section 4.4.

4.2. Experimental Setup

4.2.1. Instrumentation

A schematic of a Michelson laser interferometer with enhanced dynamic range is shown in figure 4.3. Light from a He-Ne laser ($\lambda = 632.8$ nm) was coupled into a single mode fiber and collimated at the other end of the fiber using a 10x objective lens. The collimated beam was transmitted through a 50-50-beam splitter where one beam travels through the reference arm and reflects back from the tilted reference mirror. The mirror is tilted in order to obtain linear fringes (called carrier fringes) in the interferogram. The other beam travels through the object arm to illuminate the measurement sample, which is a super polished flat mirror with nominal flatness of less than $\frac{\lambda}{10}$ as reported by the manufacturer. Reflected beams from the mirror and the measurement sample combine and produce an interference pattern.

The interference pattern was magnified using a magnifying lens system and was projected onto the spatial light modulator. The SLM used in this experiment was a liquid crystal display (LCD) taken from a PowerLite S5, EPSON projector, which is optimized for light in the red region of the visible spectrum.

The SLM can control the intensity of light transmitted through each pixel using a controller unit. The pattern on the SLM was imaged on an AVT P Guppy F-146 camera

using a zoom lens. The obtained image is transferred to a computer for further phase analysis.

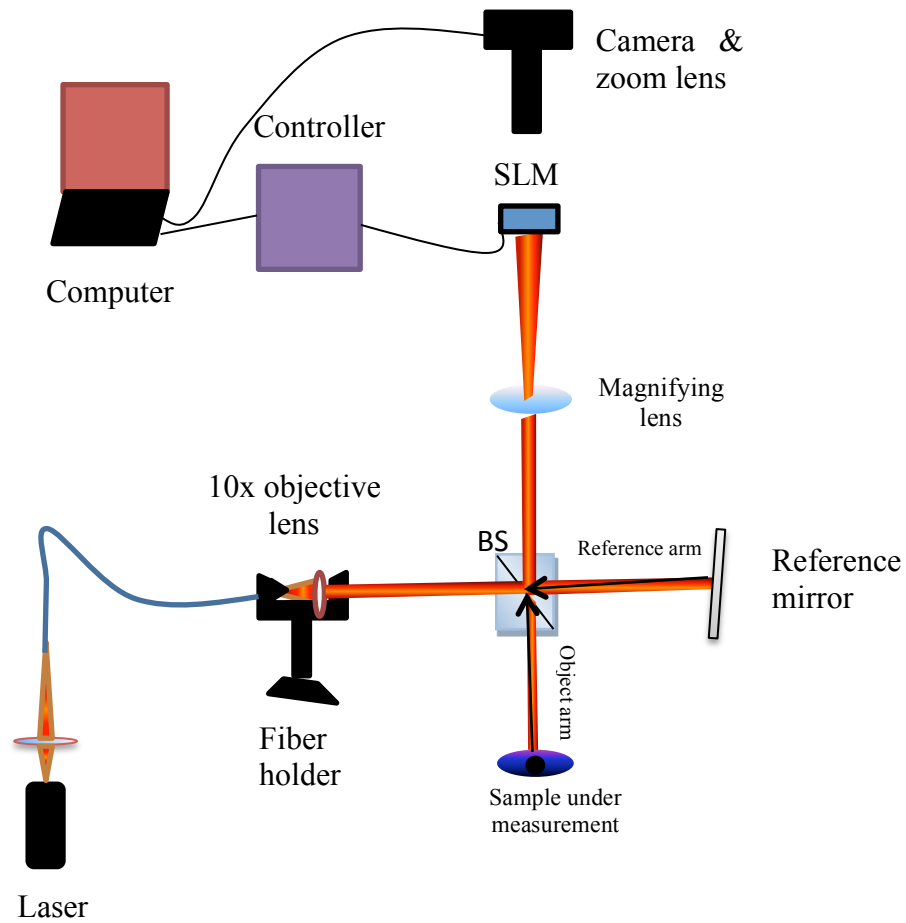


Figure 4.3: A schematic of a Michelson interferometer and the experimental setup used to demonstrate dynamic range enhancement technique.

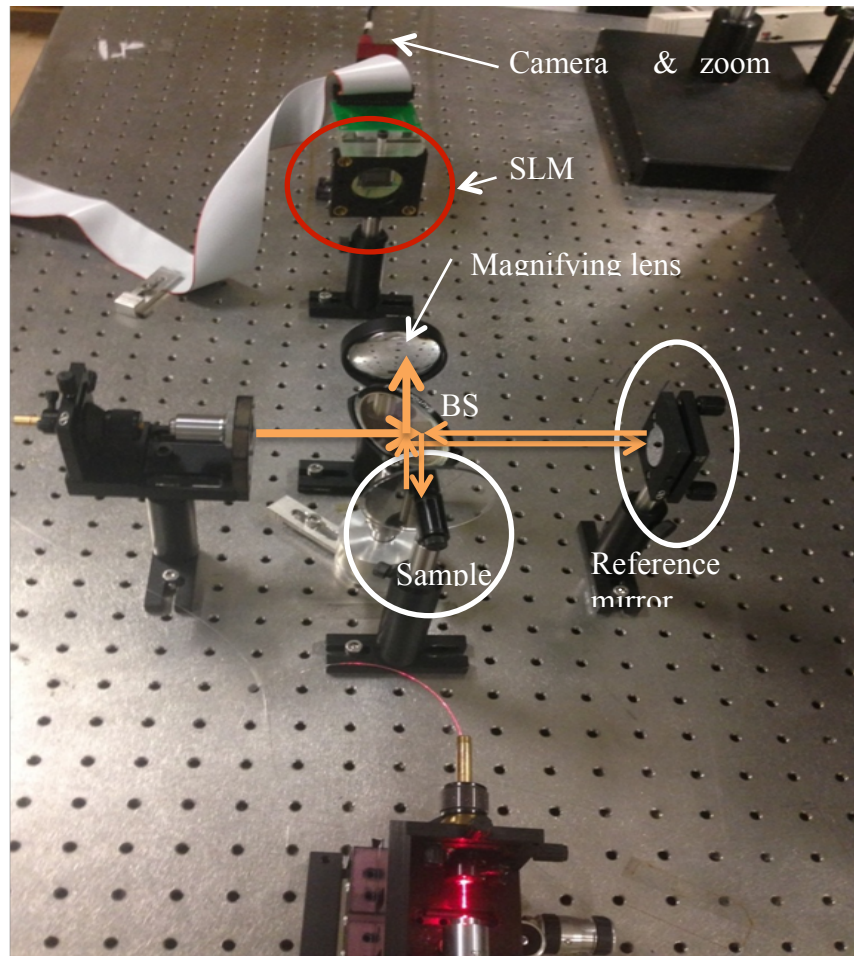


Figure 4.4: Experimental setup used for dynamic range enhancement in a Michelson laser interferometer using the SVPI technique.

4.2.2. Geometrical Alignment

Geometrical alignment is essential between the SLM and the camera sensor. To geometrically align the system, specific voltage was applied to each pixel of the SLM to create a known pattern on the SLM, figure 4.5 (a). The pattern on the SLM is then imaged on the camera. A linear transformation was used between these two patterns and

based on that, the transformation matrix, T_{ij}^{cp} , and the translation vector, S_{ij} , were computed.

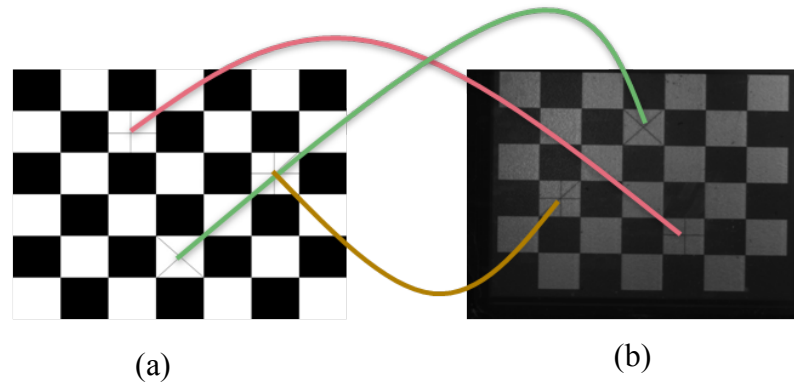


Figure 4.5: Geometrical alignment between the SLM and the camera.

Each pixel on the camera can be traced back to a pixel on the SLM using equation 1, where P_{ij} is a pixel of the SLM and C_{ij} is the corresponding pixel of the camera.

$$P_{ij} = T_{ij}^{cp} \times C_{ij} + S_{ij} \quad (4.1)$$

4.3. SVPI Algorithm Measurement Procedure

Figure 4.6 shows a flowchart of the algorithm developed to enhance the dynamic range in laser interferometry. The basic concept of the algorithm is similar to the one presented in chapter 3 for dynamic range enhancement in a digital fringe projection system, although some modifications are necessary to apply this concept in laser interferometers. The procedure is explained below.

First, a specific voltage was applied to the SLM in order to maximize the intensity of light passing through all pixels. The exposure time and gain of the camera were adjusted to obtain an image, which is the brightest image with no saturated pixels. The average value of the bright fringes was chosen to be the maximum acceptable intensity, I_{\max} . Then, a new voltage was applied to the SLM to allow the minimum possible intensity of light passing through each pixel of the SLM. It is important to note that, in practice, this minimum value is not zero. The exposure time and gain of the camera were adjusted until all of the pixel's values were above the noise level of the camera. At this point, the exposure time and gain of the camera were fixed for the rest of the experiment and I_{\min} , the minimum acceptable intensity, was defined and calculated as the average intensity of the dark fringes.

In order to quantify how effectively the SVPI technique improves the dynamic range of the system at each step, the dynamic range coefficient is introduced as below:

$$K_{\text{DR}} = \frac{N_p}{N_t - N_s} \quad (4.2)$$

where N_p is the number of pixels with intensities within the acceptable dynamic range of the camera (I_{\min} to I_{\max}), N_t is the total number of pixels in the camera image, and N_s is the number of pixels, in which their intensities cannot be adjusted as discussed in the previous chapter.

The noise level of the imaging system was determined by calculating the standard deviation of a sequence of images at different times (fluctuation of the light intensity

from the mean value). For our system, this number was determined to be $\delta = 1.15\%$. This value can be used to find the uncertainty in the dynamic range coefficient.

In order to find the uncertainty of the dynamic range coefficient, dynamic range coefficient of a pattern is calculated once based on all the pixels with the intensity I_{NP} where $I_{\min} < I_{NP} < I_{\max}$, and for $I_{\min} - \delta < I_{NP} < I_{\max} + \delta$. The difference between these two values results in the dynamic range coefficient uncertainty, δK_{DR} . This number for our system was determined to be $\delta K_{DR} = 0.09$.

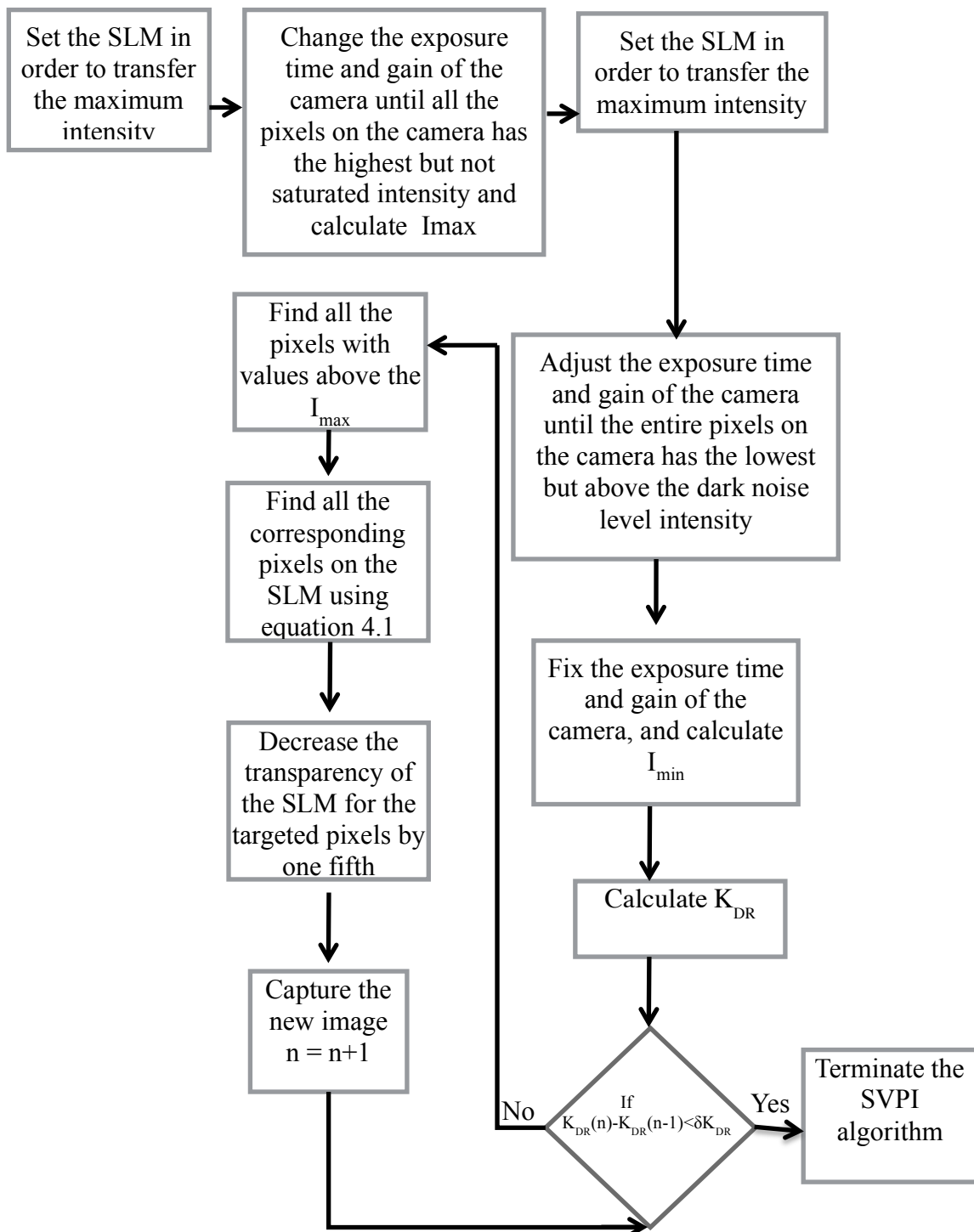


Figure 4.6. SVPI algorithm used to enhance the dynamic range of a laser interferometer.

4.4. Experimental Results and Discussion

Figure 4.7 shows an image taken by the camera with an exposure time set to 500 ms, and all the SLM's pixels are set to transmit the maximum possible light. The camera pixels corresponding to the central part of the image are mostly saturated and no correct intensity and consequently no phase information can be extracted from this region. The dynamic range coefficient of this image is $K_{DR} = 0.33 \pm 0.09$.

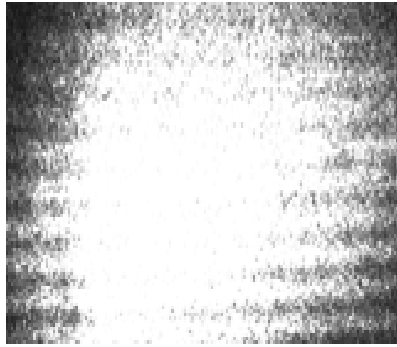


Figure 4.7. Image obtained by the camera at exposure time 500 ms.

We have applied the SVPI technique to this system. Initially, the SLM was adjusted to allow maximum transmission and the interferogram was recorded. Figures 4.8 (a) and 4.8 (b) show the transmission function of the SLM and its corresponding recorded pattern. Figure 4.8 (c) shows the transmission function of the SLM after the first iteration of SVPI algorithm. As shown in figure 4.8 (c), in the region where the intensity of interference pattern is above I_{max} , the SVPI technique adjusts the SLM's transmission function to reduce the intensity of light reaching the camera by 80%. The values on the SLM transmission coefficients were 0.2 for all the pixels corresponding to the saturated

pixels on the camera, and the remaining pixels' values were all one. Figure 4.8 (d) shows the interference pattern after this first step. Dynamic range coefficient of the interferogram, after the first iteration of SVPI algorithm, was increased to $K_{DR} = 0.68 \pm 0.09$, which shows more than twofold improvement.

Figure 4.8 (e) shows the SLM transmission function after applying the SVPI technique for the second time. In the area where the first iteration of the SVPI technique was able to compensate for the excessive transmission of light, and prevent saturation on the camera, the SLM transmission function values remained at 0.2. After applying the SVPI once there are still many saturated pixels at the central part of the image, therefore the transmission coefficients of corresponding pixels on the SLM were adjusted to 0.04 to reduce the light intensity at these pixels even more. Dynamic range coefficient of the interferogram was improved to $K_{DR} = 0.87 \pm 0.09$, which is about 30% improvement in the dynamic range from the second image and 128% improvement from the first image obtained by the camera. The transmission function of the SLM and its corresponding interference pattern are shown in Figures 4.8 (e) and 4.8 (f).

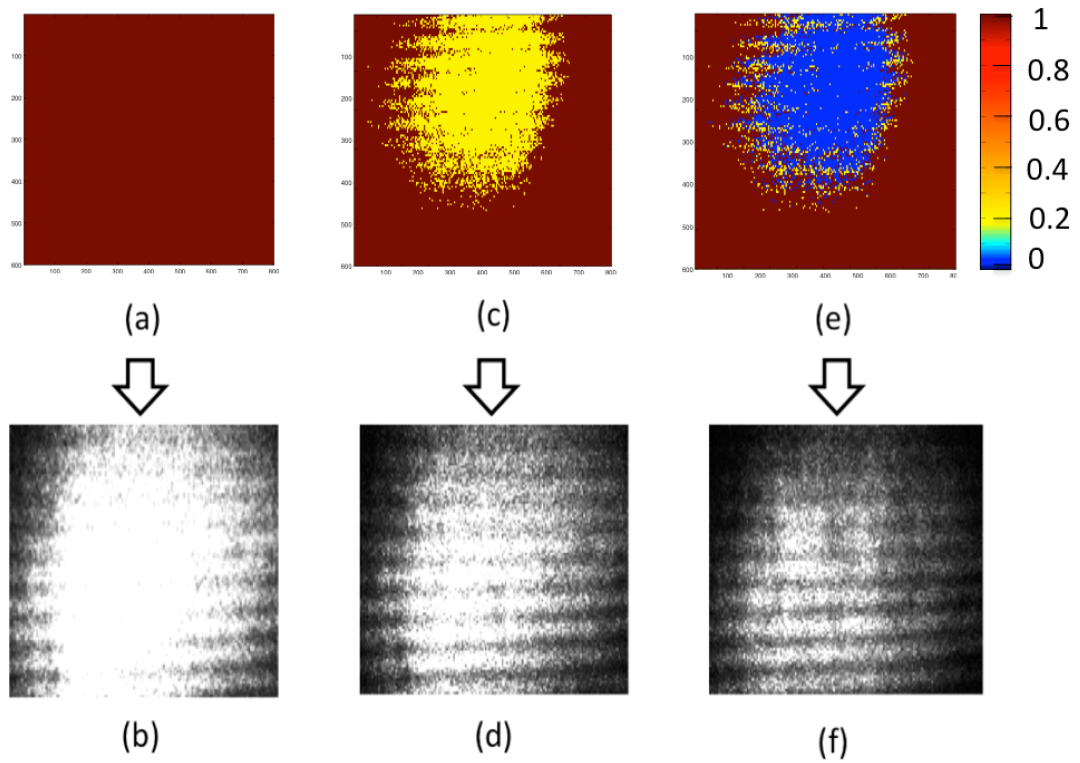


Figure 4.8: (a) Initial transmission of the SLM, (b) image obtained by the camera at exposure time 500 ms, (c) modified transmission of the SLM after the first iteration, (d) image obtained by the camera at exposure time 500 ms for modified SLM, (e) modified transmission of the SLM after the second iteration, and (f) image obtained by the camera at exposure time 500 ms.

In order to find the phase map of the interferograms, the discrete Fourier transform technique was applied to the images obtained by the camera at each step [90]. Phase information could not be retrieved from the initial interferogram, before applying the SVPI technique, due to high level of noise.

After applying the SVPI technique once, we were able to obtain the phase map from the interferogram of Figure 6(d). The 3D height map of the object obtained at this step is

shown in figure 4.9. The height variation is on the order of 0.3λ . Figure 4.10 shows the obtained 3D height map of the object after applying the technique for the second time. The height variation is on the order of 0.1λ , which is close to the nominal flatness of the mirror provided by the manufacturer.

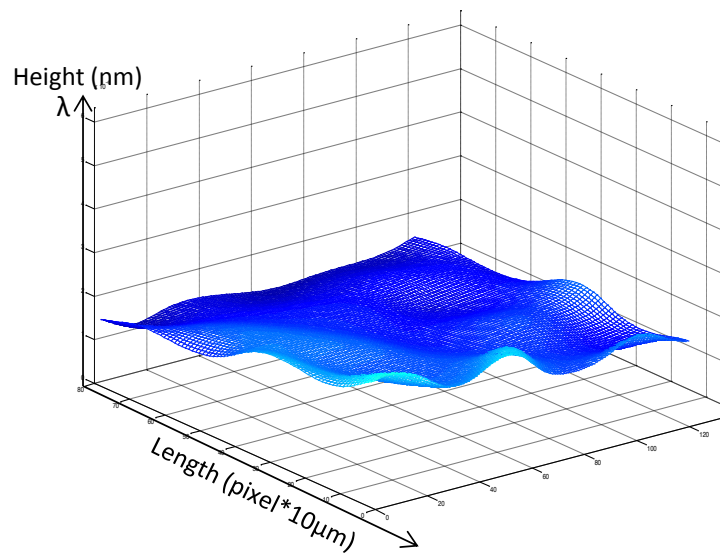


Figure 4.9: Three-dimensional profile of the flat mirror obtained from a Michelson laser interferometry after applying the SVPI technique once.

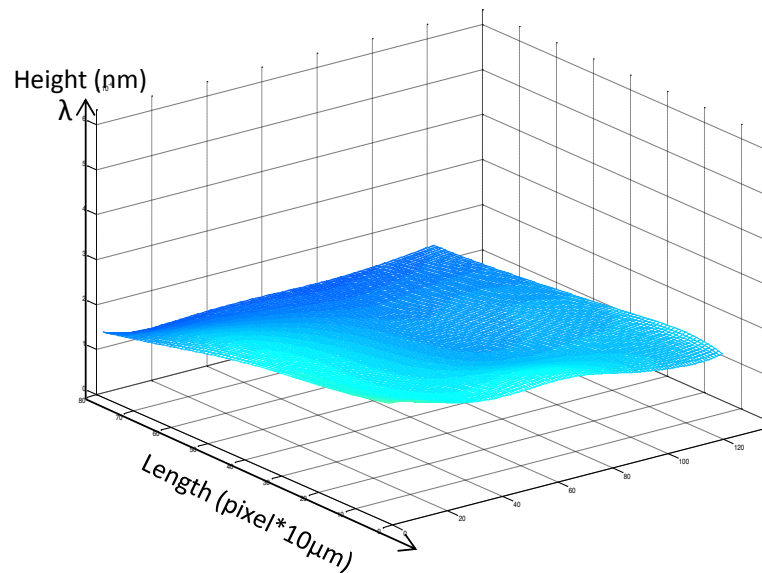


Figure 4.10: Three-dimensional profile of the flat mirror obtained from a Michelson laser interferometry after applying the SVPI technique twice.

4.5. Discussion:

Comparison of figures 4.9 and 4.10 clearly shows improved measurement precision. The results obtained indicate that the SVPI technique can enhance dynamic range of a laser interferometry system.

Higher dynamic range in laser interferometers enables us to inspect a large area of the object under measurement since we can simultaneously preserve the correct intensity information from the bright central part of the interferogram as well as its dark borders. Furthermore, the results obtained from an optically flat surface, indicate that the SVPI can also enhance the signal to noise ratio.

Enhancing dynamic range in laser interferometers is particularly important for metrology of surfaces made from different materials such as microelectronic circuits and those with curved surface features and steep slopes.

Our experimental results demonstrated that an interferogram with low dynamic range coefficient with high noise level could be transformed into an interferogram with high dynamic range coefficient with reduced noise.

CHAPTER 5: THREE- DIMENSIONAL PROFILOMETRY OF OBJECTS BASED ON ABSORPSION AND OPTICAL FREQUENCY CONVERSION

5.1. Introduction

Recent advancement in manufacturing of objects with unique raw materials offers new challenges in optical surface metrology of such objects. In the semiconductor industry, superior mechanical properties of micro and nano-crystalline materials composed of metal alloys; ceramic and/or polymers give a boost in manufacturing of high-power, high temperature and fast semiconductor devices. However, these types of materials demonstrate unique optical properties, which lead to serious limitations in optical surface metrology of these devices. For example, to enhance the electrical, thermal and mechanical properties of some objects such as solder bumps used in flip chip industry, nanoparticle alloys of gold, silver or/and copper is usually distributed uniformly on them. The presence of these metal alloy nanoparticles creates hot spots in the intensity of light reflecting back from such objects, which consequently creates difficulties in the optical profilometry of such objects.

In another example, the remarkable mechanical, electrical, and thermal properties of carbon nanotubes [103], [104] makes them an extremely powerful material in manufacturing of nano-electronic and nano-mechanical devices. However, from the optical point of view, carbon nanotube materials have strong absorption (more than 98%) and very low reflectance (less than 2%) in a very wide spectral range [105]. They can be considered as a black body material. As discussed in chapter one, the basic principle of

optical surface metrology tools is to project an optical signal to the object and analyze the reflected light from the object or transmitted light through the object. Therefore, none of the existing optical metrology tools could measure the surface of an object composed of a black body material, since there would be no or very low reflectivity or transmissivity from such objects. Currently surface measurement of dark or gray objects is a challenge due to the low signal to noise ratio of the captured image by the imaging system.

In this chapter, we introduce a new technique to measure the 3D profile of an object composed of unique raw materials based on fringe projection techniques and optical wavelength conversion principle.

The principle of fringe projection technique is discussed in chapter two in detail. In the rest of this chapter, first, a brief overview on the basics of optical wavelength conversion based on absorption and emission in solid-state materials will be discussed. Then, an experimental setup is used to show the concept of profilometry based on optical wavelength conversion on a hemispherical object, composed of a specific polymer, which fluoresces in the red spectrum under the illumination of blue light or ultra-violet wavelength. In the last part of this chapter, 3D profile of a dark, non-reflective object is measured based on optical heat induction in the object.

5.2. Absorption and Emission in Solid State Materials

Light can be absorbed by a solid as the result of intraband transitions [106]. When the energy of the light exceeds the band gap energy of the solid, the electrons absorb the energy of the light and the electron jumps from a lower energy level to a higher excited level. The reverse process can happen when the electrons in the excited states drop to the lower level by emitting light usually with the longer wavelength than the initial

wavelength of the incident light (Stoke's shift [107]). The emission process in solids is called luminescence.

The intraband transitions are observed in all types of solids, however luminescence does not occur for all solids upon the absorption of light. The process of returning the excited electron to a lower level can be through emitting a photon (radiative process) or by releasing the excess energy in the form of heat (non-radiative process).

Broadly, solid state materials can be divided into four main groups based on their optical properties, i) crystalline insulators and semiconductors, ii) glasses, iii) molecular materials, and iv) metals.

Most insulators are highly absorptive in the infrared, and ultraviolet spectrum. The infrared absorption happens due to the vibrational excitations of the crystalline lattice, and the ultraviolet absorption happens due to the absorption by bound electrons. The infrared absorption causes electrons to jump to the higher vibrational states, and when they decay it may cause the object to heat up locally (non-radiative emission). The ultraviolet absorption causes electrons in ground state to jump to the excited electronic states with large amount of energy. Ultimately the excited electrons will return to the ground state by emitting a photon (radiative process) at a longer wavelength [107].

Optical properties of glasses are usually the same as insulators. They are transparent in visible spectrum, and highly absorptive in ultraviolet spectrum due to the electronic transitions. They also emit a broad emission bands mainly in the blue-green spectral region depending on the glass composition. Therefore glasses can absorb the ultraviolet light and emit in visible spectrum [107].

Semiconductors and molecular materials are strongly absorptive in near infrared and visible spectrum; hence they are not optically transparent. These types of materials exhibit strong luminescence when their electrons in the valence band jump to the conduction band. Figure 5.1 shows a schematic of the absorption and emission process in a semiconductor.

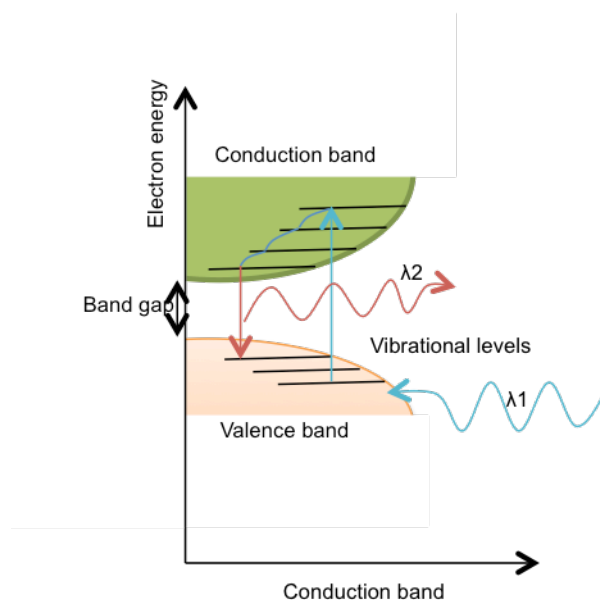


Figure 5.1 Schematic diagram of the vibrational-electronic transitions in a semiconductor.

Metals have very high reflectivity in the infrared to the visible range of the spectrum [107]. The high reflectivity in metals is the result of light interaction with the free electrons of the metal based on Drude-Lorentz free electron model of metals [107]. If the incident light source has a frequency above the plasmonic frequency of the metals, usually above the ultraviolet spectrum, the metals become transparent, and the effect is

called the ultraviolet transparency of metals. Also, intraband transitions are possible in metals from states below the Fermi level [107] to empty levels above it, which can reduce the reflectivity of the metals, but in general, metals do not luminescence.

Therefore, semiconductors, insulators, glasses and molecular materials (such as organic compounds) can either emit light from their surfaces or heat up, hence emitting long wavelength infrared radiation once they are illuminated with the light source at the proper wavelength.

In this chapter, we have combined the principle of fringe projection technique with the wavelength conversion phenomena to improve the signal to noise ratio of the interferogram obtained from objects with specific compositions.

5.3. Profilometry of a Hemispherical Polymer Surface using Optical Wavelength Conversion

Hemispherical shape objects composed of a specific polymer, which absorbs the blue spectrum of light and emits a fluorescence signal in the red spectrum, were made as test samples. Also, small metal chips were added to their surfaces to create hot spots under illumination in the image obtained by the camera. Figure 5.2 shows two such prepared objects.



Figure 5.2 Hemispherical shape objects composed of a unique polymer combination.

A sinusoidal fringe pattern at the blue wavelength was projected onto the sample. A portion of the blue light reflects back from the surface and some light is absorbed by the surface, which causes the object to fluoresce in the red spectrum. First, the combined reflected blue, and the emitted red signal from the object were observed using a CMOS color camera. Figure 5.3 shows a schematic of the setup implemented in the experiment as well as the reflected pattern obtained by the camera.

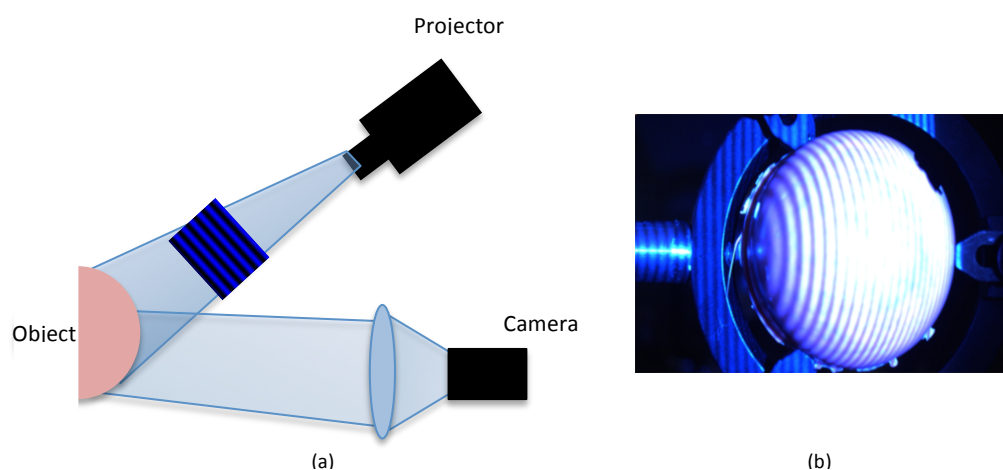


Figure 5.3 (a) A schematic of the fringe projection setup used for profilometry of a hemispherical shaped object composed of a specific polymer, and (b) the reflected image obtained by the CMOS camera.

Due to the spherical shape of the object and the added metal chips to the surface, a large area of the obtained pattern is saturated. Consequently, the phase information of the saturated pixels cannot be recovered correctly.

Then, a long pass optical filter, which only passes wavelengths greater than 550 nm is placed in front of the camera to block the blue light reflecting back from the sample. As a result only the red light, which is the fluorescent signal from the object's surface reaches the camera's sensor. Figure 5.4 shows the experimental setup used to implement the concept, as well as the fluorescence pattern emitted from the sample's surface.

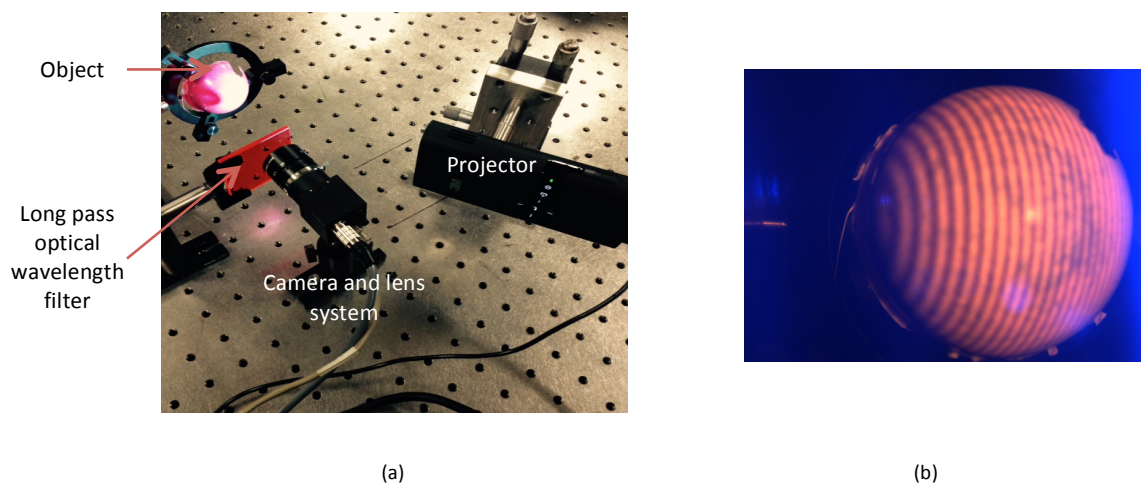


Figure 5.4 (a) The experimental setup used for profilometry of a hemispherical shaped object using the wavelength conversion technique, and (b) the emitted fluorescence pattern from the object obtained by the CMOS camera.

The image obtained in figure 5.3 (b) is the emitted pattern from the object's surface due to the material excitation. Each point on the object, which was illuminated by the

blue light source, becomes a secondary point source itself and fluoresces the red light in all directions. As a result, despite the steep slopes of the object, the light uniformly reaches the camera from the entire object.

In general, the curved shape of the object effectively acts as a lens (or curved mirror) with a given numerical aperture with an optical axis normal to the surface, locally. This will limit the ability of the system to collect the entire signal reflecting back from the surface. However, the wavelength conversion produces light in all directions that is not dependent on the shape of the object and the emission solid angle could exceed 2π allowing more light to be collected by the imaging system.

Figure 5.5 schematically compares the amount of light reaching the detector in the case where the camera observes the reflected light from the object surface versus the case where the camera observes the emitted fluorescence light from the object's surface. In the reflected mode, the amount of light reaching the camera is highly affected by the geometry of the object, while in the fluorescence emission mode, the amount of light reaching to the camera is less dependent on the shape of the object.

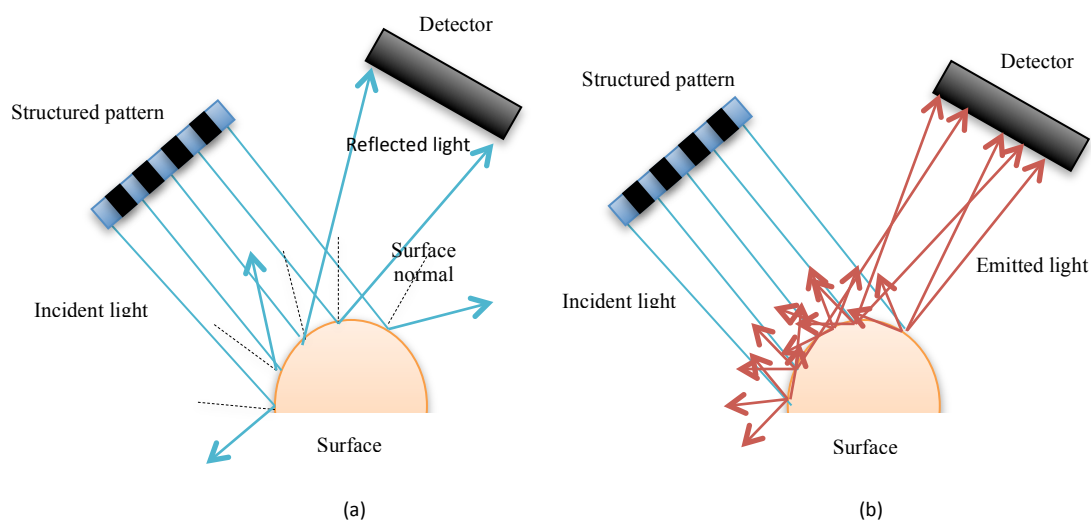


Figure 5.5: (a) A schematic of the fringe projection profilometry based on reflected light, and (b) a schematic of the fringe projection profilometry based on wavelength conversion.

Figure 5.6 (a) shows the phase calculated by the four-step phase shifting algorithm of the obtained images from the reflected blue light, and figure 5.6 (b) shows the phase of the fluorescence emitted light.

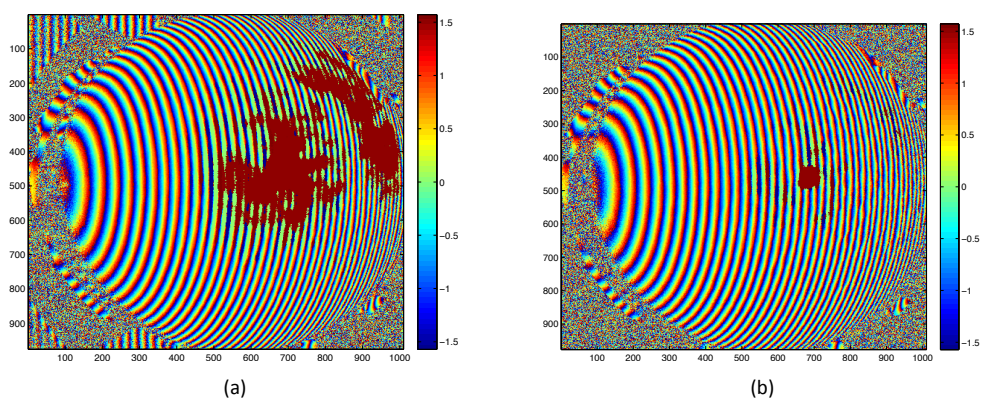


Figure 5.6 (a) Calculated phase of the blue reflected light using a four-step phase shifting algorithm. (b) Calculated phase of the red fluorescence emitted light using a four-step phase shifting algorithm.

Figure 5.7 (a) shows the Fourier spectrum of the calculated phase in the reflection mode, and figure 5.7 (b) shows the Fourier spectrum of the calculated phase in the fluorescence mode.

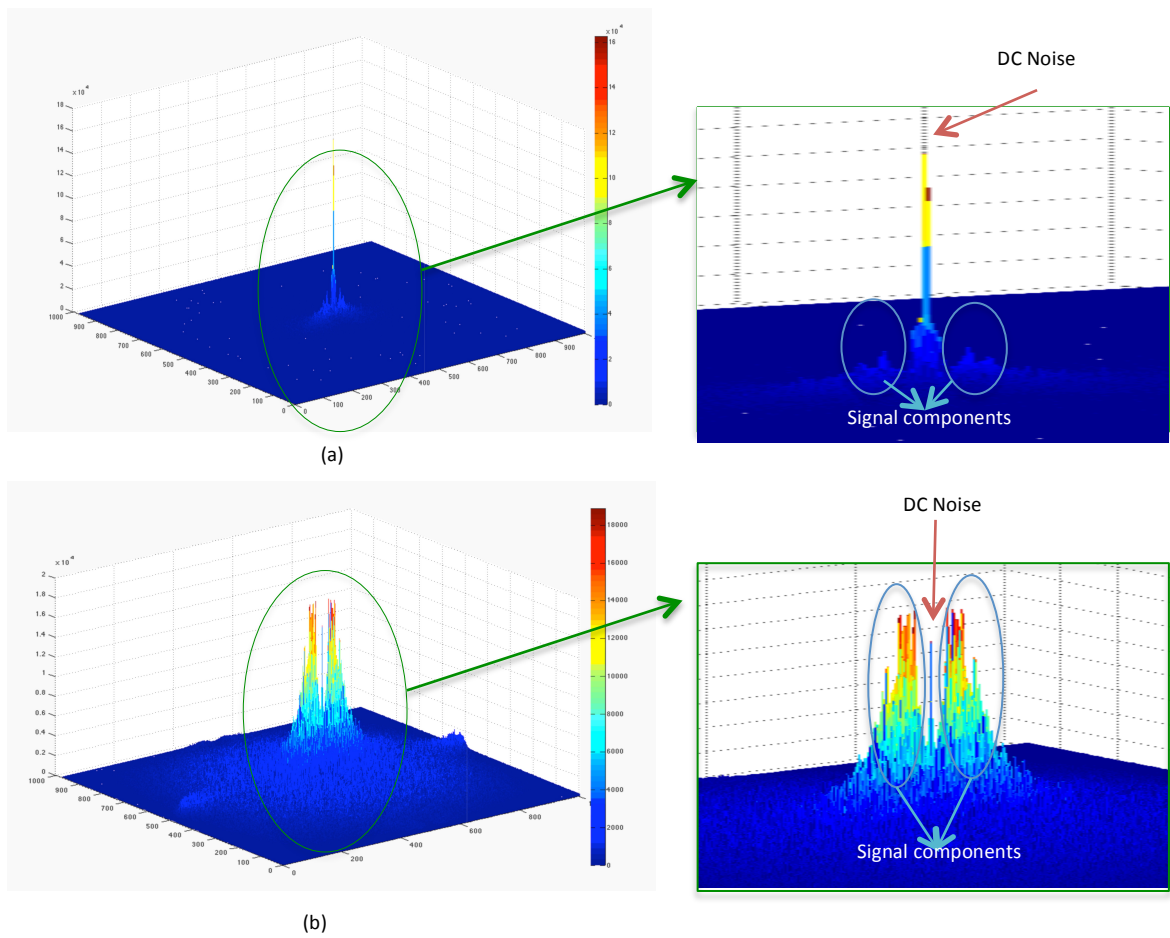


Figure 5.7 (a) Fourier spectrum of the phase component of the reflected blue signal, and (b) Fourier spectrum of the fluorescence red signal.

The Fourier spectrum of the calculated phase of the reflected blue pattern contains a large amount of noise, which dominates the signal. The signal to noise ratio for this image is 18%, Figure 5.7 (a).

The noise level for the fluorescence pattern is reduced significantly, Figure 5.7 (b), and the signal to noise ratio of this pattern is 116% which indicates six fold improvement in the signal to noise ratio.

In order to obtain the unwrapped phase map of the signal, we used a window Fourier transform algorithm combined with the quality-guided unwrapping technique. Figure 5.8 (a) shows the unwrapped phase map calculated from the blue reflected signal and figure 5.8 (b) shows the unwrapped phase map calculated from red fluorescence emitted signal.

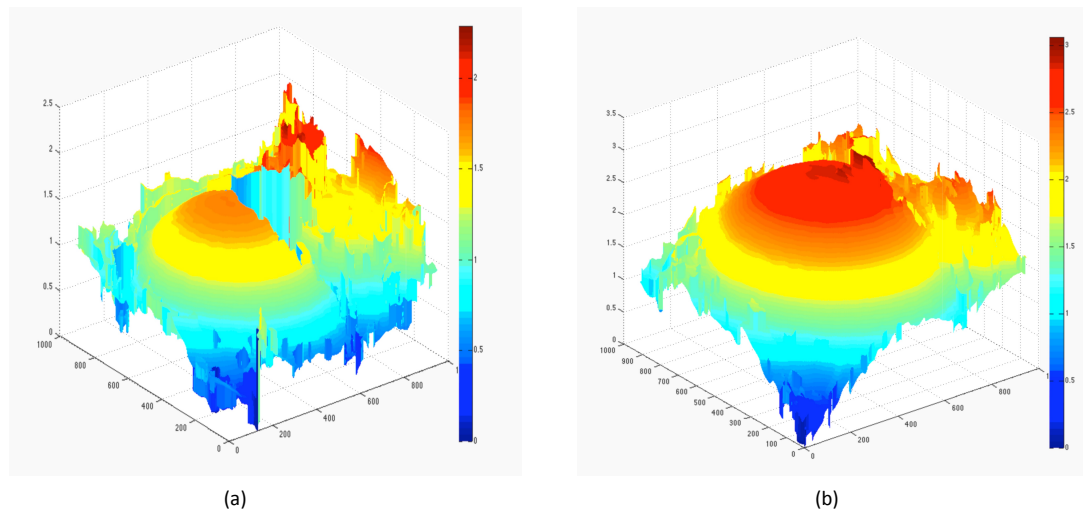


Figure 5.8 (a) Unwrapped phase map constructed from the blue reflected pattern, and (b) unwrapped phase map constructed from the emitted red pattern.

Comparison between Figures 5.8 (a) and 5.8 (b) clearly shows that using optical wavelength conversion in situations where the test object can be excited to fluoresce improves the signal to noise ratio in a fringe projection profilometry system, hence, a more accurate and reliable phase can be obtained from the object with complex geometry compared to the conventional fringe projection profilometry.

As mentioned in section 5.2, some of the materials do not fluoresce upon absorption of the light. Instead they heat up in a non-radiative process. In the next section difficulties in metrology of dark, non-reflective objects and the principle of light absorption and heat induction in such objects will be discussed.

The concept of wavelength conversion from visible spectrum to deep infrared (heat) spectrum will be used in a fringe projection system to enhance the signal to noise ratio and to demonstrate an optical technique for the metrology of dark, non-reflective objects.

5.3. Optical Profilometry of Dark Objects Based on Optically Induced Heat

Profilometry of dark/gray objects is currently a challenge in the field of optical metrology due to low or no light being reflected from this type of objects.

When a light beam is incident on a bulky medium, some portion of the light reflects from its surface while the rest enters the medium and propagates through it. If the frequency of the light resonates with the transition frequencies of the atoms in the medium, absorption occurs, and the beam will be attenuated as it progresses through the medium. The absorption of light by the medium is quantified by the absorption coefficient, which is defined as the fraction of the power absorbed in a unit length of the medium (Beer's law) [107]. A black, non-reflective object absorbs almost all of the

energy of the incident light and locally heats up as a result of thermal agitation of its composing molecules [107]. The thermal energy generated in the medium is then dissipated into its bulk by conduction. The Fourier law [108] describes the conduction rate in the matter as,

$$\mathbf{q} = -kA\nabla T \quad (5.1)$$

where \mathbf{q} is the heat flow rate vector, k is the thermal conductivity of the medium, A is the cross-sectional area in the direction of the heat flow, and ∇T is the gradient of the temperature. When light hits the object, some portion of its irradiant power converts to heat energy. Considering the linear conversion between the generated heat and the irradiant power, $q = \eta \cdot P = \eta \cdot I \cdot A$, η is a constant, in which its value depends on the absorption and thermal properties of the material, I is intensity of the light and A is the cross-sectional area in the direction of illumination. The Fourier law in terms of intensity can be written as,

$$\nabla T = -(\eta/k)I\mathbf{n} \quad (5.2)$$

where \mathbf{n} is the unit vector in the direction of heat flow on the surface. When a material is illuminated by a sinusoidal light pattern $I(x,y) = I_0 \cos(\omega_x x + \omega_y y)$, where $\omega_x = 2\pi\nu_x$ and $\omega_y = 2\pi\nu_y$ are the angular modulation of the pattern in x and y directions, its surface temperature profile can be obtained by solving Eq. 5.2.

$$T(x, y) = -\frac{\eta I_0}{k} \left(\frac{1}{\omega_x} + \frac{1}{\omega_y} \right) \cos(\omega_x x + \omega_y y) \quad (5.3)$$

Therefore, the heat pattern created by a sinusoidally varying light pattern is also a sinusoidal, in which the height distribution of the test sample modulates the phase distribution of the heat pattern, $\phi(x, y)$.

$$T(x, y) = T_0 \cos(\omega_x x + \omega_y y + \phi(x, y)) \quad (5.4)$$

where,

$$T_0 = -\frac{\eta I_0}{k} \left(\frac{1}{\omega_x} + \frac{1}{\omega_y} \right) \quad (5.5)$$

Therefore by analyzing the heat pattern with one of the common fringe analysis techniques discussed in chapter 1, we are able to extract the modulated phase and consequently reconstruct the 3D profile of a dark object.

Another important factor that needs to be addressed is finding the proper acquisition time in which the height information of the object is correctly reflected in the phase of the heat pattern. Absorption and thermal properties of material affect the energy transfer process between the light source and the sample, and therefore the time required for converting the maximum energy of the light into heat can vary from one object to another. Also the heat created on the surface will eventually dissipate through the material bulk, which results in a change of the periodic shape of the heat pattern and consequently disturbs the recorded signal. Therefore it is essential to find an optimum

time, which is long enough for the object to convert the maximum energy of the projected light into the heat, and short enough to avoid heat diffusion.

5.3.1. Experimental Setup and Results

A schematic of the experimental setup for 3D profilometry of a dark object using the heat induction technique in fringe projection is shown in Figure 5.9.

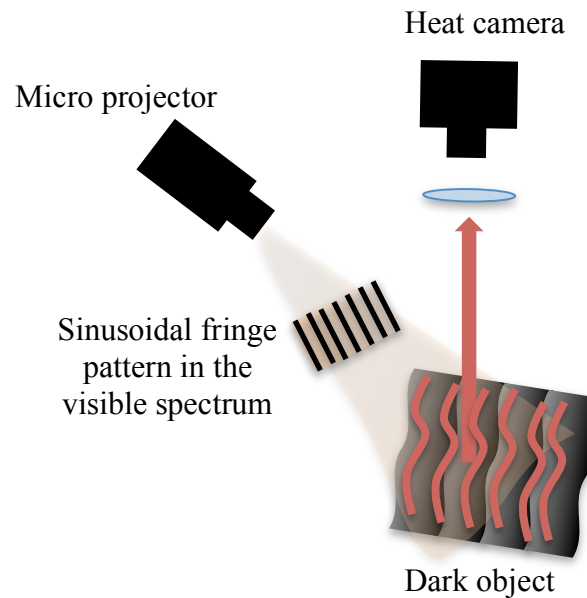


Figure 5.9: A schematic of a heat induction technique using a fringe projection configuration.

We used a conventional projector to illuminate the sample with a sinusoidally structured pattern in the visible wavelength. It should be noted that depending on the absorption properties of the object under measurement, one can choose a light source

with a specific spectral profile to optimally heat up the object by light illumination. The induced periodic heat pattern on the surface was then captured using a long wavelength infrared camera. Figure 5.9 shows the experimental setup used for the “Heat Induced Moiré” technique. The sample under measurement was a black egg-holder shaped object with very low reflectivity in the visible spectrum.

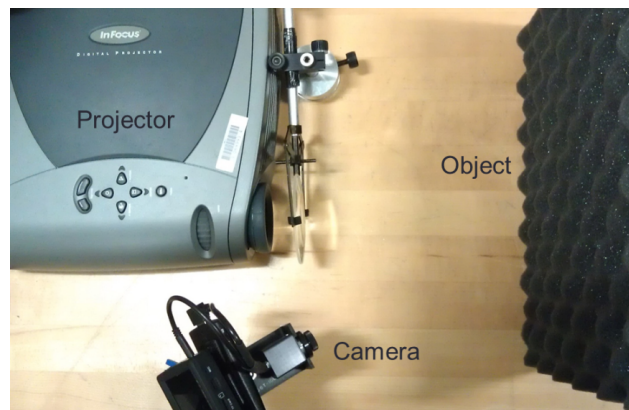


Figure 5.9: Experimental setup for profilometry of a black egg-holder shape object based on optical wavelength conversion from visible to deep infrared spectrum.

Figure 5.10 (a) shows the reflected heat pattern obtained from the test sample using a heat camera and figure 5.10 (b) shows the reflected visible pattern of the same sample obtained by a conventional visible camera. The fringe visibility of the periodic heat pattern obtained by the heat camera is more than two times better than the fringe visibility of the visible reflected pattern obtained by the visible camera.

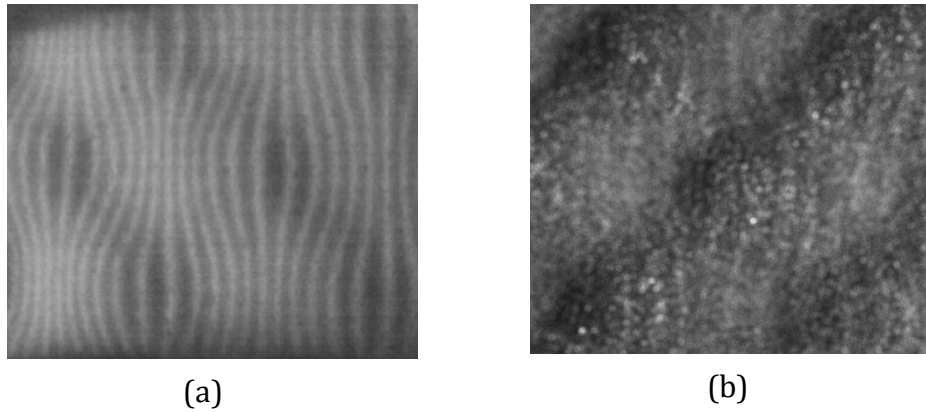


Figure 5.10: (a) Image obtained from a dark egg-holder shape object by the infrared camera, and (b) image from the dark egg-holder shape object by a conventional camera at visible spectrum.

Figure 5.11 (a) shows the one-dimensional profile of the heat pattern obtained by the IR camera along the blue line indicated. The form of the profile was removed using a polynomial fit in Matlab and the best fit sinusoidal function was found using the least square regression model to obtain the frequency of the fringe pattern, figure 5.11 (b). The same process has been applied on the 1D profile of the reflected fringe pattern obtained by the visible camera, figure 5.12 (a), and 5.12 (b). Due to high level of noise in the image obtained from the visible camera, the correct spatial frequency could not be obtained while the spatial frequency obtained from the heat pattern accurately matches the projected signal. The calculated SNR of the fringe pattern obtained by the heat camera is 10 times better than the SNR of the fringe pattern obtained by the visible camera. These results indicate that, for objects composed of dark, non-reflective material, analyzing the heat fringes gives more reliable information from the object compared to the reflected fringes in the visible spectrum.

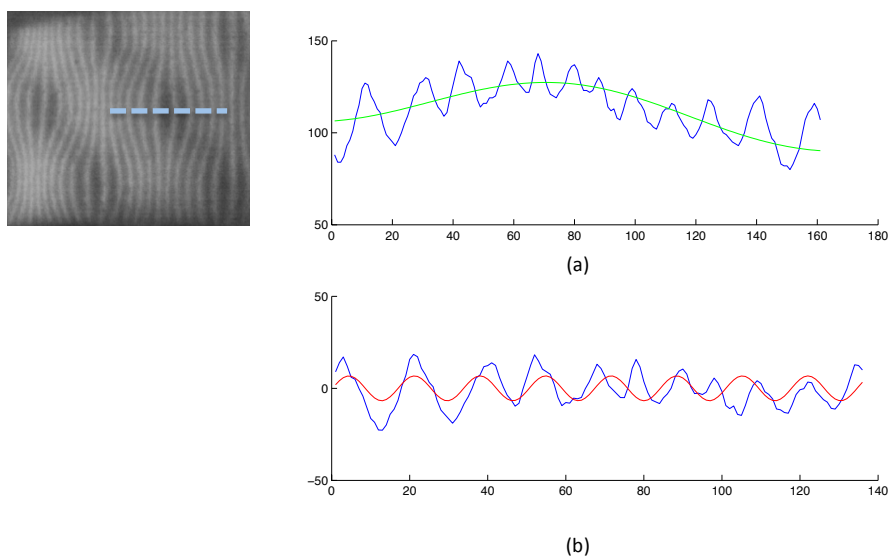


Figure 5.11: (a) One dimensional profile of the heat pattern along the blue dotted line and the best fit polynomial to the profile, the green curve, and (b) the form-free profile of the pattern along the blue dotted line. The red plot is the best sinusoidal fit to the obtained heat pattern, (SNR = 0.309).

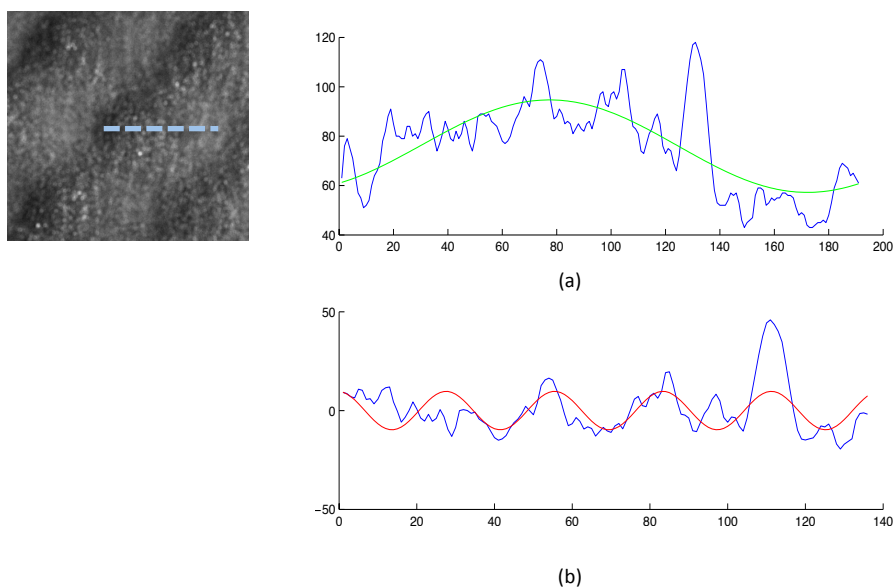


Figure 5.12: One-dimensional profile of the heat pattern along the blue dotted line and the best fit polynomial to the profile, the green curve, and (b) the form-free profile of the pattern along the blue dotted line. The red plot is the best sinusoidal fit to the obtained heat pattern, (SNR = 0.038).

Another important factor that needs to be considered before retrieving the phase from the heat pattern using the conventional fringe analysis technique, is to find the optimum time in which the heat patterns follows a sinusoidal structure.

In our experiment, in order to find the proper acquisition time, we illuminated a predefined fringe pattern with a specific frequency and intensity to a flat object with the same thermal properties of the test object. Then a series of heat patterns at different times were obtained using the IR camera. All images were analyzed in Matlab by finding the best sinusoidal fit for each heat pattern using the least-square regression model. We defined a coefficient of determination (CD), which basically calculates the difference between each heat pattern with its best sinusoidal fit, equation 5.6.

$$CD = \sum_{x,y} (I(x,y) - I^f(x,y))^2 \quad (5.6)$$

where $I(x,y)$ is the value of the obtained heat pattern, and $I^f(x,y)$ is the value of the fitted pattern at each point.

The image with a minimum value for the CD is the pattern with the closest shape to a perfect sinusoidal. The corresponding capture time of the selected image was then used as the optimum acquisition time for the rest of the experiment. Figure 5.13 shows a set of images obtained by the heat camera from a flat object at different times. A cross sectional profile of each image compared with the best sinusoidal fit and the CD was then calculated. For our test sample, the minimum CD value occurred at 15 ms.

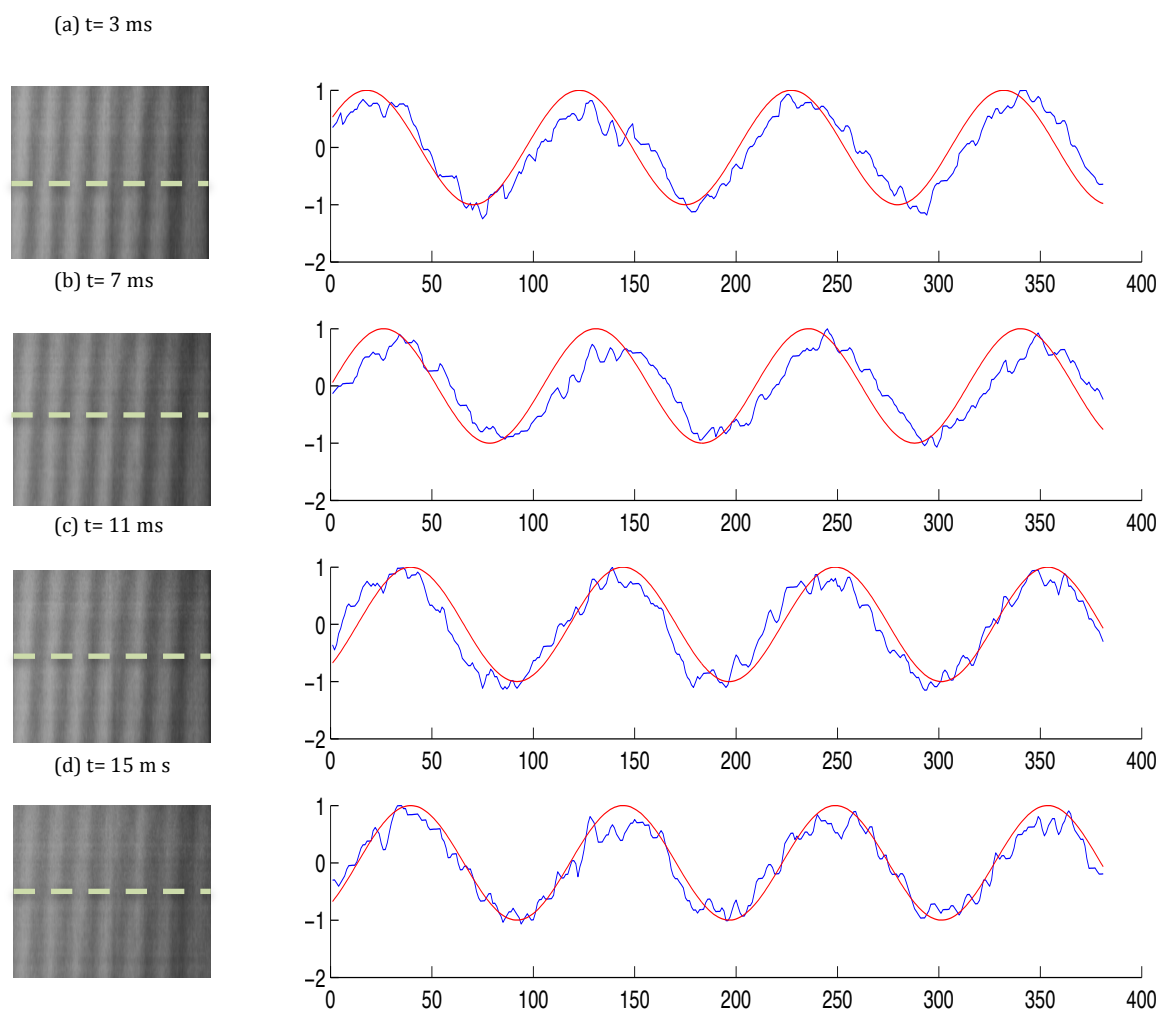


Figure 5.13: Heat patterns of a flat object obtained at different times and the profile of each pattern compared with its best sinusoidal fit.

In our work we used the Fourier transform technique to analyze the profile of the test object. Figure 5.14 shows the heat pattern obtained by the heat camera from a single bump of the test sample along with its calculated profile.

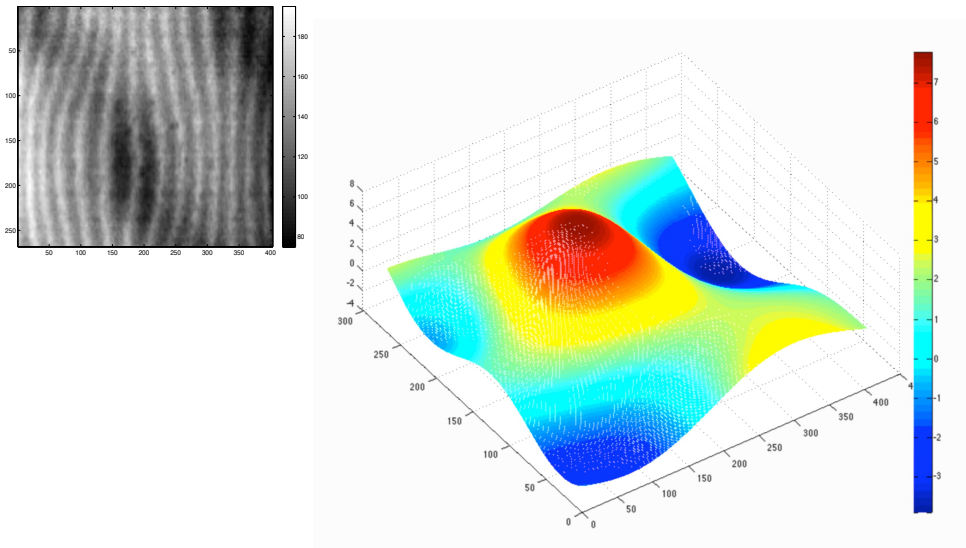


Figure 5.14. The sinusoidal heat pattern from one bump of the dark egg-holder shape object using the infrared Moiré technique, and the reconstructed height map of the object.

The reconstructed profile precisely shows the height variation of the object's surface. The peak to valley of a single bump shown in Figure 5.14 is 10.86 cm. We also used a deformed egg-holder as a second test object. Figure 5.15 shows the heat pattern obtained by the heat camera from two bumps of the second test sample. The reconstructed profile of the object shows two bumps with different peak to valley values of 10.46 cm and 8.32 cm.

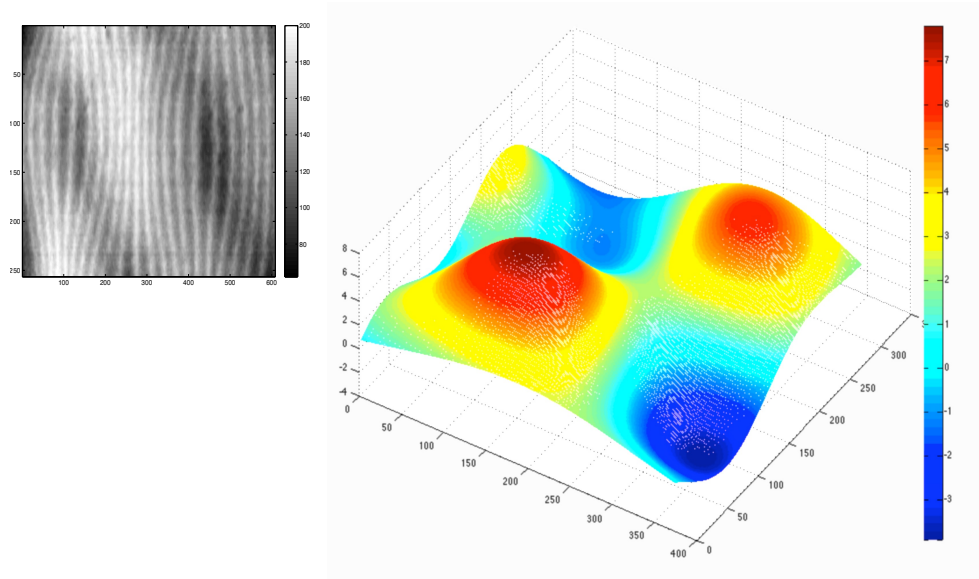


Figure 5.15: The sinusoidal heat pattern from two bumps of the dark egg-holder shape object using the infrared Moire technique, and the constructed height map of the object.

5.4. Discussion

Results obtained from both radiative (fluorescence) and non-radiative (heat) wavelength conversion phenomena combined with the fringe projection 3D profilometry technique verified that this technique can enhance the SNR of the acquired fringe pattern obtained from objects made from some unique materials, hence the precision of the measurement will be improved. Additionally, in this technique the surface becomes a large format incoherent source that emits light in all directions, which increases the effective numerical aperture of the system, and the measurement becomes less dependent on the geometry of the object.

CHAPTER 6: CONCLUSIONS AND FUTURE WORK

6.1. Conclusions

In this research effort, we have developed several solutions to stretch the capability of laser interferometers, and fringe projection systems for 3D profile measurement of objects with complex geometry and/or complex compositions.

One main limitation in metrology of complex objects using fringe projection and laser interferometer profilometry systems is the limited dynamic range of their imaging units. Usually, complex objects show a larger level of reflectivity upon illumination compared to what can be captured by a conventional camera. As the result, some information in the reflected light from the object cannot be correctly recorded by the camera, which limits the capability of the system to calculate the correct height map of the object under measurement.

We have developed the Spatially Varying Pixel Intensity (SVPI) technique as a tool to enhance dynamic range in both digital fringe projection 3D profilometry system and laser interferometers.

The main goal of SVPI technique is to control the irradiance received on the imaging system at pixel level, hence most information recorded by the camera contains reliable information from the object under measurement.

In chapter 3, the implementation of SVPI technique on a digital fringe projection 3D profilometry system was described. The high dynamic range fringe images were acquired by recursively controlling the intensity of the projection pattern at pixel level based on

the feedback from the reflected images obtained by the camera. The SVPI technique algorithm introduced in chapter 3 was developed for a digital fringe projection system. We first verified the technique by a simulation in Matlab. The result of simulation indicated that the SVPI is not only capable of controlling the intensity of light received by the camera but also it can reconstruct the true intensity value of each pixel by applying the inverse analysis, and finally calculate the correct phase map of the object under measurement.

Three different fringe projection profilometry setups were developed, and SVPI algorithm was incorporated to experimentally verify the concept on 3D profilometry surface measurement of complex objects with different sizes ranges from several micrometers to tens of centimeters.

The first setup was developed for 3D profilometry of a calibration ball with a couple of millimeters diameter. The calibration ball has a wide range of reflectivity towards the camera due to its spherical shape with large slopes on the sides; therefore a conventional fringe projection system, which utilizes a conventional 8-bit camera is not capable of reconstructing the entire shape of the object. We applied the SVPI technique to this system and the results showed that the SVPI was able to stretch the capability of the fringe projection system by enhancing the dynamic range by 20%, and hence a full-field 3D profile of the object was reconstructed.

A stereomicroscope-based fringe projection system was constructed, and SVPI algorithm was incorporated for a reliable 3D profile measurement of solder bumps. Solder bumps are semi-hemispherical shaped bumps with diameters on the order of 80-100 μm and approximately 25-50 μm of height, which are grouped in thousands on a

package substrate to provide the electrical input/output connections in semiconductor flip chip technology. Due to the spherical shape of the bumps and their composition, the intensity level of light reflecting off these structures are much higher than the dynamic range of any conventional camera used in a fringe projection 3D profilometry system. Hence, none of the fringe projection profilometry systems are capable of measuring the entire shape of these structures. However, using the SVPI algorithm enhanced the dynamic range of the stereomicroscope based fringe projection system and consequently allowed acquisition of a full-field 3D map of the solder bumps. Also, the fitting algorithm is applied to the acquired 3D profile of the bumps to estimate the sharp boundaries between the bumps and the substrate.

The third fringe projection setup was constructed to apply the SVPI technique for inspection of a large format hemispherical shaped industrial object. The results showed that the SVPI technique could enhance dynamic range of such systems by 40% and hence reconstruct the entire 3D profile of the object.

In chapter 4, the concept of SVPI technique was used to enhance dynamic range in laser interferometers. A modified SVPI algorithm was developed and verified experimentally. The modified SVPI algorithm was incorporated in a Michelson laser interferometer to measure the profile of a super polished flat mirror with nominal flatness of less than $\lambda/10$.

The interferogram of such an object using a typical Michelson laser interferometer has a bright central part and very dark borders due to Gaussian distribution of the interfering beams. Therefore, full-field phase information from such an interferogram cannot be obtained using conventional laser interferometers due to the limited dynamic

range of their imaging system. In order to implement the concept of SVPI technique in a Michelson laser interferometer, we placed a spatial light modulator (SLM) in front of the camera to spatially control the irradiance of the interferogram on the camera at pixel level. The SVPI technique improved the dynamic range of the system by 128 %.

As a result, we were able to inspect a larger area of the object under measurement since we were able to simultaneously preserve the correct intensity information from the bright central part of the interferogram as well as its dark borders. Furthermore, the results obtained from an optically flat surface indicated that the SVPI can also enhance the signal to noise ratio at each iteration, and the results are more robust to the noise in the system.

In chapter 5, we introduced a novel technique based on the concept of optical wavelength conversion to stretch the capability of fringe projection 3D profilometry systems in inspecting objects composed of unique raw materials.

First, an experimental setup was used to demonstrate the concept of 3D profilometry based on optical wavelength conversion on a hemispherical object, composed of a specific polymer, which fluoresces under the illumination of the blue light. The results indicated that the proposed technique improved the SNR of the system six fold. As a result, a more accurate 3D profile of the object was reconstructed using the proposed technique compared to the one constructed by a conventional fringe projection profilometry system.

In the second part of chapter 5, an experimental setup was developed for 3D profile measurement of an optically dark, non-reflective object based on wavelength conversion technique. Dark objects do not reflect light in the visible spectrum due to their high

absorption coefficients at these wavelengths; instead they absorb the energy of light and convert its energy to deep infrared (heat) wavelength. In our experiment we used a heat camera, to detect the optically induced heat pattern onto the object surface, and based on the deformed heat pattern and by using the conventional fringe analysis technique we were able to construct the 3D profile of an egg-shaped holder object composed of dark material.

In conclusion, the results obtained in this research effort indicate that both SVPI technique and profilometry based on optical wavelength conversion technique enhance the capability of optical-based surface metrology tools for a more reliable and robust surface inspection of objects. We mainly focused on digital fringe projection technique and laser interferometers, but the proposed techniques can incorporate other optical metrology tools with proper implementation.

6.2. Future Work

The measurement results in chapter 3 and 4 showed that SVPI technique is very powerful to enhance dynamic range in both fringe projection and laser interferometer systems, which ultimately improves the accuracy of the final height map of the objects under measurement using the mentioned instruments. The SVPI technique can adapt itself based on the feedback received from the object in real time. Therefore it can be a good candidate for in-line, real time measurements. Our current setups developed for both fringe projection and laser interferometers require at least a couple of minutes to reconstruct the height-map of the object. Future research for SVPI technique needs to be focused on decreasing the overall measurement time for a fast, real-time inspection of the part by automating the system and investigating faster fringe analysis techniques for

specific applications. Also, the overall performance of the technique can be improved using a higher resolution projector and camera.

Another approach for future work in the SVPI technique is to incorporate the technique with the dual Moiré laser interferometer system [18] to enhance dynamic range in both Moiré technique and laser interferometer. The combined technique enables us to obtain a reliable full-field measurement of complex objects with high-resolution features on top of them.

Profilometry based on optical wavelength conversion was another topic in our research. The results obtained in this research showed that this technique is capable of surface profilometry of dark, non-reflective objects. One approach for future research in this area is to investigate the effect of this technique in measuring uniformity in the bulk objects (including dark objects) by periodically illuminating the sample with a plane uniform light wave. It has been shown [109] that when a solid is periodically illuminated with a sinusoidal modulated intensity, equation 6.1, the distribution of the heat through its bulk also follows a sinusoidal equation, in which its intensity attenuates as it propagates through the bulk of the object, equation 6.2.

$$I(t) = I_0 (1 + \cos \omega t)/2 \quad (6.1)$$

where, $\omega = 2\pi f$, is the angular modulation frequency, and t is the time.

$$\vartheta(x) = \frac{I_0}{2\varepsilon\sqrt{\omega}} \exp\left(-\frac{x}{\mu}\right) \cos\left(\frac{x}{\mu} + \frac{\pi}{4}\right) \quad (6.2)$$

where, ε is the thermal effusivity of the object which indicates the amplitude of the

temperature at the sample surface, and $\mu = \sqrt{\frac{2\alpha}{\omega}}$, where α is the thermal diffusivity of the object, which determines the rate at which a temperature variation propagates through the material.

Therefore, if we periodically illuminate the sample from one side of the object, and monitor the heat distribution from the other side of object, we will observe a sinusoidal heat pattern, in which any non-uniformity of the object will cause a phase modulation. Figure 6.1 shows a simple schematic of the possible experimental setup for this technique.

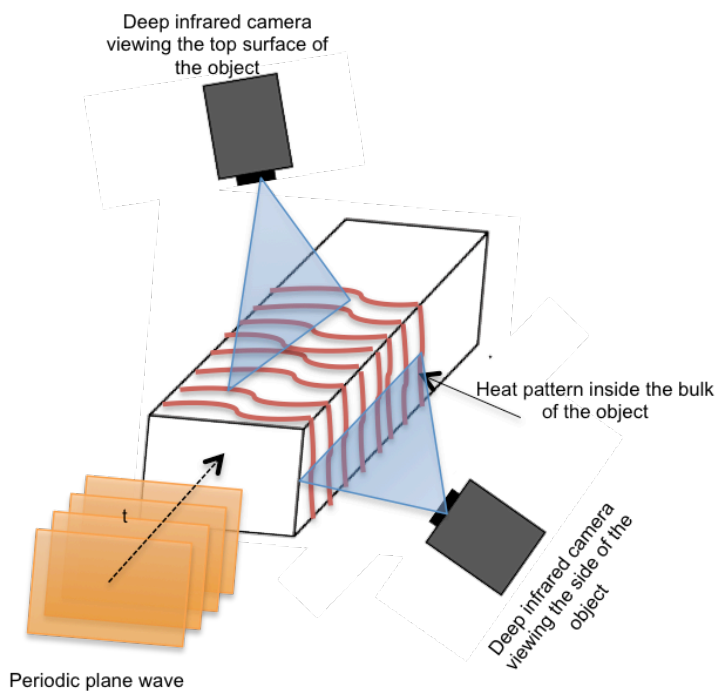


Figure 6.1: Simple schematic for 3D thermal imaging of an object to detect non-uniformity.

REFERENCES

- [1] G.E. Sommargren, “ A new laser measurement system for precision metrology,” *Precis. Eng.* vol. 9(4), p. 179-184, (1987).
- [2] D. Malacara, “Optical Shop Testing”, John Wiley & Sons Inc Publications, Hoboken, New Jersey, Chap. 16, (2007).
- [3] M. Minsky, “Microscopy apparatus” , U.S. Patent 3,013,467, (1961).
- [4] T.Wilson, “ Confocal Microscopy”, Academic Press, London, (1990).
- [5] H. J. Tiziani and H.-M. Uhde, “Three-dimensional image sensing by chromatic confocal microscopy” , *Applied Optics*, vol. 33, no. 10, (1994).
- [6] C. A. Sciammarella, “The Moiré Method—A Review,” *Optics Express. Mech.* vol. 19, p. 418–422, (1979).
- [7] K. Creath, J. Schmit, and C. Wyant, “Optical Metrology of Diffuse Surfaces in Optical Shop Testing”, D. Malacara (John Wiley & Sons, Inc. Publications, Hoboken, , pp. 756-807, New Jersey, (2007).
- [8] K. J. Gåsvik, “Optical Metrology” ,John Wiley & Sons, Ltd, (2002).
- [9] J. A. N. Buytaert, J. J. J. Dirckx, “Moiré profilometry using liquid crystals for projection and demodulation”, *Opt. Express* vol.16, p.179-193, (2008).
- [10] G. N. de Oliveira, M. E. de Oliveira, and P. A. M. dos Santos, “Dynamic moiré patterns for profilometry applications,” *J. Phys.: Conf. Ser.* 274 012036, (2011).
- [11] TSAI M; HUNG C, “Development of a high-precision surface metrology system using structured light projection”, *Measurement*, vol.38, no. 3 , p. 236-247, (2005).
- [12] Gorthi, S. S. and Rastogi, P, “Fringe Projection Techniques: Whither we are?”, *Optics and Lasers in Engiering*, vol. 48(2), p. 133-140, (2010).
- [13] F. Chen,. et al, “Overview of three-dimensional shape measurement using optical methods” , *Optical Engineering*, vol. 39/1, P.10-22, (2000).
- [14] C. Reich, et al., “3-D shape measurements of complex objects by combining photogrammetry and fringe projection”, *Optical Engineering*, vol. 39, no. 1, p. 224-231, (2000).
- [15] P. de Groot, "Coherence scanning interferometry", *Optical Measurement of Surface Topography*, R. Leach, ed., 1st Edition, p.187-208, Springer Verlag, Berlin, (2011).

- [16] J. C. Wyant and J. Schmit, "Large field of view, High spatial resolution, Surface measurement", *Tools Manufact.* vol. 38. no. 5-6, p. 691-698, (1998).
- [17] A. Olszak, M. Descour, "Microscopy in Multiples, Array-based microscopy enhances speed while maintaining large fields of view", the SPIE magazine of photonics Technologies and Applications, May (2005).
- [18] M. Abolbashari, A. S. Gerges, A. Davies, "Dual Moiré and Laser Interferometry as a Metrology Tool", *Proc. ASPE*, San Diego, p. 256-259, (2012).
- [19] D. Ghiglia and M. Pritt, "Two-Dimensional Phase Unwrapping: Theory, Algorithms, and Software" John Wiley & Sons, New York, (1998).
- [20] M. D. Pritt and J. S. Shipman, "Least-squares two-dimensional phase unwrapping using FFT's," *IEEE Transactions on Geoscience and Remote Sensing*, vol. 32, no. 3, p. 706–708, May (1994).
- [21] M.D. Pritt, "Phase unwrapping by means of multigrid techniques for interferometric SAR," *IEEE h n s . Geosci. Rem. Sen.*, vol. 34, no. 3. p 728-738, (1996).
- [22] D. C. Ghiglia and L. A. Romero, "Minimum L^p -norm two-dimensional phase unwrapping," *Journal of the Optical Society of America A*, vol. 13, no. 10, p. 1999, Oct. (1996).
- [23] A. Baldi, "Two-dimensional phase unwrapping by quad-tree decomposition," *Appl. Opt.* vol. 40, p. 1187–1194, (2001).
- [24] M. Arevallilo Herra'ez, D. R. Burton, and D. B. Clegg, "Robust, simple, and fast algorithm for phase unwrapping," *Appl. Opt.* vol. 35, p. 5847–5852, (1996).
- [25] P. Stephenson, D. R. Burton, and M. J. Lalor, "Data validation techniques in a tiled phase unwrapping algorithm," *Opt. Eng.* vol. 33, p. 3703–3708, (1994).
- [26] K. M. Hung and T. Yamada, "Phase unwrapping by regions using least-squares approach," *Opt. Eng.* vol. 37, p. 2965–2970, (1998).
- [27] J. J. Gierloff, "Phase unwrapping by regions," in *Current Developments in Optical Engineering II*, R. E. Fischer and W. J. Smith, eds., *Proc. SPIE*, (1987).
- [28] P. G. Charette, and I. W. Hunter, "Robust phase-unwrapping method for phase images with high noise content," *Appl. Opt.* vol. 35, p. 3506–3513, (1996).
- [29] R. M. Goldstein, H. A. Zebker, and C. L. Werner, "Satellite radar interferometry: Two-dimensional phase unwrapping," *Radio Science*, vol. 23, no. 4, p. 713, (1988).

- [30] O. Y. Kwon, D. M. Shough, R. A. Williams, "Stroboscopic phase-shifting interferometry," *Opt. Lett.*, vol. 12, p. 855–857, (1987).
- [31] J. Schoëner, A. Etemeyer, U. Neupert, H. Rottenkolber, C. Winter, and P. Obermeier, "New approaches in interpreting holographic images," *Opt. Lasers Eng.*, vol. 14, p. 283–291, (1991).
- [32] H. A. Vrooman and A. M. Maas, "Image processing algorithms for the analysis of phase-shifted speckle interference patterns," *Appl. Opt.* vol. 30, p. 1636–1641, (1991).
- [33] J. A. Quiroga and E. Bernabeu, "Phase unwrapping algorithm for noisy phase-map processing," *Appl. Opt.* vol. 33, p. 6725–6731, (1994).
- [34] J. A. Quiroga, A. Gonzalez-Cano, and E. Bernabeu, "Phase unwrapping algorithm based on adaptive criterion," *Appl. Opt.* vol. 34, p. 2560–2563, (1995).
- [35] W. Xu, and I. Cumming, "A region-growing algorithm for In- SAR phase unwrapping," *IEEE Trans. Geosci. Remote Sens. IGARSS'96* vol. 34, p. 2044–2046, (1996).
- [36] P. E. Debevec and J. Malik., "Recovering high dynamic range radiance maps from photographs", In *Proceedings of SIGGRAPH, ACM SIGGRAPH / Addison Wesley, Los Angeles, California, Computer Graphics Proceedings, Annual Conference Series*, 369–378, (1997).
- [37] S. Mann and R. Mann. "Quantigraphic imaging: Estimating the camera response and exposures from differently exposed images", *Proceedings of the Computer Society Conference, IEEE*, vol. 1, (2001).
- [38] M. A. Robertson, S. Borman, and R. L. Stevenson, "Estimation-theoretic approach to dynamic range enhancement using multiple exposures", *Journal of Electronic Imaging*, (2003).
- [39] C. Wyckoff, "Silver Halide Photographic Film having Increased Exposure-response Characteristics", *US Patentt 3450536*, (1969).
- [40] G. Ward., "Fast, robust image registration for compositing high dynamic range photographs from hand-held exposures.", *Journal of Graphics Tools: JGT*, vol. 8(2), p.17–30, (2003).
- [41] S. Mann, C. Manders, and J. Fung., "Painting with looks: Photographic images from video using quantimetric processing", In *ACM international conference on Multimedia*, p.117–126, (2002).

- [42] S. Mann and R. Picard. "Being undigital with digital cameras: Extending dynamic range by combining differently exposed pictures.", In IS&T 46th annual conference, p. 422–428, (1995).
- [43] T. Mitsunaga and S. K. Nayar. "Radiometric self calibration. In Computer Vision and Pattern Recognition", vol. 2, p. 374–380, 1997.
- [44] Zhang S, Yau ST., "High dynamic range scanning technique", Opt Eng; vol. 48, p. 033604–47, (2009).
- [45] J. Vargas, T. Koninckx, J.A. Quiroga, L.V. Gool, "Three dimensional measurement of microchips using structured light techniques", Optical Engineering vol. 47, (2008).
- [46] P.E. Debevec, J. Malik, "Recovering high dynamic range radiance maps from photographs", SIGGRAPH, vol. 97, p. 369-378, (1997).
- [47] J. Vargas, L. González-Fernandez, J. Antonio Quiroga, T. Belenguer, "Shack–Hartmann centroid detection method based on high dynamic range imaging and normalization techniques", Appl. Opt. vol. 49 P. 2409- 2416, (2010).
- [48] R. M. Groves, P. Giancarlo, O.Wolfgang, "Real-time extended dynamic range imaging in shearography", Appl. Opt., vol. 47, (2008).
- [49] J. Vargas, R. Restrepo, J.A. Quiroga, T. Belenguer, "High dynamic range imaging method for interferometry", Optics Communications, vol. 284, (2011).
- [50] Chou, Sen-Yih, et al. Projection moiré profilometry with high-dynamic range image. Opt Eng, vol. 51(2), p. 021112–21121, (2012).
- [51] C. Quan, C.J.Tay, X.Y.He, X.Kang, H.M.Shang, "Microscopicsurface contouring by fringe projection method", Opt. Laser Techn., vol. 34 (7) p. 547–552, (2002).
- [52] X.He, W.Sun, X.Zheng, M.Nie, "Static and dynamic deformation measurements of micro beams by the technique of digital image correlation", Key Engineering Materials vol. 326-328 , p. 211–214, (2006).
- [53] S.T.Yilmaz, U.D.Ozugurel, K.Bulut, M.N.Inci, "Vibrationamplitude analysis with a single frame using a structured light pattern of a four-core optical fibre", Opt. Commun., vol. 249 (4-6) p. 515–522, (2005).
- [54] Q. Zhang, X. Su, " High-speed optical measurement for the drumhead vibration", Opt. Express, vol.13 (8) , p. 3110–3116, (2005).
- [55] J. Burke, T. Bothe, W. Osten, C. Hess, Reverse engineering by fringe projection, Proc. SPIE, vol. 4778 , p. 312–324, (2002).

- [56] C.Lin, H.He, H.Guo, M.Chen, X.Shi,T.Yu, “Fringe projection measurement system in reverse engineering”, *Journal of Shanghai University*, vol. 9 (2) , p.153–158, (2005).
- [57] J. Hecht, K. Lamprecht, M. Merklein, K. Galanulis, J. Steinbeck, “Triangulation based digitizing of tooling and sheet metal part surfaces: Measuring technique, analysis of deviation to CAD and remarks on use of 3D-coordinate fields for the finite element analysis”, *Key Engineering Materials*, vol. 344 , p. 847–853, (2007).
- [58] H. Yen, D. Tsai, J. Yang, “Full-field 3-D measurement of solder pastes using LCD-based phase shifting techniques”, *IEEE Trans. Electronics Packaging Manufacturing*, vol. 29 (1) , p. 50–57, (2006).
- [59] T. Hui, G. K. Pang, “Solder paste inspection using region-based defect detection”, *Int. Journal of Advanced Manufacturing Technology*, vol. 42 (7-8) , p. 725–734, (2009).
- [60] D. Hong, H. Lee, M. Y. Kim, H. Cho, J. Moon, “Sensor fusion of phase measuring profilometry and stereo vision for three-dimensional inspection of electronic components assembled on printed circuit boards”, *Appl. Opt.* vol. 48 (21) , p. 4158–4169, (2009).
- [61] J.Yagnik, S.S.Gorthi, K.R.Ramakrishnan, L.K.Rao, “3D shape extraction of human face in presence of facial hair: A profilometric approach”, *Proc. IEEE Region 10 Annual International Conference (4085277)*, (2007).
- [62] G.Zhou, Z.Li, C.Wang, Y.Shi, “A Novel Method for Human Expression Rapid Reconstruction”, *Tsinghua Science and Technology*. vol. 14 ,p. 62– 65, (2009).
- [63] L. Chen, C. Huang, “Miniaturized 3D surface profilometer using digital fringe projection”, *Meas. Sci. Techn.*, vol.16 (5) , p.1061–1068, (2005).
- [64] K.Genovese, C.Pappalettere, “Whole 3D shape reconstruction of vascular segments under pressure via fringe projection techniques”, *Opt. Laser Eng.*, vol. 44 (12), p. 1311–1323, (2006).
- [65] F. Lilley, M. J. Lalor, D. R. Burton, “Robust fringe analysis system for human body shape measurement”, *Opt. Eng.*, vol.39 (1) , p.187–195, (2000).
- [66] C.J.Moore, D.R.Burton, O.Skydan, P.J.Sharrock, M.Lalor, “3D body surface measurement and display in radiotherapy part I: Technology of structured light surface sensing”, *Proc. Int. Confe. Medical Information Visualisation - BioMedical Visualisation*, (2006).
- [67] T.Hain, R.Eckhardt, K.Kunzi-Rapp, B.Schmitz, “Indications for optical shape measurements in orthopaedics and dermatology”, *Medical Laser Application*, vol. 17 (1) , p. 55–58, (2002).

- [68] Y.Ferrag, D.Black, J.M.Lagarde, A.M.Schmitt, S.Dahan, J.L.Grolleau, S. Mordon, “ Use of a 3D imaging technique for non-invasive monitoring of the depth of experimentally induced wounds”, *Skin Research and Technology*, vol.13(4) , p. 399–405, (2007).
- [69] S. Jaspers, H. Hopermann, G. Sauermann, U. Hoppe, R. Lunderstaedt, J. Ennen, “Rapid in vivo measurement of the topography of human skin by active image triangulation using a digital micromirror device”, *Skin Research and Technology*, vol.5 (3) , p.195–207, (1999).
- [70] J. M. Lagarde, C. Rouvrais, D. Black, S. Diridollou, Y. Gall, “Skin topography measurement by interference fringe projection: A technical validation” , *Skin Research and Technology*, vol. 7 (2) , p. 112–121, (2001).
- [71] G. Oh, J. H. Yoon, H. S. Kye, D. H. Kim, J. Y. Kim, J. Choi, S. Seo, Y. C. Kye, H. H. Ahn, I. J. Rhyu, “3D reconstruction of skin pathological tissue: the understanding of microrelief pattern and dermal ridge”, *Skin Research and Technology*, vol. 20, (2014).
- [72] E. B. Li, X. Peng, J. Xi, J. F. Chicharo, J. Q. Yao, D. W. Zhang, “Multi- frequency and multiple phase-shift sinusoidal fringe projection for 3D profilometry”, *Opt. Express*, vol. 13 (5) , p. 1561–1569, (2005).
- [73] J. I. Harizanova, E. V. Stoykova, V. C. Sainov, “ Phase retrieval techniques in coordinates measurement”, *AIP Conference Proceedings*, vol. 899, p. 321–322, (2007).
- [74] W. Su, K. Reichard, S. Yin, F. T. S. Yu, “Fabrication of digital sinusoidal gratings and precisely controlled diffusive flats and their application to highly accurate projected fringe profilometry”, *Opt. Eng.*, vol. 42 (6) , p.1730–1740, (2003).
- [75] J. Zhang, C. Zhou, X. Wang, “Three-dimensional profilometry using a Dammann grating”, *Appl. Opt.*, vol. 48 (19) , p. 3709–3715, (2009).
- [76] C. R. Coggrave, J. M. Huntley, “High-speed surface profilometer based on a spatial light modulator and pipeline image processor”, *Opt. Eng.*, vol. 38 (9), p. 1573–1581, (1999).
- [77] G. S. Spagnolo, D. Ambrosini, “Diffractive optical element-based profilometer for surface inspection”, *Opt. Eng.*, vol. 40 (1) , p. 44–52, (2001).
- [78] T. L. Pennington, H. Xiao, R. May, A. Wang, “Miniaturized 3-D surface profilometer using a fiber optic coupler”, *Opt. Laser Technol.*, vol. 33 (5) , p. 313–320, (2001).
- [79] T. Anna, S. K. Dubey, C. Shakher, A. Roy, D. S. Mehta, “Sinusoidal fringe projection system based on compact and non-mechanical scanning low-coherence

- Michelson interferometer for three-dimensional shape measurement”, *Opt. Commun.*, vol. 282 (7), p. 1237–1242, (2009).
- [80] M. K. Kalms, W. P. Jueptner, W. Osten, “Automatic adaption of projected fringe patterns using a programmable LCD-projector”, *Proc. SPIE*, vol. 3100, p. 156–165, (1997).
- [81] J. Salvi, J. Pages, J. Batlle, “Pattern codification strategies in structured light systems”, *Pattern Recognition*, vol. 37 (4), p. 827–849, (2004).
- [82] K. Iwata, F. Kusunoki, K. Moriwaki, H. Fukuda, T. Tomii, “Three-dimensional profiling using the fourier transform method with a hexagonal grating projection”, *Appl. Opt.*, vol. 47 (12), p. 2103–2108, (2008).
- [83] L.Chen, C.Quan, C.J.Tay, Y.Fu, “Shapemeasurementusingoneframe projected sawtooth fringe pattern”, *Opt. Commun.*, vol. 246 (4-6), p. 275–284, (2005).
- [84] P.Jia, J.Kofman, C.English, “Error compensation in two-step triangular pattern phase-shifting profilometry”, *Opt. Laser Eng.*, vol. 46 (4), p. 311–316, (2008).
- [85] V. Srinivasan, H. C. Liu, M. Halioua, “Automated phase-measuring profilometry of 3-D diffuse objects”, *Appl. Opt.*, vol. 23 (18), p. 3105–3108, (1984).
- [86] M. Chang, D. Wan, “On-line automated phase-measuring profilometry”, *Opt. Laser Eng.*, vol. 15 (2), p. 127–139, (1991).
- [87] X.F.Meng, X.Peng, L.Z.Cai, A.M.Li, J.P.Guo, Y.R.Wang, “Wavefront reconstruction and three-dimensional shape measurement by two-step dc term suppressed phase-shifted intensities”, *Opt. Lett.*, vol. 34 (8), p. 1210–1212, (2009).
- [88] M. Takeda, K. Mutoh, “Fourier transform profilometry for the automatic measurement of 3-D object shapes”, *Appl. Opt.*, vol. 22 (24), p. 3977–3982, (1983).
- [89] J.-F. Lin, X.-Y. Su, “Two-dimensional Fourier transform profilometry for the automatic measurement of three-dimensional object shapes”, *Opt. Eng.*, vol. 34 (11), p. 3297–3302, (1995).
- [90] X. Su, W. Chen, “Fourier transform profilometry: A review”, *Opt. Laser Eng.*, vol. 35 (5), p. 263–284, (2001).
- [91] F. Berryman, P. Pynsent, J. Cubillo, “The effect of windowing in Fourier transform profilometry applied to noisy images”, *Opt. Laser Eng.*, vol. 41 (6) p. 815–825, (2004).

- [92] R. Zhang, H. Guo, “Phase gradients from intensity gradients: a method of spatial carrier fringe pattern analysis”, *Optics Express*, vol. 22(19), p. 22432-22445 (2014).
- [93] P. H. Chan, P. J. Bryanston-Cross, and S. C. Parker, “Spatial phase stepping method of fringe-pattern analysis,” *Opt. Lasers Eng.*, vol. 23(5), p.343–354, (1995).
- [94] Q. Kema, “Two-dimensional windowed Fourier transform for fringe pattern analysis: Principles, applications and implementations,” *Optics and Lasers in Engineering*, vol. 45 (2), p. 304–317, (2007).
- [95] Creath K. “Phase-measurement interferometry techniques.” *Progr Opt*, vol. 26(26), p. 349–393, (1988).
- [96] R.M. Groves, G. Pedrini, W. Osten, “Real-time extended dynamic range imaging in shearography”, *Applied Optics*, vol. 47, p. 5550- 5556, (2008).
- [97] C. Quan, C.J. Tay, T. Wu, S.H. Wang, H.M. Shang, “Optimal use of dynamic range of a white light video measurement system”, *Optics Communications*, vol. 237, p. 243-250, (2004).
- [98] S. Ri, M. Fujigaki, Y. Morimoto, “Intensity Range Extension Method for Three-dimensional Shape Measurement in Phase-measuring Profilometry Using a Digital Micromirror Device Camera”, *Applied Optics*, vol. 47, p. 5400- 5407, (2008).
- [99] G. Pedrini, H.J. Tiziani, I. Alexeenko, “Digital-holographic interferometry with an image-intensifier system”, *Applied Optics*, vol. 41, p. 648-653, (2002).
- [100] J. Vargas, T. Koninckx, J.A. Quiroga, L.V. Gool, “Three dimensional measurement of microchips using structured light techniques”, *Optical Engineering*, vol. 47, (2008).
- [101] Agulló-López, Fernando, and José Manuel Cabrera., “Electrooptics: phenomena, materials and applications”, *Academic Press*, vol. 1, (1994).
- [102] S. H. Lee, S. S Bhattacharyya, H. S. Jin, K. Jeong, “Devices and materials for high-performance mobile liquid crystal displays”, *J. Mater. Chem.*, vol ,22, p.11893-11903, (2012).
- [103] R. K. Goel, A. Panwar, “Carbon Nano Tubes:A New Approach In Material Science”, *International Journal of Latest Research in Science and Technology*, vol. 1 (2), p. 2278-5299, (2012).
- [104] K. Kaneto, et al. , “Electrical conductivities of multi-wall carbon nano tubes “*Synthetic Metals*, vol. 103.1, p. 2543-2546, (1999).

- [105] X. Wan, D. Jinming, D. Y. Xing., “Optical properties of carbon nanotubes”, *Physical Review B*, vol. 58.11 ,(1998).
- [106] C. Kittel, P. McEuen., “Introduction to solid state physics”, vol. 8. New York: Wiley, 1976.
- [107] *Optical Properties of Solids*. North-Holland Publishing Company, 1980.
- [108] J.B. Fourier, “The Analytical theory of Heat”, *Encyclopedia Britannica, Inc.*, Chicago,1952.